THE UNIVERSITY OF CHICAGO

RESPONSE OF SUPERHEATED C3F8 AND C2H2F4 TO NUCLEAR AND ELECTRON RECOILS: APPLICATIONS TO DARK MATTER DETECTION

A DISSERTATION SUBMITTED TO
THE FACULTY OF THE DIVISION OF THE PHYSICAL SCIENCES
IN CANDIDACY FOR THE DEGREE OF
DOCTOR OF PHILOSOPHY

DEPARTMENT OF PHYSICS

BY
JOEL EDUARDO FUENTES

CHICAGO, ILLINOIS
DECEMBER 2021

To my parents

I am an American, Chicago born—Chicago, that somber city—and go at things as I have taught myself, free style, and will make the record in my own way: first to knock, first admitted; sometimes an innocent knock, sometimes a not so innocent. But a man's character is his fate, says Heraclitus, and in the end there isn't any way to disguise the nature of the knocks by acoustical work on the door or gloving the knuckles.

—Bellow, *The Adventures of Augie March*

TABLE OF CONTENTS

LIST OF FIGURES vii

ACKNOWLEDGMENTS x

ABSTRACT xii

1 INTRODUCTION 1
  1.1 WIMP Dark Matter 4
  1.2 WIMP Detection 8
    1.2.1 Direct Detection Methods 8
    1.2.2 Indirect Detection Methods 10
    1.2.3 Collider Searches 11
  1.3 PICO Bubble Chambers 14
    1.3.1 Seitz Theory 17
    1.3.2 Advantages of Superheated Liquids 21
    1.3.3 Present Status and Future 29

2 GUNTER CHAMBER 34
  2.1 Motivation 36
    2.1.1 New Model for Electron Recoil Response 36
    2.1.2 Acoustic Studies 41
    2.1.3 PICO-LowMass 44
  2.2 Critical Subsystems 49
    2.2.1 PID Temperature Control 49
    2.2.2 Acoustic Detection System 56
    2.2.3 Entropy Trigger 58
    2.2.4 Neural Networks for Position Reconstruction 62
    2.2.5 Bubble Finding Algorithm 65

3 C_3F_8 STUDIES 68
  3.1 Electron Recoil Mechanism and Response Parameters 68
  3.2 Acoustic Sensor Design 77
  3.3 Electron and Nuclear Recoil Classification 77

4 R-134A STUDIES 87
  4.1 Acoustic Response 90
  4.2 Electron and Nuclear Recoil Classification 90
  4.3 Response Parameters 96
    4.3.1 Electron Recoil Mechanism 96
    4.3.2 Neutron Calibration and Threshold Model 98

APPENDICES 108

A ELECTRON RECOIL ANALYSIS 109
  A.1 Fit Methodology 109

B GUNTER R-134A MCNP INPUT FILES 111
  B.1 ^{88}Y/Be 111
    B.1.1 Neutrons 111
    B.1.2 Gammas 115
  B.2 ^{22}Na 119
    B.2.1 Gammas 119

C ANALYSIS CODE 122
  C.1 Simulated Rates using Linear Threshold Model 122
    C.1.1 Program 122
  C.2 Technical Note 122
    C.2.1 setup.py 122
    C.2.2 Best Fit and Visualization 123

REFERENCES 124

LIST OF FIGURES

1.1 ΛCDM model 2
1.2 Dark-halo fit to rotation curve model 3
1.3 Dark matter as an extended halo and diagram of electron and nuclear recoils . . 4
1.4 CMB power spectra and fit to the ΛCDM model 5
1.5 Thermal relic WIMP density 6
1.6 Primordial abundances of light nuclei 7
1.7 Generic results from direct dark matter searches 9
1.8 Diffuse extragalactic photon background 11
1.9 Dark matter detection types via SM interactions 12
1.10 Comparison between direct detection experiments and the upper limit set on the WIMP nucleon cross-section via collider searches 12
1.11 Theoretical research targets for dark matter 13
1.12 Phase diagram and Gibbs potential of a superheated liquid 14
1.13 Phase diagram illustrating the thermodynamics of a superheated liquid 16
1.14 Stopping power and energy thresholds for bubble nucleations in CF_3I 18
1.15 Gamma rejection for multiple PICO chambers 22
1.16 Spatial distribution in PICO-60 WIMP search data 22
1.17 PICO discrimination of gamma-induced electron recoils and alphas 24
1.18 PICO-60 upgrade at SNOLAB 25
1.19 Comparison of cross-sections for a set of dark matter models 26
1.20 Excluded WIMP scattering cross-sections and history of coupling sensitivity . . 27
1.21 PICO-60 progress achieved during experimentation at SNOLAB 28
1.22 PICO-60 C_3F_8 SD and SI limits 29
1.23 PICO-60 and PICO-2L SI and SD sensitivities 30
1.24 Present and future generation PICO chambers 31
1.25 PICO-60 detector 32

2.1 GUNTER Calibration Chamber 35
2.2 Schematic cross-section view of GUNTER and ^{88}Y/Be source 37
2.3 Schematic top view of GUNTER and Y-88/Be source 38
2.4 CAD rendering of fully assembled GUNTER while compressed. 39
2.5 CAD rendering of GUNTER cross-section while expanded. 40
2.6 PICASSO experiment acoustics 41
2.7 Acoustic analysis variables for WIMP search data and neutron calibration runs . 42
2.8 PICO-60 ANN acoustic analysis 43
2.9 Acoustic identification of proton recoils 45
2.10 Preliminary calibrations of R-134a 46
2.11 Preliminary R-134a electron recoil calibrations in GUNTER 47
2.12 Projected SI and SD limits for PICO-40L 48
2.13 External pump used for GUNTER 50
2.14 Cooling and heating elements in GUNTER 50
2.15 Block diagram of a typical closed loop system. 52

2.16 Block diagram of a basic PID control algorithm 52
2.17 PID Autotuning (Temperature) VI 53
2.18 GUNTER PID temperature control optimization 54
2.19 GUNTER PID controller VI 55
2.20 Piezoelectric sensor 56
2.21 Piezo-dome gap 57
2.22 Example of piezoelectric transducer measurement and characterization system . 58
2.23 Fabrication of piezoelectric components 59
2.24 GUNTER entropy trigger VI 60
2.25 Entropy trigger 61
2.26 Basic geometry of a stereovision system 62
2.27 Outer vessel grid images for camera calibration using ANNs 64
2.28 ANN architecture for position reconstruction in GUNTER 64
2.29 Example ANN 3D position reconstruction 65
2.30 GUNTER simulation side-by-side comparison 66
2.31 Control panel of GUNTER bubble finding algorithm VI 66

3.1 Simulated rates for ^{88}Y/Be 10-35 psig pressure scan at 15°C for GUNTER C_3F_8 neutron calibration 69
3.2 Traditional Seitz model for electron recoil bubble nucleation in C_3F_8 70
3.3 Simulated energy spectra deposited in GUNTER for photons originating from external ^{133}Ba and ^{124}Sb sources 71
3.4 Ratio of measured event rates in GUNTER from exposure to ^{133}Ba and ^{124}Sb . 72
3.5 Pressure and temperature conditions of all PICO C_3F_8 gamma calibrations . . . 73
3.6 Probability of bubble nucleation per keV of energy deposited by electron recoils in C_3F_8 74
3.7 PICO C_3F_8 gamma calibration datasets 74
3.8 Comparative tests for acoustic response of alternative piezoelectric transducer designs in GUNTER 76
3.9 GUNTER average power density per bubble comparison from electron and nuclear recoils in in R-134a and C_3F_8 79
3.10 ANN architecture for acoustic classification in GUNTER 79
3.11 Temperature and pressure distributions for C_3F_8 acoustic cuts 80
3.12 Position reconstruction of C_3F_8 acoustic cuts for electron and nuclear recoil discrimination in GUNTER 80
3.13 Acoustic power from electron and nuclear recoil induced bubble events in C_3F_8 . 81
3.14 Correlation matrix for C_3F_8 acoustic classification input features 82
3.15 Overall accuracy histogram of electron and nuclear recoil acoustic discrimination in C_3F_8 and R-134a 83
3.16 Pressure distribution for electron and nuclear recoil events within 0.1 psig of each other 84
3.17 Overall accuracy histogram of electron and nuclear recoil acoustic discrimination in C_3F_8 and R-134a for stricter bounds on pressure 85
3.18 ANN output for unit vector inputs in C_3F_8 and R-134a 86

4.1 GUNTER during operation with R-134a and an ^{88}Y/Be source source 88
4.2 Stopping power and energy thresholds for bubble nucleations in R-134a 89
4.3 GUNTER acoustic output comparison of electron recoils in R-134a and C_3F_8 . . 89
4.4 Temperature (left panel) and pressure (right panel) distributions for R-134a acoustic cuts 91
4.5 Position reconstruction of R-134a acoustic cuts for electron and nuclear recoil discrimination in GUNTER. 91
4.6 Acoustic power from electron and nuclear recoil induced bubble events in R-134a 92
4.7 Correlation matrix for R-134a acoustic classification input features 93
4.8 Average power density per bubble of well-constrained electron and nuclear recoils in R-134a 94
4.9 Ratio of average spectral difference and its sum for well-constrained electron and nuclear recoils in R-134a 95
4.10 Probability of bubble nucleation per keV of energy deposited by electron recoils in R-134a 96
4.11 Probability of nucleation per unit of energy deposited for multiple pressure and temperature combinations in R-134a 97
4.12 ^{88}Y/Be photo-neutron calibration source applications 98
4.13 Fiducial volume artifacts due to reflections 99
4.14 ^{88}Y/Be 10-60 psig pressure scan at 35°C for GUNTER R-134a calibration . . . 100
4.15 Seitz threshold calculation in R-134a for different Harper factors 101
4.16 Seitz threshold calculation in R-134a for increasing pressures at fixed temperatures 102
4.17 PICO-60 best-fit efficiency curves for C_3F_8 102
4.18 Diagrams of linear threshold models for bubble nucleation efficiency 103
4.19 Simulated bubble nucleation rates in R-134a for the simplest linear threshold model 104
4.20 Energy deposited in the active volume of GUNTER by gammas emitted from the Y-88/Be source 105
4.21 Best fit comparison between all data and constrained data to bubble nucleation rates in R-134a for the linear threshold model with seven free parameters 106

ACKNOWLEDGMENTS

The path to the Ph.D. is undoubtedly an arduous one. How difficult, you ask? Picture a young boy chasing Moby Dick with nothing but a life raft and a kitchen knife, or Sisyphus pushing a mammoth boulder up a hill only to have it roll down every time it nears the top. Yet, in a way, the Ph.D. journey is a humbling reminder that to be a man is to endure, persevere in the face of adversity, and take a go at life with unfettered relentlessness. Along those lines, if I were to choose the mantra that has stuck with me through the thick and thin of the last four years, it would probably be the Persian adage my advisor, Juan I. Collar, echoed in my darkest hour as a graduate student: "this too shall pass," and so it did.

First and foremost, I want to thank my family for their unconditional support – my mother, best friend, and confidant, Sonia, who always urged me to have a plan and whose immeasurable sacrifices bore the fruits of my past and current endeavors; my stepfather, Rafa, who gave the finger to communist Cuba, left the milk processing plant, showed genuine love and devotion to my mother, taught me what it meant to be brave, and stood across from me wherever I went, especially when I had lost my way; my younger brother, Rafael Fernando, whose love and affection offers me a glimpse of what fatherhood must feel like; my late father, Rafael, for giving me such beautiful memories; my dear friend Casillas, who has stood next to me in the trenches of life for almost a decade, helping me weather so many of its storms; and my gringo compadre Mark, who made sure on multiple occasions that I wasn't sleeping out on the streets, taught me how to throw knives, and enriched every aspect of my life immensely with our camaraderie.

Secondly, I wish to thank my advisor for his tenacity and guidance and for allowing me to help create knowledge and pose questions as part of his group in this exciting field. I have never witnessed such dedication to the craft and noble tradition of science, all the while supporting me every step of the way through the trials and tribulations of the doctoral degree program. I will forever treasure Juan's innumerable teachings, stories, bantering, and words of encouragement. I could not have been more fortunate in my search for a great advisor.

Next, I would be remiss not to acknowledge friends I made along the way. In particular, I wish to sincerely thank Lee Vaasjo, Aaron Ortega, Karthik Ramanathan, Ryan Thomas, Alex Kavner, Julian Cuevas, Lukas Palm, Edgar Marrufo, Alec Hryciuk, Diego Suarez Rojas, Carlos Rascon, and Tania Labastida for their friendship, help, and input. This support network made all the difference in making it through different stages of the doctoral degree program. My graduate student experience would have been severely diminished without them.

Moreover, I want to thank Dan Baxter and my graduate student predecessors Matthew Szydagis and Alan Robinson, whose meaningful contributions served as guidance and a motivational force. Thank you to everyone from the PICO collaboration. I am more than humbled to have been a part of such an incredible collaboration. Thank you to the National Science Foundation (NSF) for its support. I am grateful to David Reid, Amy Schulz, and Young-Kee Kim for their help and support when I had just started the program, having flown over two thousand miles to make a life for myself in the City of the Broad Shoulders with nothing but a suitcase full of hot weather clothing, first month's rent, and a few physics textbooks. Lastly, I wish to thank Luca Grandi, David Schmitz, and Dan Hooper for their input and accessibility as my committee members.

ABSTRACT

The PICO-500 bubble chamber will search for Weakly Interacting Massive Particles (WIMPs) at the SNOLAB underground laboratory. This dark matter detector is expected to reach spin-dependent WIMP-nucleus cross-sections of $\approx 10^{-42}\text{cm}^2$, furthering PICO's present leadership in sensitivity to this type of coupling. Its prototype, PICO-40L, is presently operating in the same underground location. The GUNTER calibration bubble chamber, designed and assembled at the University of Chicago as part of this thesis, was operated using C3F8 and C2H2F4 (refrigerant R-134a) within its 25 c.c. active volume. These compounds are favored as WIMP scattering targets for dark matter direct detection. This thesis reports on high-statistics calibration studies from a C3F8 and R-134a filled GUNTER, aiming to confirm the sensitivity of these targets to WIMP scattering, inform upgrades in acoustic sensor design for PICO-500, find possible indications of acoustic discrimination between electron and nuclear recoils, and define optimal target run conditions for PICO-40L and PICO-500. GUNTER calibration data are also used to demonstrate a new model of bubble-nucleation by electron-recoils, casting light on the underlying physical mechanisms at work. The hydrogenated target R-134a, of interest for low-mass WIMP detection, was also studied for the first time in this role, defining the parameters that describe its response to nuclear and electron recoils.

CHAPTER 1

INTRODUCTION

Cosmology, at its core, sets out to understand the underlying mechanisms behind the origin and evolution of the universe, and the way it does this is by working to establish its composition and density in terms of matter and energy. The combination of precise cosmological measurements and astronomical observations led to the development of a model that explains much of what we observe in the known universe. The adiabatic cold dark matter (ΛCDM) model places us in an inflationary universe whose makeup is distributed between baryonic matter (5%), dark matter (27%), and dark energy (68%), which affects the universe on the largest scales and is considered responsible for the accelerating expansion of the universe (Peebles, 1994). Hence, the visible universe constitutes only a tiny fraction of the universe as a whole. Therefore, the remaining component is alluded to as dark since it does not interact electromagnetically, i.e., cannot be directly observed. An image of the ΛCDM model is shown in Figure 1.1.

Traditionally, the term dark matter has referred to missing gravity at large cosmic scales. The name was coined in the 1930s by Fritz Zwicky. He used the virial theorem to discover a gravitational anomaly in extragalactic nebulae and infer the unseen dark matter necessary for describing the evolution of the universe and the gravitational acceleration within galaxies (Zwicky, 1933). Many years later, a study of galaxy rotation curves in the late 1970s by Vera Rubin led to the first strong evidence for dark matter (Rubin, 1978), and experiments would go on to confirm her results in subsequent decades. An example of the rotation curve model is shown in Figure 1.2. In particular, the total galactic mass attributed to visible matter failed to explain why stars at the edges of spiral galaxies were gravitationally bound to the universe when their velocities were high enough to suggest otherwise. Precise big-bang nucleosynthesis theories took this further by requiring the dark matter to be nonbaryonic (Schramm and Turner, 1998). Additionally, the physics of structure formation needed dark

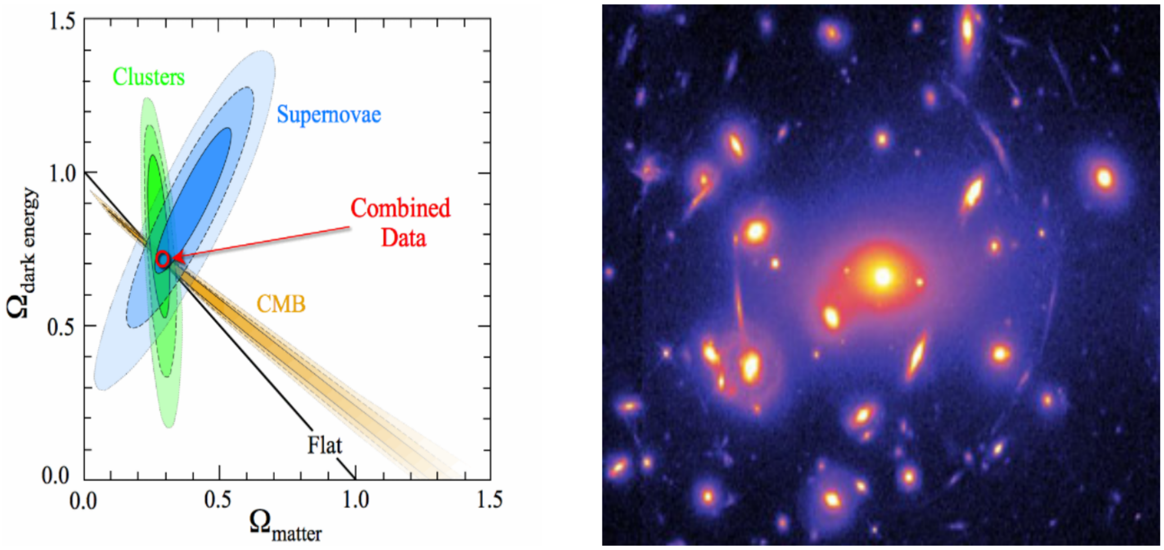

Figure 1.1: Left: the ACDM model represented as the best fit to the combination of a wide range of cosmological and astronomical data. Right: image of arcs and rings of galaxies formed via gravitional lensing due to dark matter between galaxies and the observer. Figure courtesy UCL Dark Matter.

matter to be non-relativistic (Blumenthal et al., 1984). However, it is worth noting that a solution to dark matter is unattainable via the Standard Model (SM) of particle physics alone. The WIMP hypothesis, if confirmed, is expected to open the door to Beyond Standard Model (BSM) physics and the extrapolation to Grand Unified Theory (GUT) scales. At the time of writing, dark matter remains one of the most elusive problems in modern physics despite universal consensus on its existence and scientific urgency.

The PICO experiment is one of many search efforts working toward the direct detection of dark matter in the form of stable and heavy Weakly Interacting Massive Particles or WIMPs (Steigman and Turner, 1985) (see Figure 1.3). This well-motivated dark matter candidate also arises naturally in multiple supersymmetric (SUSY) extensions to the SM (Munoz, 2017). In 2013, the merger of the Project In Canada to Search for Supersymmetric Objects (PICASSO) and the Chicagoland Observatory for Underground Particle Physics (COUPP) collaborations led to the formation of the PICO collaboration for WIMP search experiments. PICO exploits superheated liquids in bubble chambers to achieve superior background rejec-

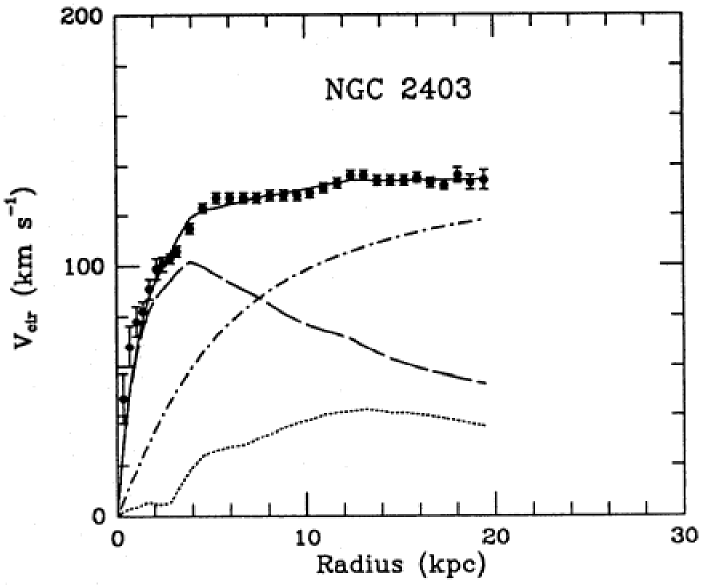

Figure 1.2: Example of a three-parameter dark-halo fit (dotted: gas, dashed: disk, dash-dotted: halo) to the rotation curve model for NGC 2403. Figure from Begeman et al. (1991) reproduced with permission.

tion in the field of WIMP direct detection experiments. This thesis summarizes the recent results from GUNTER, a superheated bubble chamber assembled and deployed at the University of Chicago under a modest overburden of 6 meters of water equivalent (m.w.e.) in the Michelson Center for Physics. This is sufficient to reduce cosmic ray backgrounds to levels that make their interference negligible for present studies. GUNTER was designed for high-statistics calibration studies using targets C_3F_8 and R-134a and as a testbed to inform the next-generation PICO bubble chamber design.

This chapter outlines the case for why WIMPs are the most compelling class of candidates for dark matter, followed by a survey of the multiple approaches at detection and the specific advantages of bubble chambers for WIMP direct search experiments. Chapter 2 focuses on the wide-ranging motivation behind GUNTER, covering its mechanical design, control software, and general structure and introducing the studies of interest that make up the bulk of this thesis. Chapter 3 contains the GUNTER calibration results and studies for C_3F_8. Lastly, Chapter 4 includes the GUNTER calibration results and studies for the hydrogenated

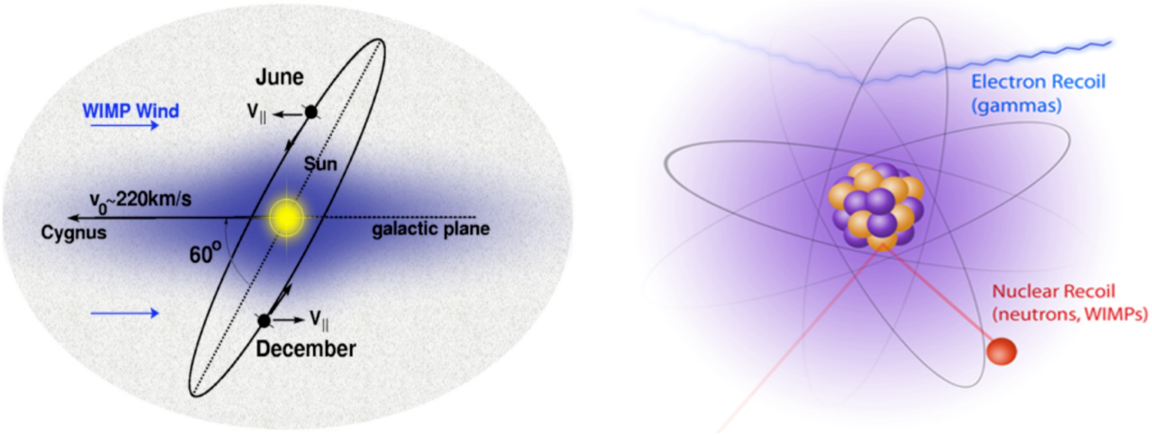

Figure 1.3: Left: dark matter represented as an extended halo encompassing the Milky Way. Right: diagram of electron and nuclear recoils as scattering off regular nuclei. Figures courtesy UCL Dark Matter.

target R-134a.

1.1 WIMP Dark Matter

Based on the ΛCDM model, the assumption is as follows: a yet undiscovered form of matter which is non-baryonic and non-relativistic accounts for close to 85% of the matter content of the Universe and nearly 27% of its energy budget (Ade et al., 2016). Among the potential candidates, we find axions (Battesti et al., 2008), primordial black holes (Carr et al., 2010), and WIMPs (see Figure 1.3). These studies include but are not limited to cosmic microwave background (CMB) (Tanabashi et a1., 2018), galaxy clusters (Beck, 2019), distant supernovae (Farnes, 2017), and expansion rate via baryon acoustic oscillations (Bernal et al., 2020). Cold Dark Matter (CDM) has played a crucial role in explaining large-scale structure formation since its theoretical predictions substantially align with observations (Blumenthal et al., 1984). A fit to the ΛCDM model using measured CMB power spectra is shown in Figure 1.4. WIMPs are compelling candidates because they both satisfy all the necessary conditions for dark matter and arise naturally via multiple SUSY extensions to the SM. They represent the lightest SUSY particle, the neutralino WIMP (Jungman et al., 1996).

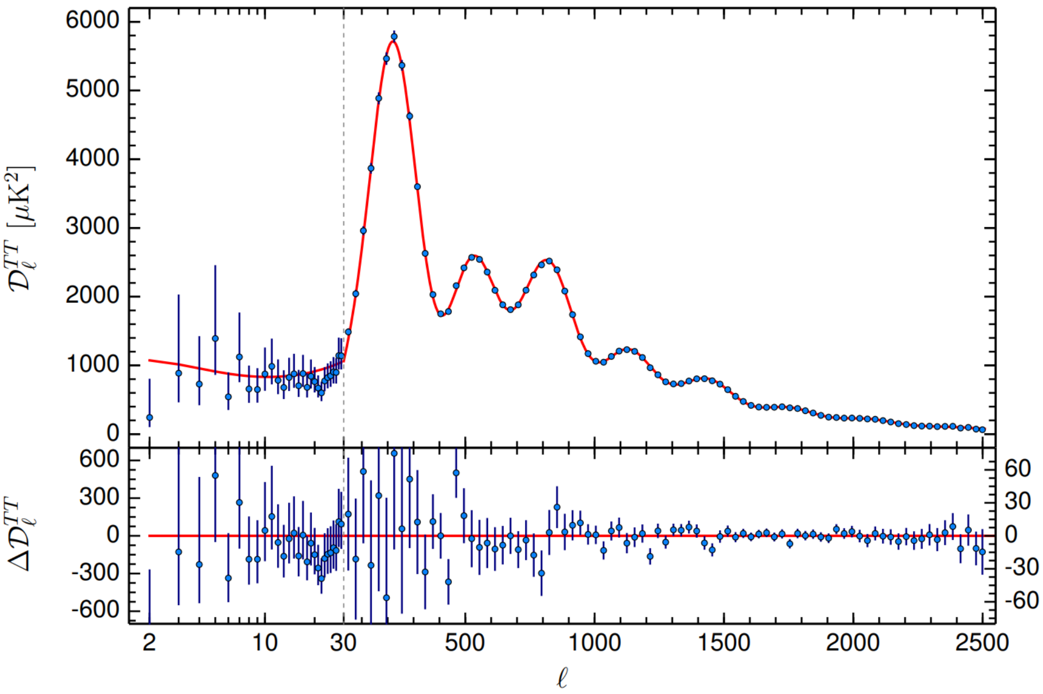

Figure 1.4: Measured temperature and temperature-polarization CMB power spectra (blue) and fit to the ACDM model (red). Figure from Ade et al. (2016) reproduced with permission.

This section summarizes the merits of the WIMP dark matter model, which has undergone extensive experimental scrutiny and remains a strong focus today.

Primordial abundances of light nuclei from standard Big Bang nucleosynthesis and CMB predictions are shown in Figure 1.6. Assuming WIMPs were in thermal equilibrium with other SM particles in the brief period just after the Big Bang, as the universe reached temperatures below the WIMP mass m_χ and the expansion rate H exceeded the rate of annihilation to creation, these WIMPs dropped out of thermal equilibrium and remained as thermal relics (see Figure 1.5). Hence, a fixed relic density for WIMPs arises, which is independent of m_χ and inversely proportional to $\langle \sigma_a \nu \rangle$,

$$\Omega_\chi = \frac{m_\chi n_\chi}{\rho_c H^2} \sim \frac{10^{-26}\mathrm{cm}^3/\mathrm{s}}{\langle \sigma_a v \rangle}, \tag{1.1}$$

where n_χ is the WIMP number density, σ_a is the average annihilation cross section, v is

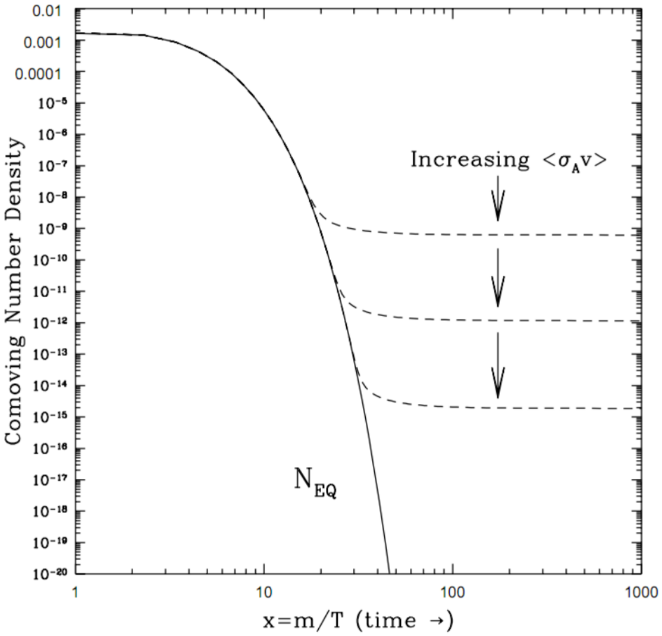

Figure 1.5: Solid line is the thermal relic WIMP density remains in equilibrium as the universe expands and cools down, and the dotted lines are WIMP freeze-out densities at different annihilation cross-sections. Figure from Kolb and Turner (1994) reproduced with permission.

the thermal velocity, and the critical density ρ_c is defined as in the Friedmann equations (Friedmann, 1922). Refer to Jungman et al. (1996) for an intricate explanation of this process. By definition, the annihilation cross-section is set around the weak scale

$$\langle \sigma_a v \rangle \sim \alpha^2 (100\text{GeV})^{-2} \sim 10^{-25}\text{cm}^3/\text{s}. \tag{1.2}$$

A surprising consequence of this, based on Equation 1.1, is that WIMP thermal relic density rests at $\Omega_\chi \sim 0.1$, on precisely the same scale needed by any cosmological argument, implying that the role of dark matter can be naturally filled by any stable particle generated via new physics at the electroweak scale. Thus, it is generally assumed that weak-scale interactions lead to the WIMP in question.

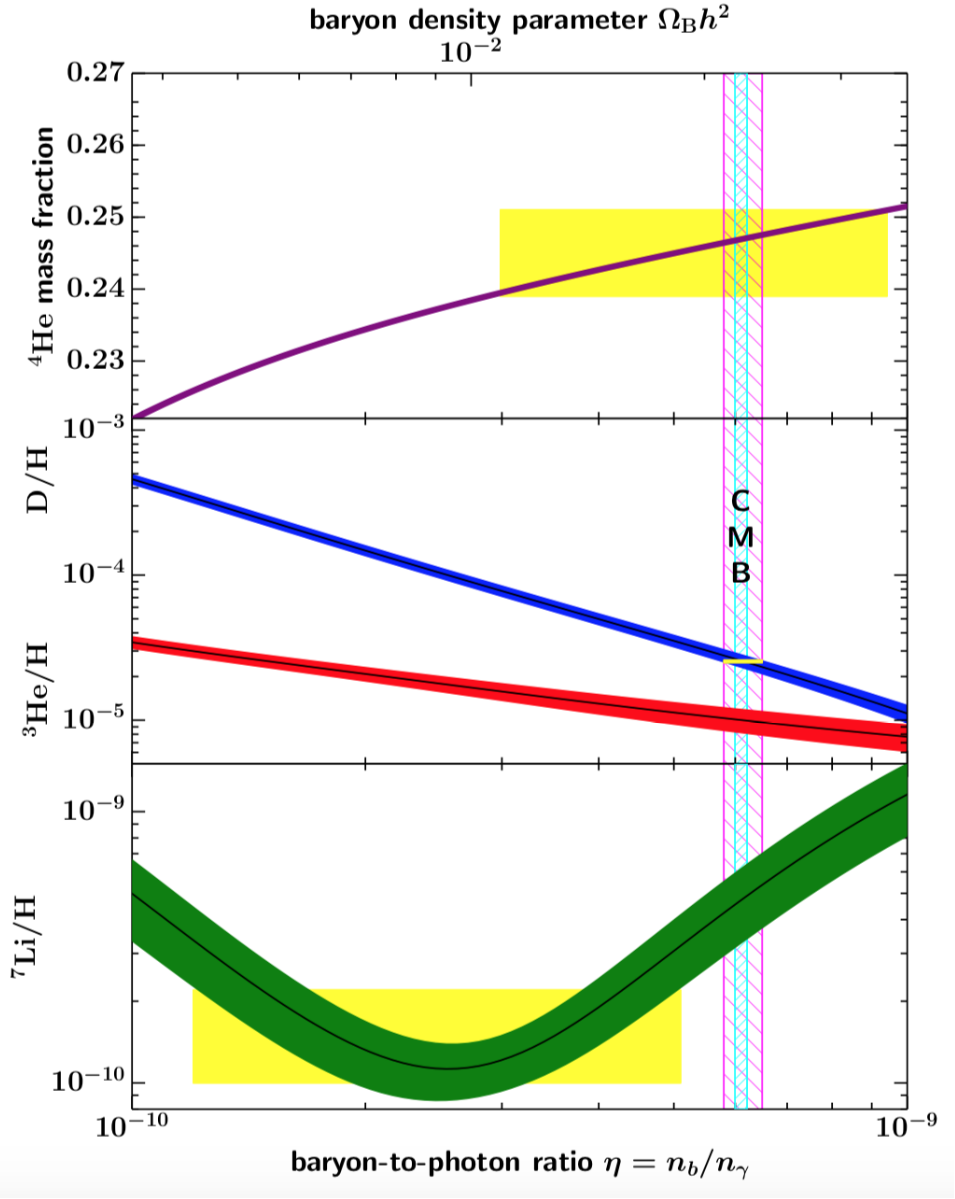

Figure 1.6: Schramm plot depicting primordial abundances of light nuclei arising from standard Big Bang nucleosynthesis and CMB predictions. Figure from Tanabashi et a1. (2018) reproduced with permission.

1.2 WIMP Detection

The direct observation of dark matter would lead to a better understanding of its composition and properties. Hence, decades of experimental effort have sought out to do just that. Assuming dark matter comprises WIMPs distributed throughout galactic halos, they should scatter elastically off target nuclei in a detector via weak interaction with some frequency related to the strength of the WIMP-nucleon cross-section. This cross-section can be either spin-dependent (SD) or spin-independent (SI). For SI interactions, the amplitude is proportional to the number of nucleons. In SD interactions, the amplitude sign is flipped if the spin of a nucleon is reversed. The two fundamental SD cross-sections are WIMP-proton and WIMP-neutron. As such, the details of the target nucleus become important in SD WIMP-nucleon experiments, as it does in PICO experiments. This section briefly surveys multiple approaches at nuclear recoil detection, along with different WIMP search experiments. A detailed derivation of the differential WIMP recoil spectrum is found in Lewin and Smith (1996), and a thorough review of WIMP models, searches, and constraints is provided by Arcadi et al. (2018).

1.2.1 Direct Detection Methods

Generally, direct detection experiments work toward setting upper limits on the rate of WIMP-nucleon scattering at specific recoil energies, which in turn provides a limit on the total event rate for each choice of dark matter mass m_χ. The limits set on the largest elastic scattering cross-sections allowed by the data of each experiment are commonly expressed as exclusion plots in cross-section versus WIMP mass phase space (see Figure 1.6).

The differential scattering rate for WIMP-nuclei can be written as

$$\frac{dR(E,t)}{dE} = \frac{N_T \rho_\chi}{m_\chi m_A} \int_{v_{min}}^{v_{esc}} v f_E(\mathbf{v},t) \frac{d\sigma(v,E)}{dE} d^3\mathbf{v}, \tag{1.3}$$

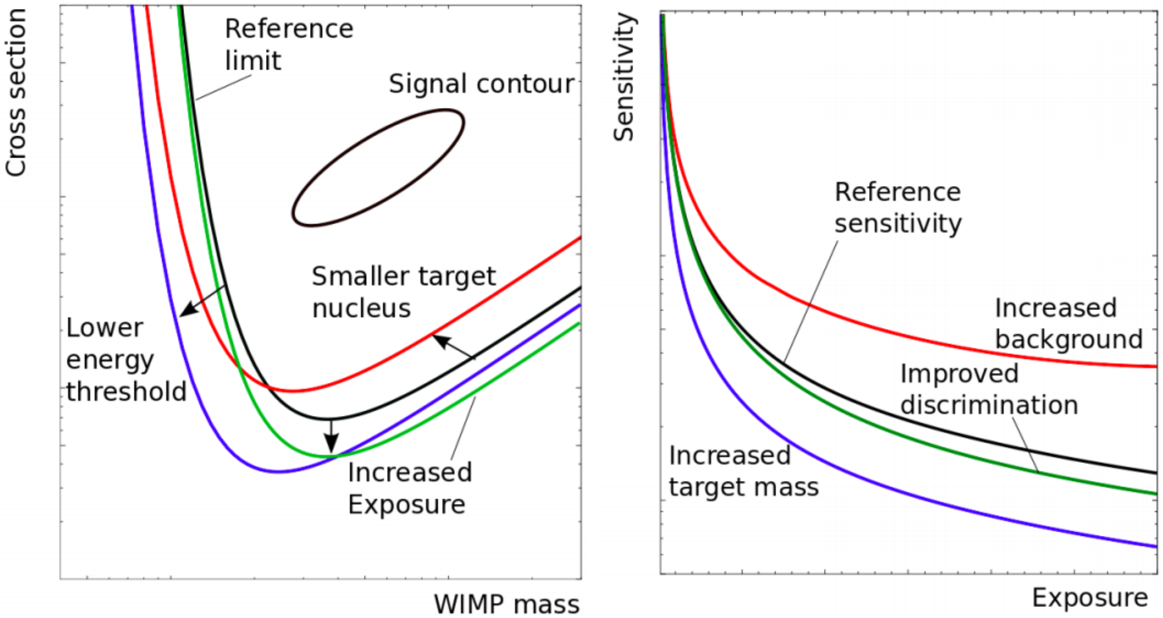

Figure 1.7: Left: illustration of the generic result from a direct dark matter detection experiment. Right: illustration of how sensitivity evolves as a function of exposure. Figure from Marrodan, Undagoitia, and Rauch (2016) reproduced with permission.

where E is the scattering event recoil energy, N_T is the ratio of target nuclei to a kilogram of the detector, ρ_χ is the local dark matter density, $\mathbf{v}$ is the velocity of the dark matter particle relative to the Earth, $f_E(\mathbf{v}, t)$ is the distribution of WIMP velocities in the frame of the Earth, $v_{min} = \sqrt{m_N E/(2\mu^2)}$ is the minimum WIMP speed necessary for the production of detectable events with energy E, and v_{esc} is the escape velocity for a WIMP gravitationally bound to the Milky Way. The WIMP-nucleus reduced mass is written in terms of the nucleus mass m_N and dark matter mass $\mu = m_\chi m_N/(m_\chi + m_N)$. The differential cross-section term for the WIMP-nucleus scattering is typically written as

$$\frac{d\sigma(v,E)}{dE} = \frac{m_N}{2\mu^2 v^2}(\sigma^{SI}F^2(q) + \sigma^{SD}S(q)), \tag{1.4}$$

where q is the momentum transfer, and $F^2(q)$ and $S(q)$ are the SI and SD form factors, respectively, as described in Schnee (2011).

Background rejection is achieved using the detector response to electron and nuclear scattering, depending on the experiment. WIMP signal sensitivity is determined by a combination of factors such as target nucleus, energy threshold, and control over the background and exposure (see Figure 1.6). The target nucleus affects the sensitivity to low and heavy WIMP masses and the constraints set on detectable SD scatterings. The energy threshold refines direct detection limits on the scattering cross-section by driving the sensitivity toward low WIMP masses. In contrast, control over the background and exposure is used to establish the overall sensitivity of the experiment, allowing for lower limits in scattering cross-sections.

1.2.2 Indirect Detection Methods

Indirect detection of dark matter candidates consists of searching for WIMP annihilation byproducts over expected galactic or extra-galactic scale backgrounds using Earth earth-based telescopes (Ackermann et al., 2015) or satellites (Albert et al., 2017). The WIMP annihilation signal is sought via the detection of gamma rays, cosmic rays, and neutrinos. This section expounds briefly on the gamma-ray flux channel from WIMP annihilation as an example of an indirect detection method (see Figure 1.7).

Models predict that for large enough densities ($\rho = n_\chi m_\chi$), the collision and subsequent annihilation of two WIMP particles produces a flux of gamma rays that should be observable. The differential flux from annihilation is found to be

$$\frac{d\Phi}{d\Omega dE} = \frac{\sigma v}{8\pi m_\chi^2} \times \frac{dN}{dE} \times \int_{l.o.s.} ds \times \rho^2(\vec{r}(s,\Omega)), \tag{1.5}$$

where Ω is the solid angle within which the volume of the sky was observed, σ is the current WIMP annihilation cross-section, v is the mean WIMP velocity, and dN/dE is the energy spectrum. From Equation 1.5, it is worth noting that indirect detection explores complementary properties of dark matter particles because the sensitivity ranges from WIMP mass to how it is distributed and the current annihilation cross-section, which is potentially different

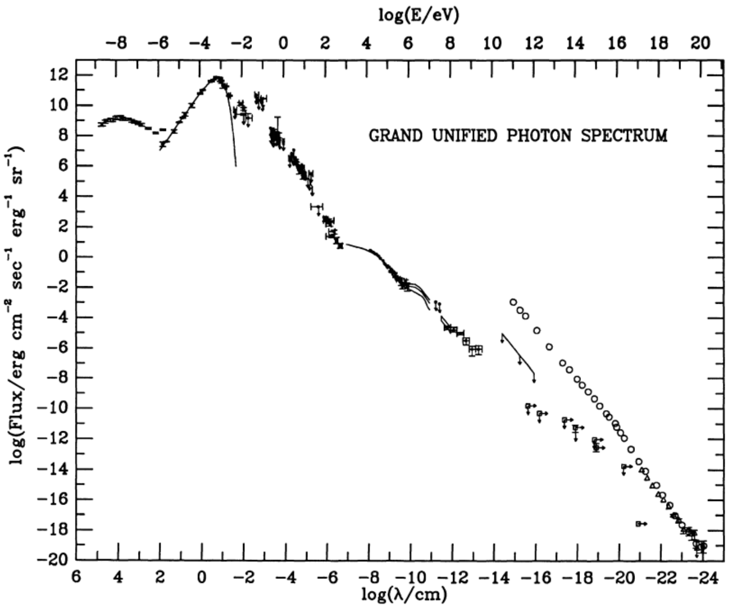

Figure 1.8: An example plot of the diffuse extragalactic photon background. Horizontal arrows correspond to upper limits, and vertical arrows indicate integrated flux. Open circles and triangles correspond to gamma rays and hadrons, which make up the total cosmic ray flux. Figure from Ressel and Turner (1990) reproduced with permission.

from that found for the relic density. Suppose no excess signal is observed upon measuring gamma-ray flux and comparing it to the expected backgrounds. In that case, the dark matter density profile is adjusted to select the annihilation final state needed for dN/dE, setting a limit on the ratio $\sigma v/m_\chi^2$ according to Equation 1.5. Notwithstanding, intricate numerical tools such as a likelihood calculator of dark matter detection have been developed (Huang et al., 2017). A final feature worth noting when exploring WIMP models via indirect detection is the fact that if the annihilation cross-section σv is velocity independent, then the bounds on the current σv relate directly to that of the dark matter relic density (Griest and Seckel, 1991).

1.2.3 Collider Searches

Alternatively, collider experiments search for dark matter production evidence, with such searches having been completed at the Large Hadron Collider (LHC) by the ATLAS and

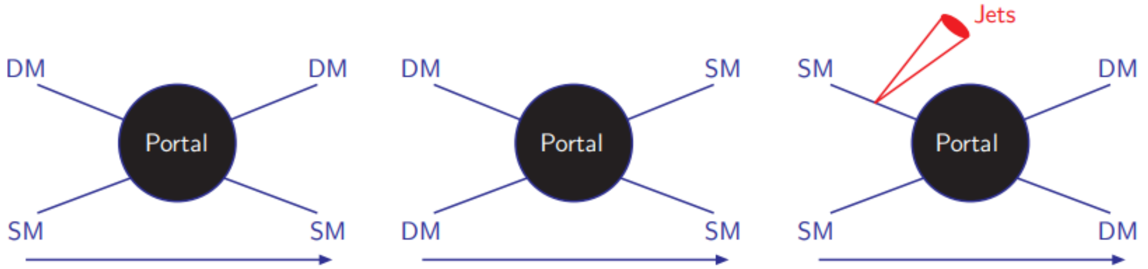

(a) Direct Detection **(b) Indirect Detection** **(c) Collider Detection**

Figure 1.9: Detection type illustration of dark matter interactions with SM particles. At the moment of writing, the knowledge about how these interactions occur is unknown. Figure from Arcadi et al. (2018) reproduced with permission.

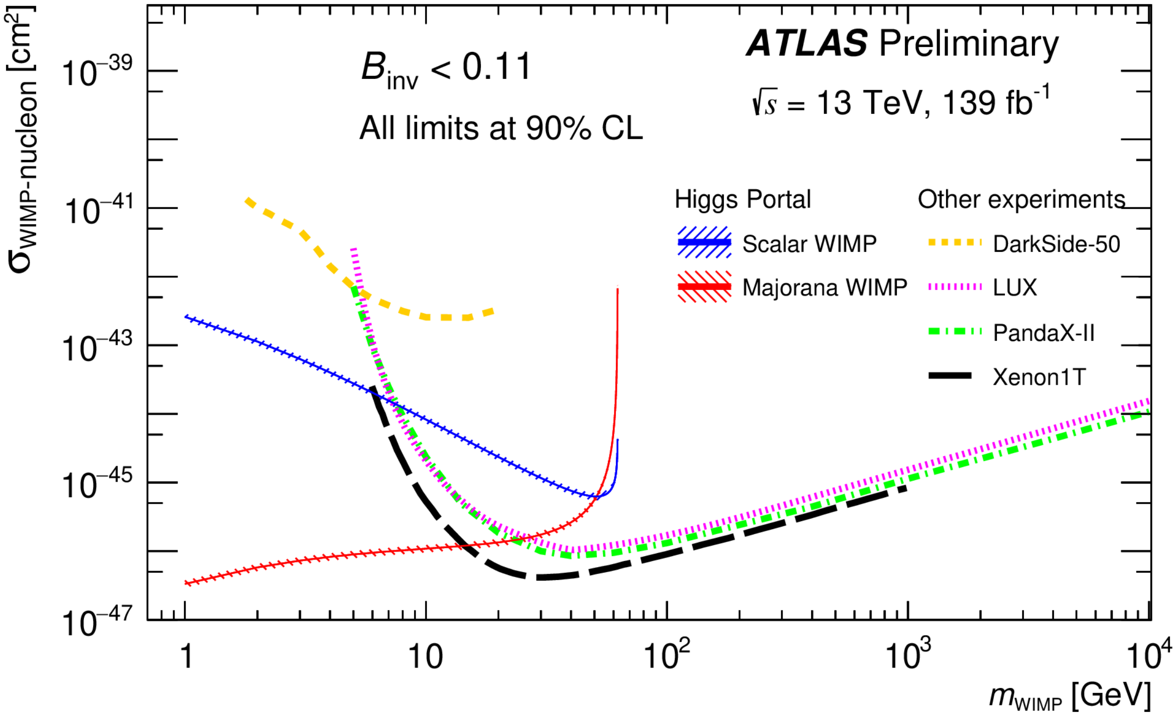

Figure 1.10: Comparison between direct detection experiments and the upper limit set on the WIMP nucleon cross-section via collider searches at 90% confidence level. Figure courtesy ATLAS Collaboration/CERN.

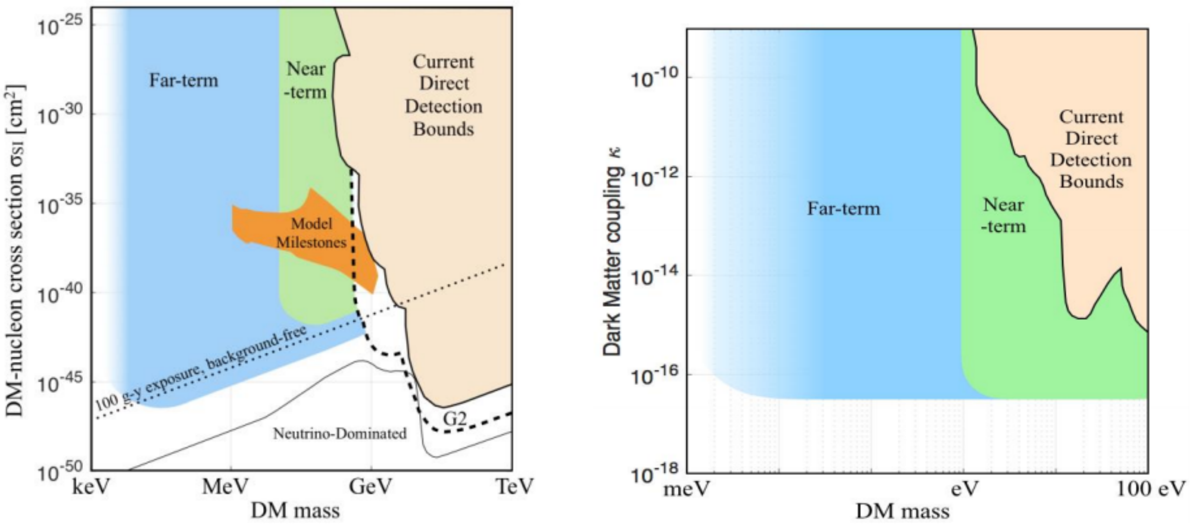

Figure 1.11: Theoretical targets as shown in the BRN report. Current PICO efforts aim to considerably expand sensitivity into the Model Milestones and Near-Term shaded regions shown in orange and green, respectively. Figure from Kolb et al. (2018) reproduced with permission.

CMS collaborations (see Figure 1.9). Collider efforts probe high-energy proton-proton collisions, theoretically leading to WIMP production in association with detectable particle byproducts (see Figure 1.8). The basic idea is that WIMPs would manifest themselves as missing transverse momentum (energy) since they are stable and electrically neutral. Mono-X searches, for example, look at charged leptons and photons as visible counterparts for WIMP production (Tolley, 2016). These types of searches filter events with considerable missing energy to improve background rejection and increase visibility in a potential WIMP signal event. That said, collider searches can only confirm or deny candidate particles' presence via missing energy events, therefore disqualifying them from uniquely ascertaining the existence of WIMPs in a signal event (Arcadi et al., 2018). Refer to Cui (2015) for an in-depth review of WIMP baryogenesis mechanisms and its detection channels in collider experiments.

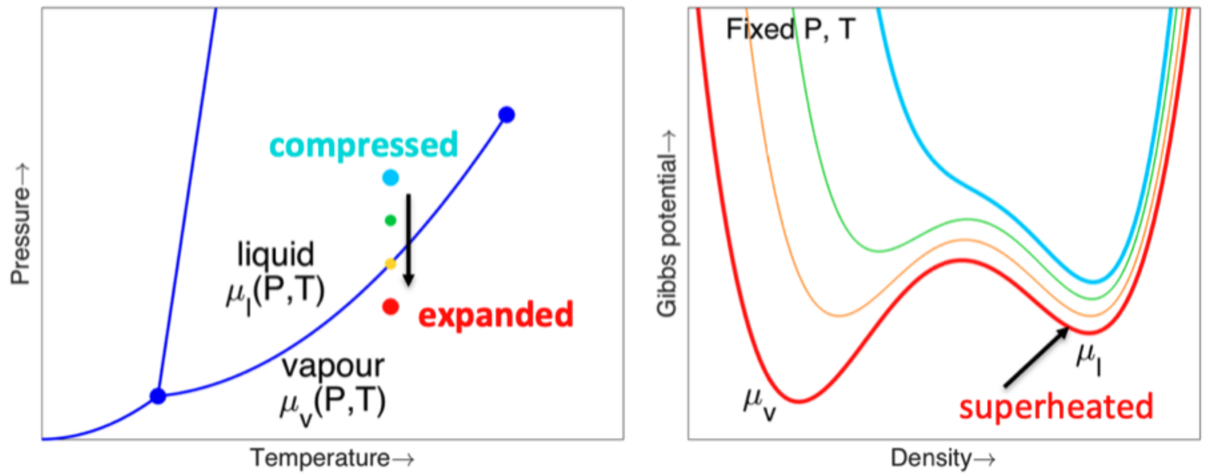

Figure 1.12: Left: generic phase diagram of a superheated liquid, highlighting the processes of compression and expansion in between phase regions for a fixed temperature. Right: Gibbs potential of a superheated liquid for varying density at fixed pressure and temperature. Figure courtesy E. Dahl (private communication).

1.3 PICO Bubble Chambers

The PICO collaboration has produced leading limits for WIMP searches via SD proton couplings with outstanding electron recoil insensitivity (Amole et al., 2019). Recent collaboration efforts have focused on developing successful PICO bubble chambers as low-mass dark matter detectors by repurposing existing infrastructure to exploit hydrogen-rich targets, which would allow for visibility of nuclear recoils from sub-GeV dark matter. This work ultimately aims to explore uncharted parameter space and further the collaboration's leadership in bubble chamber dark matter searches. A detailed overview of dark matter research targets is found in the recent Basic Research Needs for Dark Matter Small Projects New Initiatives (BRN) report (Kolb et al., 2018). The theoretical targets from the BRN report are shown in Figure 1.11.

PICO deploys bubble chamber superheated targets to search for WIMP dark matter and has maintained leadership in spin-dependent WIMP-proton matter interaction limits using freon-based bubble chambers. (see Figure 1.12). Measures of acceptable electron recoil background drive the current operating threshold of its detectors. PICO bubble chamber detectors use a combination of optical, acoustic, and pressure sensors to identify the candidate nuclear recoils in the bulk of the active mass of the detector. Energy deposition events responsible for producing bubbles via nucleation are captured by cameras, while piezoelectric acoustic sensors measure the acoustic power released as the result of rapid bubble expansion. All the while, pressure transducers, and thermocouples register the thermodynamic state of the bubble chamber. Bubble chambers, in principle, provide excellent rejection of all types of radioactive background. Moreover, bubble chamber technology offers the most flexible direct detection techniques since they can operate with any fluid of choice.

This section focuses on the theory of bubble chamber operation and the advantages of superheated liquids for dark matter detection. The Seitz theory, described in the following section, explains bubble nucleation in showing that radiation must surpass thresholds of both energy and stopping power to allow for the formation of a bubble. Hence, this threshold system enables bubble chambers to trigger on high stopping power charged nuclei (~ 1 MeV/μm) while rejecting electrons of much lower stopping power (< 0.01 MeV/μm) (Fustin 2012).

Initially devised as a radiation detector for high-energy experiments (Glaser, 1952), the bubble chamber exploits superheated liquids for WIMP direct detection experiments. A bubble chamber detector is considered superheated when the temperature is held constant, and the pressure is slowly decreased below the vapor pressure of the liquid, in what is commonly referred to as expansion (Glaser, 1952). Superheated liquids remain in a liquid state past their boiling points or below their vapor pressure. The condition for vaporization requires a nucleation site in the form of either a pocket of gas due to impurities in the liquid or container or a particle interaction whose energy and stopping power are above the thresholds set by the liquid's current thermodynamic state. The superheated liquid's stability is determined by the degree of superheat, defined as the difference between the

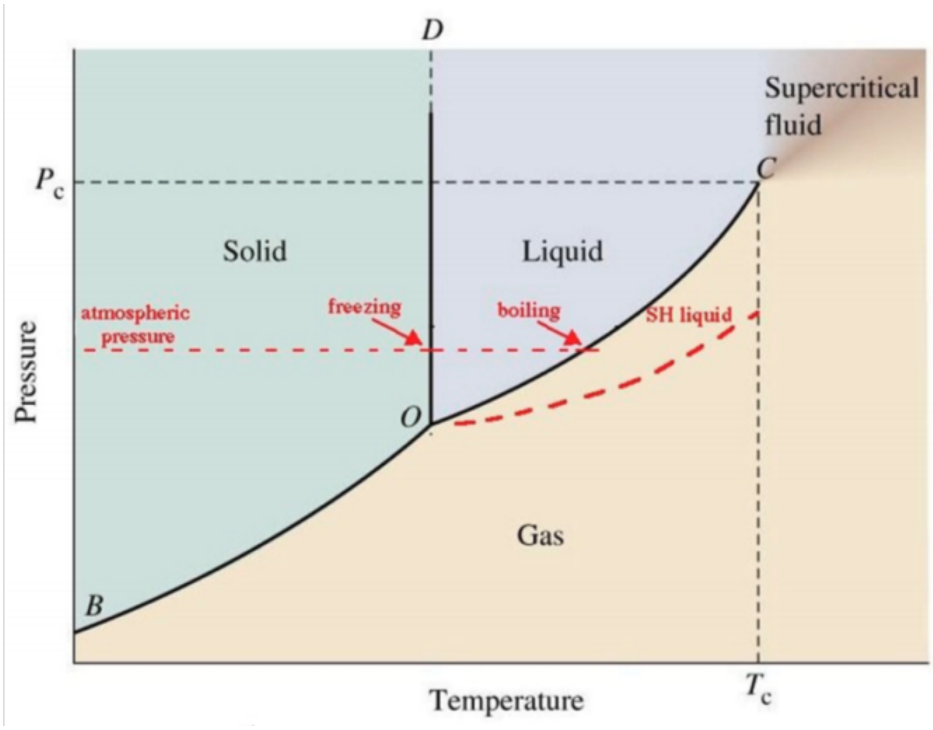

Figure 1.13: Phase diagram illustrating the thermodynamics of a superheated liquid. The red dashed curve defines the superheated region reachable by decreasing the pressure or increasing the temperature of a stable liquid. Figure courtesy J. I. Collar (private communication).

liquid's vapor pressure and the operating pressure at operating temperature. Figure 1.13 depicts an example phase diagram for the thermodynamics of a superheated fluid.

Current bubble chamber iterations use newer techniques that allow for high purity levels in fluids and deactivation of surface event sources in the containers (Bolte et al., 2007). This has led to bubble chamber designs without stubborn nucleation sites leading to instability (fluid vaporization). Building upon these developments, bubble chambers can now operate for nearly indefinite periods, significantly improving their viability for rare event searches with low background and an expected low signal rate.

Two thresholds need to be surpassed during particle interactions in bubble chambers for bubble nucleation to occur: a minimum of energy deposition and stopping power, i.e., energy deposition per unit length traversed by the particle (see Figure 1.14). The two tunable parameters in a bubble chamber, operating pressure and temperature, define these thresholds, which are lowered as the fluid's degree of superheat —the departure from a stable liquid depicted in Figure 1.14— is increased. Simply put, there needs to be sufficient energy in a sufficiently localized region (i.e., local heating) for bubble nucleations to occur. For example, it is common for electrons not to have enough stopping power to be above thresholds for low degrees of superheat, leaving only nuclear recoils from potential WIMP scattering able to produce nucleations (see Fig. 1.13). Alpha particles and their recoiling daughters can still be nucleation sources, but it is possible to discriminate against them acoustically (subsection 1.3.2). At high degrees of superheat (high temperature or low pressure), the virtue of being insensitive to minimum ionizing particles such as electrons is lost. This defines the minimum recoil energy detected using this technique, typically of order 1 keV.

1.3.1 Seitz Theory

The heat input required to form a critically sized bubble has been traditionally described using the Seitz 'hot-spike' threshold model. According to this model, a particle that deposits

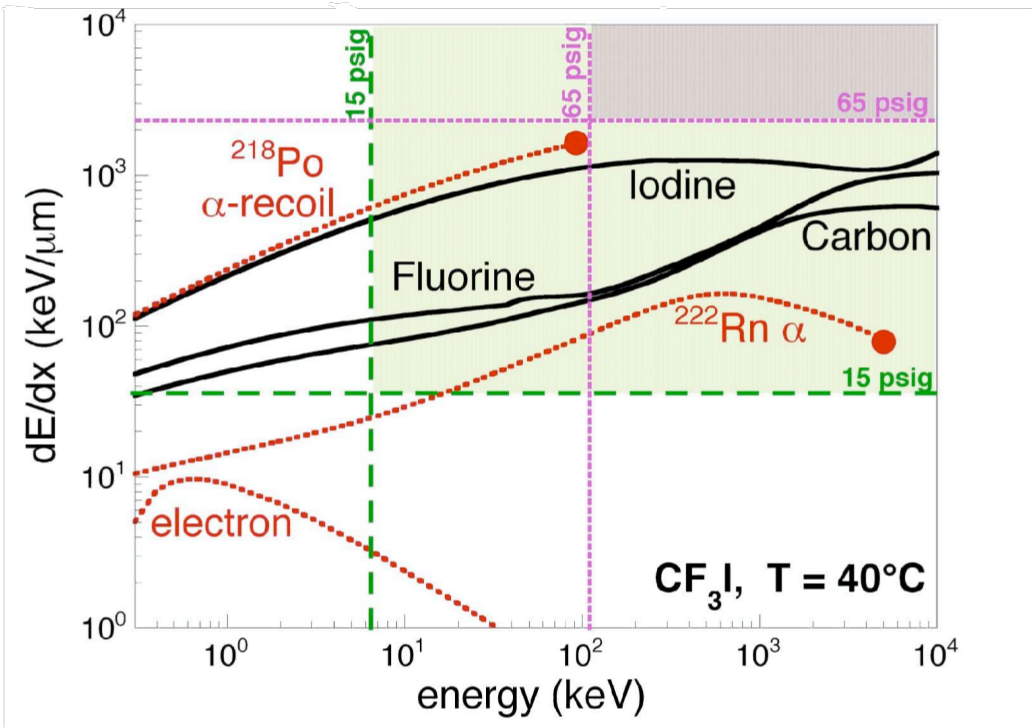

Figure 1.14: Instantaneous stopping power (dE/dx) versus energy for different particles in CF_3I, including its three recoiling species, electrons, alphas and alpha-recoils. Only particles in the thermodinamically-defined upper right quadrants can produce bubbles, by surpassing minimum energy and dE/dx thresholds. Examples of these thresholds are provided for two operating pressures. Figure from Collar et al. (2008).

enough energy can produce a phase change that leads to the formation of a vapor bubble of radius r when it interacts (e.g., via a WIMP or neutron-induced nuclear recoil or a gamma-induced electron recoil). The bubble chamber theory of operation was formulated by Seitz, who stated that if an energy spike is larger than Q, the Seitz threshold, and concentrated within a radius less than r_c, the critical radius, then a proto-bubble can grow into a macroscopic bubble (Seitz, 1958). The critical radius is defined as

$$r_c = \frac{2\sigma_{surf}}{P_b - P_l}, \tag{1.6}$$

where σ_{surf} is the surface tension, P_b is the pressure of the gas bubble, and P_l is the superheated liquid pressure. The Seitz threshold for nucleation is a function of surface tension and liquid vaporization terms

$$Q = 4\pi r_c^2(\sigma_{surf} - T\frac{\partial\sigma_{surf}}{\partial T}) + \frac{4}{3}\pi r_c^3 \rho_b(h_b - h_l), \tag{1.7}$$

where T is the operating temperature, ρ_b is the density of the bubble gas, and h_b and h_l are the specific enthalpies of the gas bubble and the superheated liquid. This critical energy for bubble formation is described by three work terms: the work required to vaporize the fluid, the work required to form the surface, and the work done against external pressure. Hence, it is typically described as the much larger sum of these reversible works. Formally expressed, the energy requirement becomes

$$E > E_c = \frac{4\pi r_c^2 \sigma_{surf}}{3\epsilon}, \tag{1.8}$$

which is a compact form of Equation 1.7 permitted by making

$$\epsilon = 4\pi r_c^2 \sigma_{surf}/3Q = 4\pi r_c^2 \sigma_{surf}/3E_c'. \tag{1.9}$$

It must be emphasize that ϵ as correctly defined in Equation 1.9 is not a free parameter. It is possible to accurately calculate it for each refrigerant and operating condition and compare it with experimental measurements (Collar, 2000). The NIST REFPROP (Lemmon et al. 2018) program was used to calculate the thermodynamic properties of C_3F_8 and R-134a arising from the equations of state found in Lemmon and Span (2006) and Lemmon and Jacobsen (2004), respectively. These thermodynamic properties are necessary to calculate the Seitz model parameters for C_3F_8 and R-134a. A detailed derivation of the Seitz hot-spike threshold can be found in Appendix A of Amole et al. (2019).

Furthermore, the Seitz model imposes a second threshold, the energy threshold being the one just described. The second threshold requires deposition of energy greater than E_c in a space much smaller than the critical range L_c, which is proportional to r_c. Simply put, this second condition asks whether or not sufficient energy was deposited locally to allow for the formation of a proto-bubble. When only the stopping power threshold is met, the Seitz threshold becomes E_c. This second threshold is typically formulated by adding an instantaneous stopping power threshold

$$\frac{\mathrm{d}E}{\mathrm{dx}} > \frac{E_c}{a r_c}, \tag{1.10}$$

where a is a dimensionless scaling parameter with a history of different interpretations and measured values (Bell et al., 1974; Harper and Rich, 1993). For example, Bell et al. (1974) obtained a theoretical value of $a = 6.07$, although values of $a = 2$ (Apfel, 1979), $a = 2\pi$ (Norman and Spiegler, 1963), and even $a = 12.96$ (El-Nagdy and Harris, 1971) can be found in the literature. Within the collaboration, a is informally referred to as the ‘Harper’ factor. For convenience, this terminology will be adopted when referring to a for the remainder of this thesis. The SRIM program (Ziegler, Biersack, and Ziegler 2008) was used to simulate nuclei stopping in C_3F_8 and R-134a. The stopping and range calculations facilitated by the SRIM program allowed for calculating the instantaneous stopping power threshold for bubble nucleation.

The double threshold nature of the bubble chamber is illustrated in Fig. 1.14. The relationship between the instantaneous stopping power of recoils and given energy showcases the strength of the bubble chamber as a WIMP detector. Varying temperature and pressure set-points for bubble chamber operation allows for the tuning of energy and stopping power thresholds to greatly minimize electron recoils as a potential background. It is worth noting that since the stopping power threshold is inversely proportional to E_c, it can be neglected to first order when the bubble chamber is operated at low energy thresholds.

The critical range L_c is usually experimentally constrained since it is not a precisely known quantity. However, it has been shown to vary with both the properties of the liquid being superheated (Poesposoetjipto and Hugentobler, 1970) and with temperature (Das and Sawamura, 2004). The critical range ($L_c = ar_c$) used in Equation 1.14 is typically replaced with one that varies with fluid density

$$L_c = b\Big(\frac{\rho_b}{\rho_l}\Big)^{1/3} r_c, \tag{1.11}$$

where b is an dimensionless scaling parameter and $r_c(\rho_b, \rho_l)^{1/3}$ represents the radius of a fluid volume that creates a critical bubble when vaporized (Poesposoetjipto and Hugentobler, 1970). Lastly, b is allowed to scale with temperature to account for temperature variation.

1.3.2 Advantages of Superheated Liquids

This section describes some of the critical advantages of using superheated liquids as dark matter detectors. They provide an alternative to the traditional detectors that rely on electron and nuclear recoil discrimination to distinguish background events from dark matter signals. These bubble chambers are operated deep underground to minimize cosmic-induced backgrounds to a great extent (Duncan, Noble, and Sinclair, 2010). Natural radioactivity

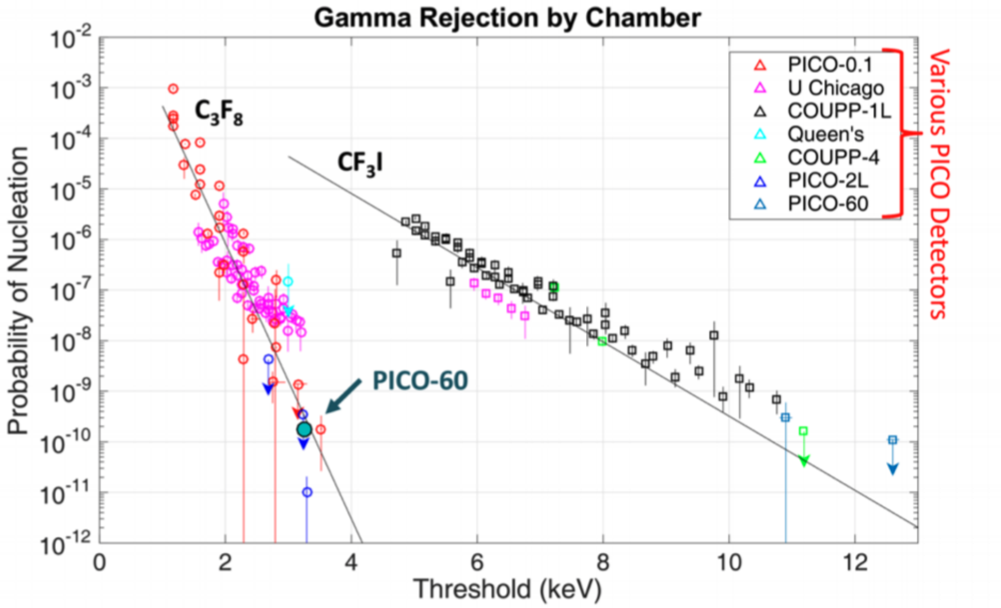

Figure 1.15: Background rejection in PICO bubble chambers with intrinsic electron recoil insensitivity in CF_3I and C_3F_8. Highlighted in teal is a rejection of 10^{-10} as the normal operating threshold for the PICO-60 detector.

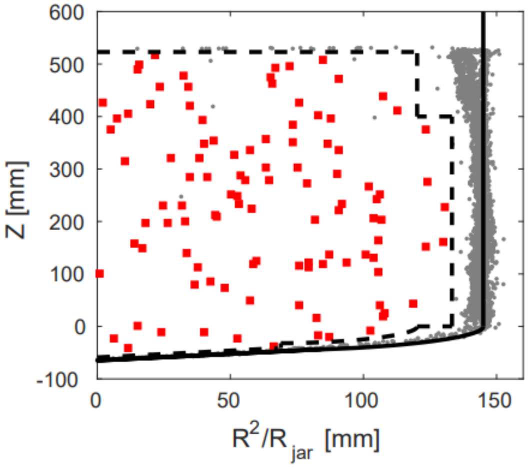

Figure 1.16: Single-bubble event spatial distribution in PICO-60 WIMP search data, where the reconstructed vertical position Z is plotted against the normalized distance from the center axis squared. The dashed line represents the fiducial cut. Single bulk bubbles passing all cuts are shown as red squares and rejected single-bubble events are shown as grey dots. Figure from Amole et al. (2017).

accounts for the remaining source of background, which includes neutrons and alpha particles. Neutrons can scatter off nuclei and mimic dark matter signals (Behnke et al., 2014), but this background is typically reduced with shielding. However, in the case of alpha decays at MeV-scale energies, it is necessary to implement a type of calorimetry technique to reject them (Aubin et al., 2008). With the careful selection of operating temperature and pressure, detectors using superheated liquids can become 'blind' to electron recoils (background) from remaining scatters produced from beta, gamma, and neutrino radiation. Further information can be found in the references cited below regarding this technique.

Superheated detectors offer excellent background rejection since the threshold can be set to optimize gamma and electron insensitivity, gammas and electrons being the most problematic backgrounds in dark matter searches. This background rejection advantage arises primarily from the relatively long distances over which energy is deposited in an electron recoil and the low probability of having sufficient energy deposited within the critical radius. The measured rates of electron recoils in multiple PICO calibration chambers are shown in Figure 1.15, which highlights a rejection of 10^{-10} as the normal operating threshold for the PICO-60 detector. This is the best electron recoil rejection factor ($< 10^{-10}$) in the field that has been measured in superheated liquid-filled detectors in conditions leading to high sensitivity to few-keV nuclear recoils (E. Behnke et al., 2008, 2013; S. Archambault et al., 2009). In comparison, this discrimination is seven orders of magnitude weaker for liquid-xenon (LXe) detectors. More specifically, this is an intrinsic rejection, characterized by a complete absence of bubble nucleations, which means that it is independent of background cuts performed in the analysis. Bubbles produced in chemically stable fluids can only arise from nuclear recoils or alpha particles (Bolte et al., 2007).

Visual signatures allow partial discrimination of nuclear recoil backgrounds since neutron multiple-scatter events within the active volume produce separated bubbles (see Figure 1.16). The emission of alphas as the primary background is atypical for dark matter detectors.

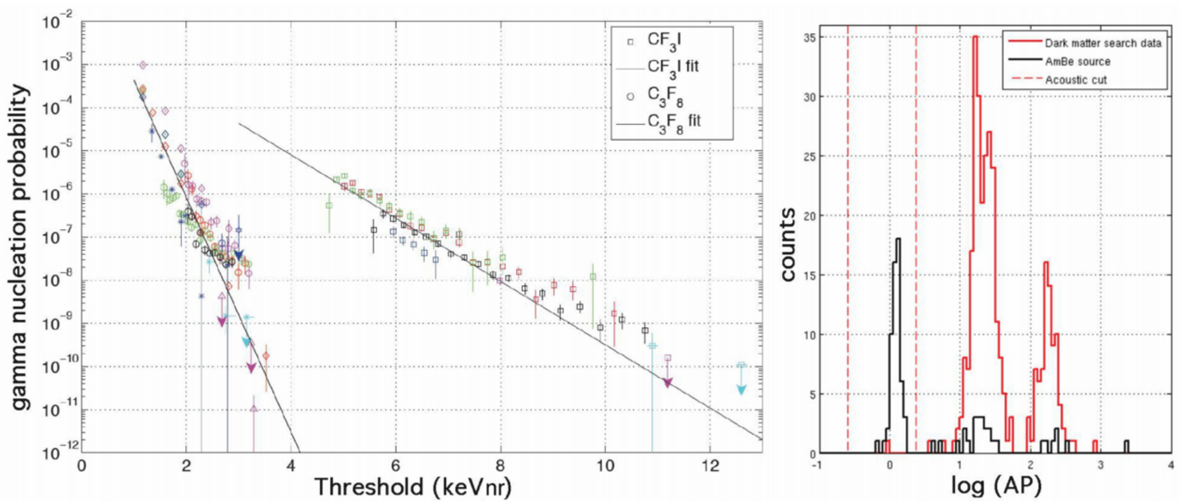

Figure 1.17: Left: measured intrinsic discrimination against gamma-induced electron recoils, plotted against threshold energy for nuclear recoils. Right: acoustic alpha discrimination achieved during the second run of PICO-2L at SNOLAB. Single bubbles from neutron-induced nuclear recoils (AmBe source) are normalized to an acoustic parameter $AP = 1$. This acoustic parameter is proportional to the intensity of sound emission pertaining to bubble nucleations (Behnke et al., 2011). The red histogram represents the events collected during dark-matter search runs. These events originate in alpha emissions from ^{222}Rn and its short-lived daughters, which are characterized by a large AP. Advances in acoustic discrimination have led to reliable acoustic alpha calorimetry, as showcased by the double peak in the red histogram (see Figure 1.21). The few naturally occurring events from alpha emissions produced during neutron source calibrations are visible in the AmBe histogram.

These alphas are emitted by radioactive contamination within the target and have total bubble nucleation efficiency when the energy-dependent threshold is surpassed. However, the acoustic energy released in the bubble's expansion can be measured to discriminate between alphas and the expected WIMP signal (nuclear-recoil) since alpha particles are known to be louder (see Figure 1.17).

Bubble chamber scalability is of relatively minor concern since built-in amplification provided by the rupture of metastability and the stemming macroscopic phase transition allow the collaboration to monitor large target masses easily. This technique benefits from the choice of three event triggers, which can, in principle, monitor arbitrarily large chambers using a single readout channel: pressure rise from boiling within a closed volume, intense

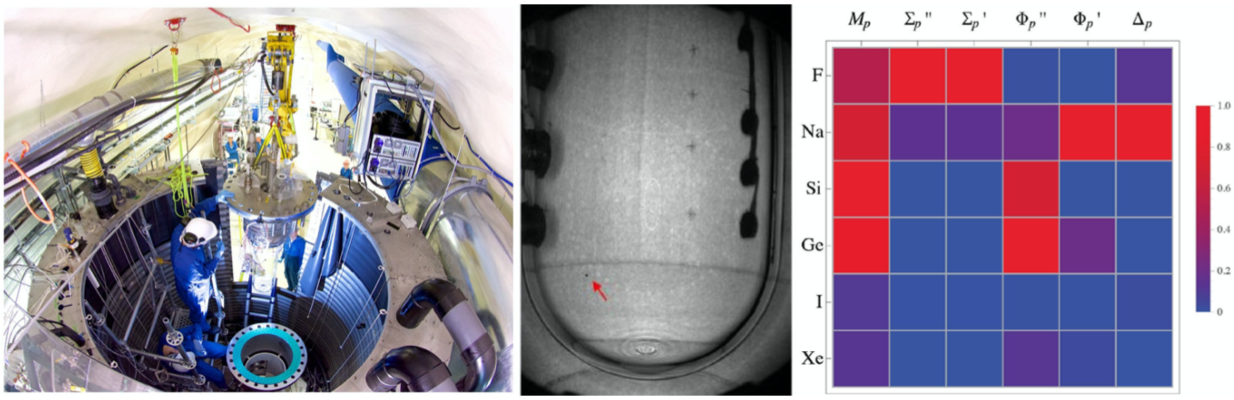

Figure 1.18: Left: recent PICO-60 upgrade at SNOLAB showing the insertion of the inner quartz vessel. Visible items include a water tank providing thermal control, neutron shielding, and Cerenkov muon vetoing. Center: first bubble detected by PICO-60 at SNOLAB, shown in one of two stereoscopic images. Right: response comparison of several target materials to six possible WIMP-proton couplings shown as a figure of merit proportional to interaction strength. Fluorine on the top left corner is seen to dominate for several of them, complementing germanium and xenon, favored for neutron couplings (Fitzpatrick et al., 2012).

acoustic emission describing the initial stage of nucleation, and visual bubble detection. The most effective of these are optical detection, which is implemented by real-time comparison of video frames recorded every ~ 10 ms, capturing the early stages of bubble development and triggering chamber recompression before the bubble grows much larger than a few mm. The installation of multiple cameras allows a refined spatial position reconstruction of $\sim 1\ \mathrm{mm}^3$. The WIMP interaction signature comes from a single bubble induced by the high stopping power nuclear recoil. In large chambers, neutrons are likely to produce multiple bubbles and have free paths between scatters of just a few cm. However, PICO's use of stereoscopic, high-resolution imaging of events (see Figure 1.18) allows for an emphatic rejection mechanism for this otherwise irreducible neutron background bound, which eventually affects all direct detection experiments.

Improving sensitivity to both spin-dependent and spin-independent WIMP couplings provides a more efficient probing of supersymmetric WIMP parameter space. Some regions favor one mode of interaction over the other (see Figure 1.19, left panel), emphasizing the

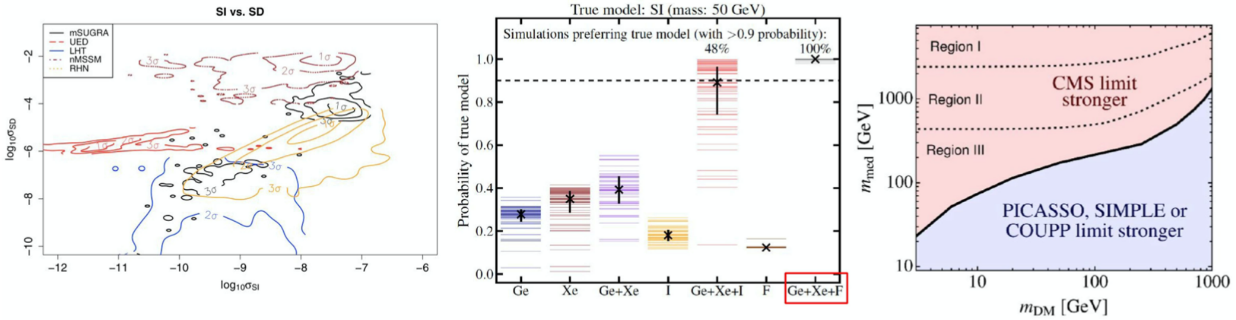

Figure 1.19: Left: comparison of SD-proton vs. SI cross sections for a set of dark matter models, highlighting their complementarity: the lack of obvious correlation between these couplings underscores the need for detectors maximally sensitive to the SD channel (Bertone et al., 2007; Barger et al., 2008). Center: the addition of a fluorine-rich target to Ge and LXe is able to pinpoint the correct underlying model of dark matter interaction, in a majority of simulated experiments. Figure from Gluscevic et al. (2015) reproduced with permission. Right: the assumptions made in the effective field theories employed to extract accelerator constraints on SD dark matter couplings (see Figure 1.23) strongly influence their validity. Here m_{med} denotes the interaction mediator's mass and m_{DM} the mass of the dark matter particle. Figure from Buchmueller, Dolan, and McCabe (2014) reproduced with permission.

importance of the SD channel for a variety of reasons (J. I. Collar et al., 2000; D. S. Akerib et al., 2006). However, from a pragmatic point of view, the most potentially interesting is that some supersymmetric models can generate much smaller WIMP cross-sections for the SI channel (see Figure 1.19). Hence, a complete exploration of SUSY dark matter is less likely via this coupling alone, even after accounting for the coherent enhancement to the SI cross-section. PICO chambers have used multiple safe refrigerants operable near room temperature (e.g., CF_3 I, C_3F_8, C_4F_{10}, CF_3Br), which are maximally sensitive to spin-dependent coupling through their large fluorine mass fraction (Ellis and Flores, 1991).

The progress of searches sensitive to SI WIMP-nucleus couplings is a subject of great interest partly due to historical inertia. Experimental efforts have focused heavily on this interaction mode to benefit from the coherent enhancement to the SI cross-section. However, there is no theoretical bias favoring this coupling. Recent phenomenological emphasis (Fitzpatrick et al., 2013; Anand et al., 2015; Gresham and Zurek, 2014; Gluscevic et al., 2015) tells a different story: there are many WIMP interaction mechanisms, and a variety of targets not

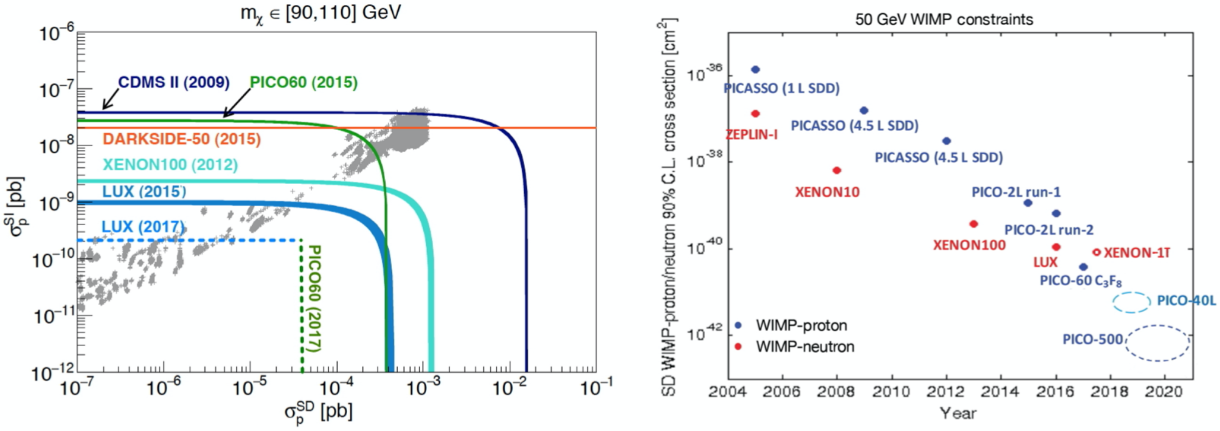

Figure 1.20: Left: WIMP scattering cross-sections excluded via SD and SI channels. Right: SD-proton coupling sensitivity as a function of publication date for LXe and superheated detectors, where the XENON-1T datapoint is inferred from the its first SI limits. It is worth noting the differences in the rate of progress made evident in this representation.

restricted to those leading in SI reach are required to investigate them thoroughly. A close inspection of Figure 1.20 shows that PICO targets already compete with or dominate over LXe detector sensitivity to multiple of these viable WIMP couplings (Gresham and Zurek, 2014), bearing in mind that the current PICO limits are a factor of > 300 lower than what is considered there (Amole et al., 2017).

In a similar vein, a recent publication compared the efficiency of different dark matter searches in probing supersymmetric models via SD or SI couplings (Riffard et al., 2016). The left panel in Figure 1.20 shows an updated version of the main result, indicating that PICO is rapidly approaching large LXe detectors in the coverage of its supersymmetric candidates. Moreover, the right panel in Figure 1.20 confirms that PICO is advancing in WIMP sensitivity at a noticeably faster rate than LXe detectors. Lastly, the need for fluorine-based sensors, in addition to Ge and LXe targets, has been recently emphasized. Hence, combining these targets will be necessary to thoroughly understand the interaction mediating an eventual WIMP detection (Gluscevic et al., 2015).

Construction costs for room-temperature bubble chambers rank low (a few thousand USD/kg target mass for > 100kg modules, all-inclusive). This is a notable advantage given

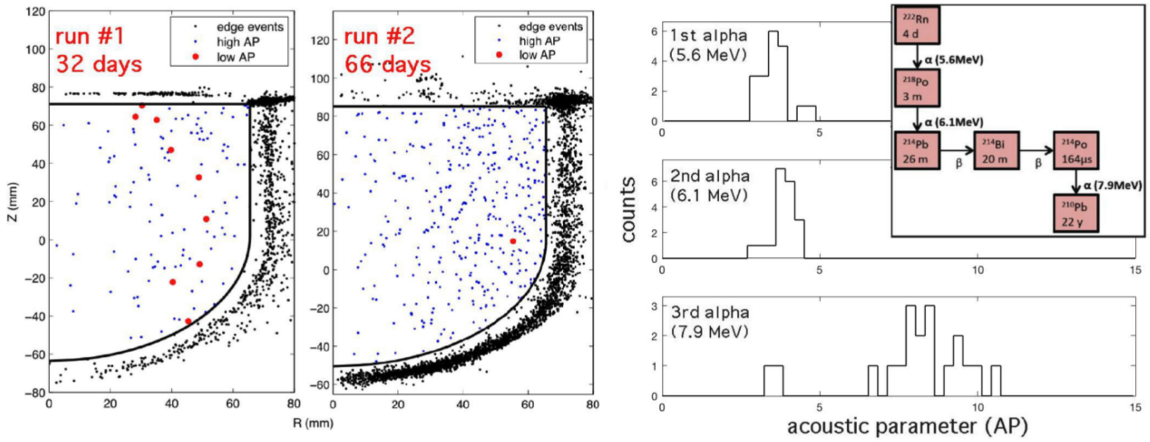

Figure 1.21: PICO-60 progress achieved during experimentation at SNOLAB. Left: a second PICO-2L run only limited by the expected neutron-interaction rate (Amole et al., 2016) thanks to the successful removal of particulates in solution. The vertical cross-section of the active volume is shown with the single surviving WIMP-like event is shown in red, alpha events in blue, and surface or interface events in black. A blind analysis using PICO-60 of a 1,167-kg day final exposure revealed no WIMP candidates (Amole et al., 2017). Right: measurement of acoustic yield proportional to alpha energy, independently tagged via temporal analysis of identifiable ^{222}Rn alpha triplets (inset).

the large masses needed for full LSP exploration. Moreover, room-temperature operation features such as safety (non-toxic industrial refrigerant targets) and moderate pressures ($<$ 200 psig) add to the appeal of this design. PICO concerns about the radiopurity of chamber materials and shielding are also mitigated thanks to the intrinsic insensitivity to gammas, leading to freedom of design, reduction of costs, and expedited chamber construction. Details of the work that goes into preparing radiopure piezoelectric transducers for PICO can be found in Appendix C of Fustin (2012). Notwithstanding, control of alpha-emitters within the active volume of PICO chambers remains essential, given that alphas can produce single-bubble nucleations similar to those produced from nuclear recoils.

The PICO collaboration has recently demonstrated excellent discrimination between alpha and nuclear recoils using acoustic methods (Amole et al., 2017) (see Figure 1.17). The significant difference in microscopic trajectory range between these two types of particles defines the size or quantity of the rapidly expanding protobubble(s) responsible for acoustic

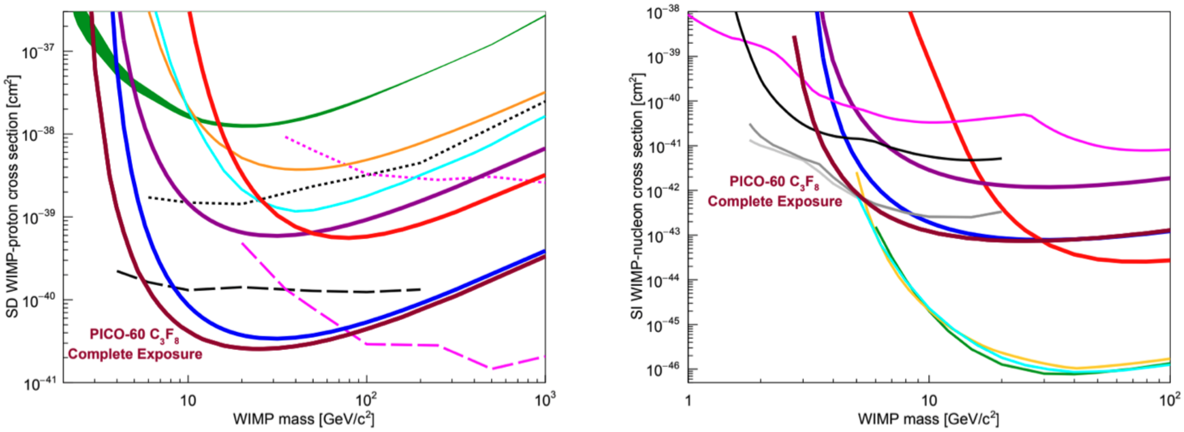

Figure 1.22: Left: PICO-60 C_3F_8 SD WIMP-proton cross section limits at 90% C.L., along with the first run of PICO-60 C_3F_8 shown in dark blue (Amole et al. 2017), PICO-60 CF_3I in red (Amole et al. 2016), PICO-2L in purple (Amole et al., 2016), and PICASSO in green (Behnke et al., 2017). Right: PICO-60 C_3F_8 SI WIMP-proton cross section limits at 90% C.L. Further details can be found in Amole et al. (2019).

emission. This additional capability is expected to allow PICO to achieve its ultimate sensitivity goals. Successful acoustic discrimination has relaxed by several orders of magnitude the original target of reaching alpha-emitter concentrations of $< 10^{-17} g/g$ within the active volume. Specifically, 0.2 alphas were observed per kg-day in PICO-60. The possibility of (α, X) reactions shortening the alpha trajectory length and hence reducing its acoustic yield is expected to limit alpha acoustic rejection to 10^{-5} (Robinson, 2015). These two figures suggest that a large chamber (a few hundred liters) will eventually run into an alpha-background limitation after a few years of operation.

1.3.3 Present Status and Future

PICO and its precursors PICASSO and COUPP have a long history of world-leading dark matter searches. PICO was formed by merging the PICASSO and COUPP collaborations, which employed room-temperature superheated liquids to search for dark matter particle candidates. The collaboration has operated two bubble chambers at SNOLAB, PICO-60, and PICO-2L, filled with up to 60 kg of a superheated target. These devices have played a crucial

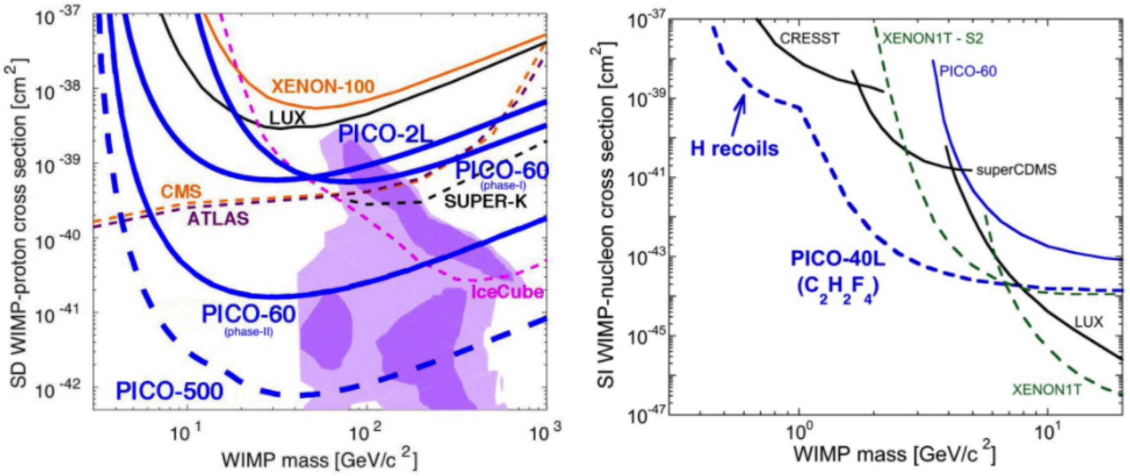

Figure 1.23: SD and SI sentivities obtained from the two previously-operated bubble chambers at SNOLAB, PICO-60 (Amole et al., 2016, 2017) and PICO-2L (Amole et al., 2016). These chambers provided the first direct exploration of favored SD supersymmetric dark matter phase space shown as purple solid regions (Roszkowski, Riuz de Austri and Trotta, 2017). Projected sensitivity for PICO-500 and PICO-40L are shown as thick dash blue lines. A background-free run using PICO-40L at a threshold of 1.5 keVnr is expected to provide an extention to low-mass WIMPs. A similar eventual extension to lower WIMP masses is expected from PICO-500. Whereas PICO-500 will provide an extensive exploration of supersymmetric WIMP candidates via SD couplings.

role in informing next-generation chamber design while continuously improving bound on spin-dependent WIMP interactions. PICO-60 is presently the most advanced bubble chamber for dark matter searches (Amole et al., 2019) (Figure 1.25). The final exposure collected during the second PICO-60 run resulted in an additional improvement in sensitivity by a factor of 17, and the best standing limits on SD WIMP couplings (Amole et al., 2017), shown in Figure 1.22. Lastly, a final run at a higher degree of superheat (i.e., lowering the threshold from 3.3 to 1.75 keVnr) further improved the sensitivity to low WIMP mass beyond what is shown in Figure. 1.23.

The smaller PICO-2L was used mainly for research and development on the alternative fluid C_3F_8 to inform its use in the final runs of PICO-60. Some of the key reasons to consider C_3F_8 as a replacement for CF_3I were to the following: i): its higher content in fluorine per mass results in enhanced sensitivity to both SD couplings and low-mass WIMPs

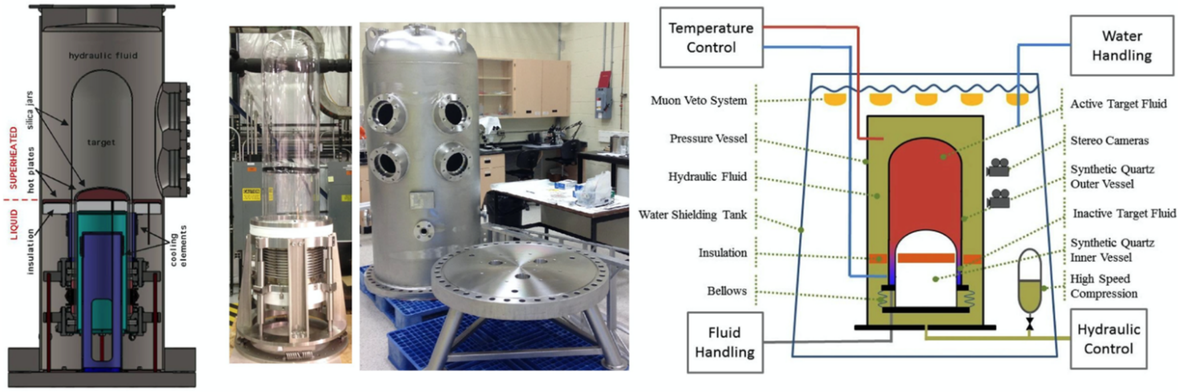

Figure 1.24: Present and future generation PICO chambers. From left to right: PICO-40L schematic, its inner and outer vessel during assembly at SNOLAB, and a RSU system schematic, common to both PICO-40L and PICO-500.

(see Figure 1.23), ii): the achievable nuclear recoil threshold is considerably lower than for CF_3I (see Figure 1.17, left panel) for a given electron recoil rejection factor. The reason for this is because of the K-shell electron binding energy in iodine, which is much larger than for fluorine, where gamma-sensitivity is mediated by Auger electron emission (Tenner, 1963), iii): A much sharper sensitivity onset to low-energy fluorine recoils in C_3F_8 has been confirmed by conducting a variety of low-energy neutron calibrations, compared to that of CF_3I (Amole et al., 2015; Robinson, 2015). The result was a considerable improvement in C_3F_8 sensitivity to WIMP masses below tens of GeV.

The same basic design is used to inform the design of all PICO chambers. Contained within a synthetic fused silica jar is a target fluid (C_3F_8, CF_3I or $C_2H_2F_4$) used for operation. This component is connected to flexible stainless steel bellows separated from the active region by a silica piston in the current designs. In contrast, in older chambers, this was an ultrapure water buffer layer. The detector is contained within a pressure vessel filled with hydraulic fluid (typically propylene glycol or mineral oil). The hydraulics are managed externally, expanding for superheated operations and later compressing the system upon triggering. The use of cameras at stereo angles allows for the position reconstruction of bubbles. Acoustic signals are picked up with custom-made zirconate titanate (PZT) piezoelectric

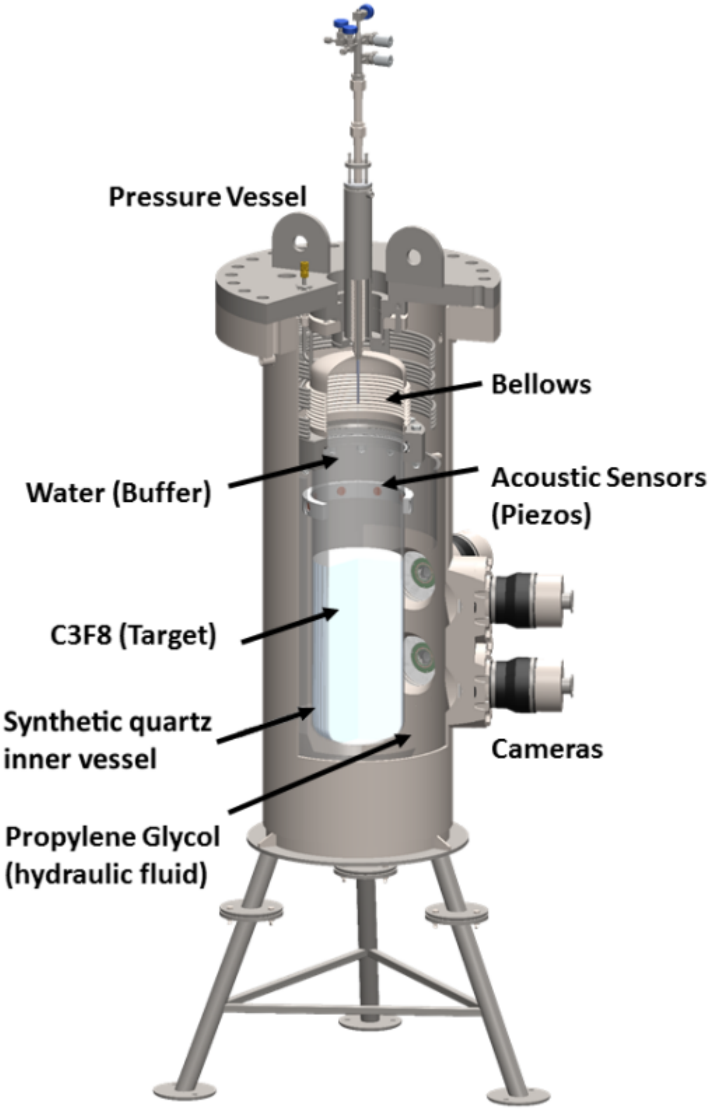

Figure 1.25: Configuration of the PICO-60 detector for its operation with C_3F_8. Two columns of two cameras can be seen on the right. They are used to stereoscopically image the full volume of target fluid. Figure from Amole et al. (2019).

sensors externally attached to the vessel. Figure 1.24 showcases the implementation of this design in PICO-40L, the present-generation PICO detector.

PICO-500 is the next-generation detector. It will be filled with 500 L of C_3F_8, increasing the scale of the right-side-up chamber design, with the goal of swift conversions to low-mass sensitivity for purposes of confirming PICO-40L discoveries using a hydrogenated target. The identification of hydrogen recoils in new targets and improvements in background rejection at high degrees of superheat aim to extend the reach of PICO-500 to WIMP masses below 1 GeV/c^2. It is worth noting that concentrating collaboration efforts on C_3F_8 is also strategic. Given the advanced state of the XENON-1T and -nT projects, PICO can be more valuable to the field of direct dark matter searches through its superior sensitivity to SD WIMP-proton couplings and low-mass WIMPs (see Figure 1.23). As discussed in the previous section, the pursuit of maximum SD sensitivity improves the chance of WIMP discovery, complementary to SI searches. PICO-500 is expected to begin a spin-dependent WIMP search in 2021 and reach cross-sections down to $\approx 10^{-42}$ cm^2. There are small-scale bubble chambers within the collaboration used for studying calibration results and technological advances. More recently, two of these chambers were deployed to test proposed next-generation design upgrades and verify the performance of the hydrogen-rich scattering target. They are the GUNTER and Drexel Chamber located at the University of Chicago and Drexel University, respectively. The following chapter will emphasize the motivation to build GUNTER and describe the studies of interest that make up the rest of this thesis.

CHAPTER 2

GUNTER CHAMBER

GUNTER (see Figure 2.1) is a “right-side-up” chamber designed and assembled at the University of Chicago for high-statistics calibration work within its 25 c.c. active volume. This style of chamber is a departure from earlier designs where a buffer inert (i.e., not superheated) liquid would float atop the active volume, contacting all rough, porous metallic surfaces that would otherwise be prone to surface nucleations (a process typically referred to as “pool boiling”). “Right-side up” chambers do without this buffer fluid and instead rely on a sharp gradient of temperature to keep all such metallic surfaces surrounded by target fluid always in the liquid phase. A warmer volume sits atop, containing the superheated target, which wets only the smooth surfaces of quartz vessels.

GUNTER monitors up to 25 MHz acoustic emissions using a high bandwidth piezoelectric transducer amplifier and high-speed (1 GS/s) digitizer. Acoustic emissions at these high frequencies are of interest since they correspond to the very early stages of evolution in an expanding bubble when its size is of the order of tens of microns or smaller (the instantaneous dominant wavelength of acoustic emission is of the order of the bubble diameter) (Levi et al., 1978). The differences between different types of radiations in their acoustic signature are expected to be maximal during the early stages of bubble evolution when the length scale is comparable to particle range —tens of microns for alphas. GUNTER is the first chamber within the PICO collaboration to expand its sensitivity range beyond acoustic frequencies of $\sim$ 300 kHz, exploring new opportunities for acoustic particle discrimination in the process.

Images of sub-millimeter bubbles are captured with sensitive entropy triggers implemented using stereoscopic 200 fps cameras. Spatial reconstruction of captured events is achieved via a neural network algorithm that determines bubble positions with O(1) mm accuracy. The chamber features a fast Dytran pressure transducer which provides additional information on bubble multiplicity and position. Robust hardware integration software pro-

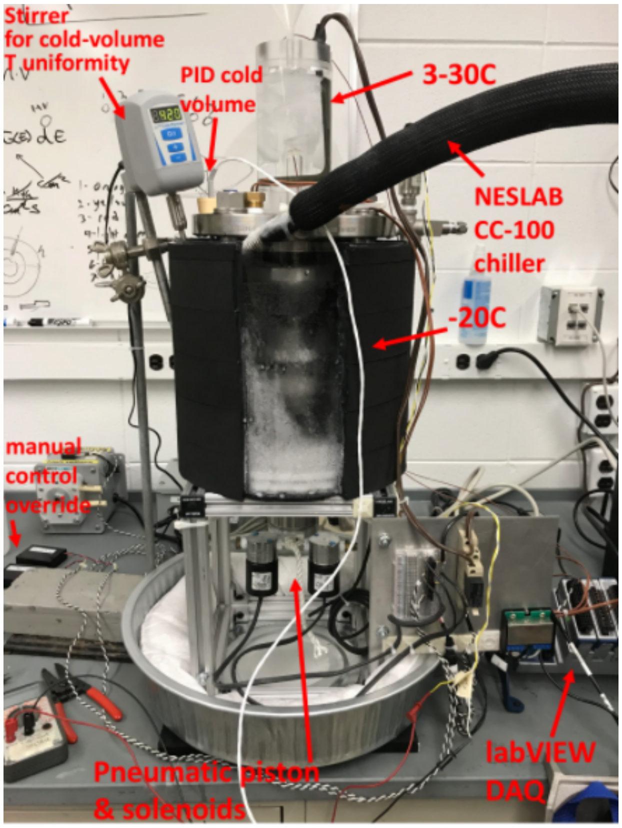

Figure 2.1: Snapshot of GUNTER calibration chamber during C_3F_8 operation with labeled components and details of operation. Further information about the design of GUNTER is included in Appendix B.

vides DAQ, control, and analysis for GUNTER. The chamber's pressure and PID-controlled temperature stability are of order O(1) psig and O(0.25) C, respectively. GUNTER was deployed for C_3F_8 and R-134a nuclear and electron recoil calibrations and as a testbed for acoustic sensor design. Cross-section and top view diagrams of GUNTER are shown in Figures 2.2 and 2.3, respectively. The transverse cut view includes the ^{88}Y/Be source geometry to highlight its complexity as described in simulations where other sources were considered point sources.

2.1 Motivation

2.1.1 New Model for Electron Recoil Response

The PICO collaboration developed a new semi-empirical model of electron recoil nucleation, outlined in a recent publication (Amol et al., 2019). According to this model, electron recoils produce bubbles through dispersed ionization from delta-electrons rather than through nucleation processes due to localized heat spikes as in the previously discussed Seitz model, which is a strong approximation for describing nuclear recoils (Behnke et al., 2013). In this newly defined scenario, the energy threshold becomes

$$E_{ion} \approx 4\pi r_c^2 \left(\sigma_{surf} - T \frac{\partial \sigma_{surf}}{\partial T} \right) + \frac{4\pi}{3} r_c^3 P_l, \tag{2.1}$$

where E_{ion} is referred to as the ionization energy threshold and P_l is the liquid pressure. A detailed derivation of the ionization energy threshold can be found in Appendix B of Amole et al. (2019). This threshold E_{ion} represents the total surface energy of the bubble plus the work done by the expanding liquid reservoir.

This thesis describes how GUNTER calibration data was used to demonstrate this new model of bubble-nucleation by electron-recoils in C_3F_8 (see Section 3.1) and R-134a (see Section 4.3), casting light on the underlying physical mechanisms at work. Additionally, it

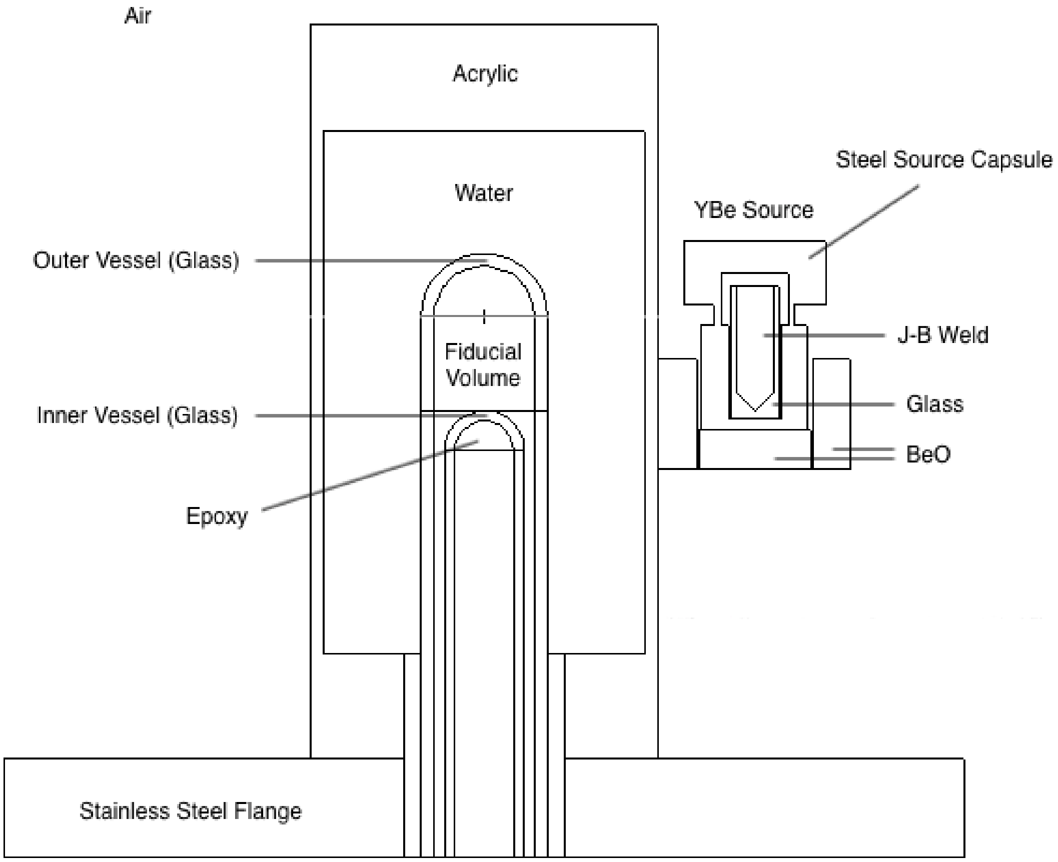

Figure 2.2: Schematic cross-section view of GUNTER and ^{88}Y/Be source with labelled materials as defined in MCNP simulation.

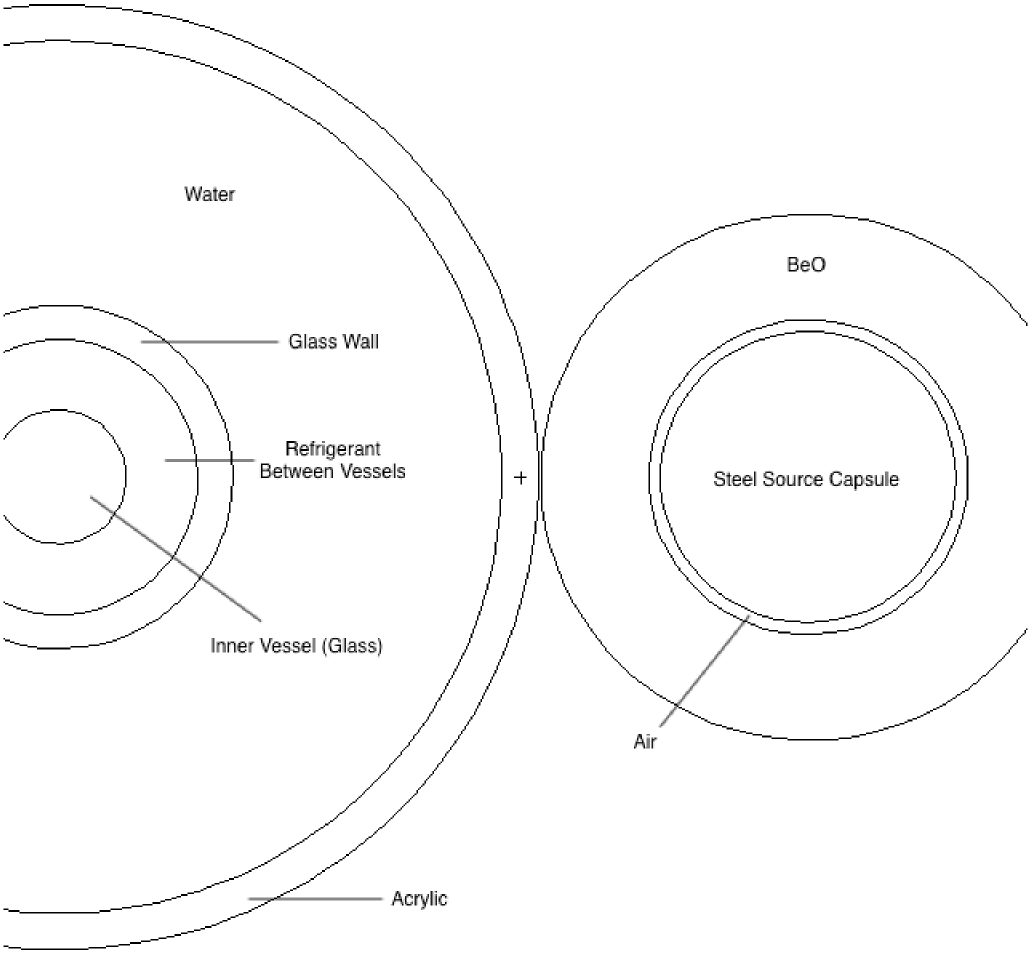

Figure 2.3: Schematic top view of GUNTER and ^{88}Y/Be source with labelled materials as defined in MCNP simulation.

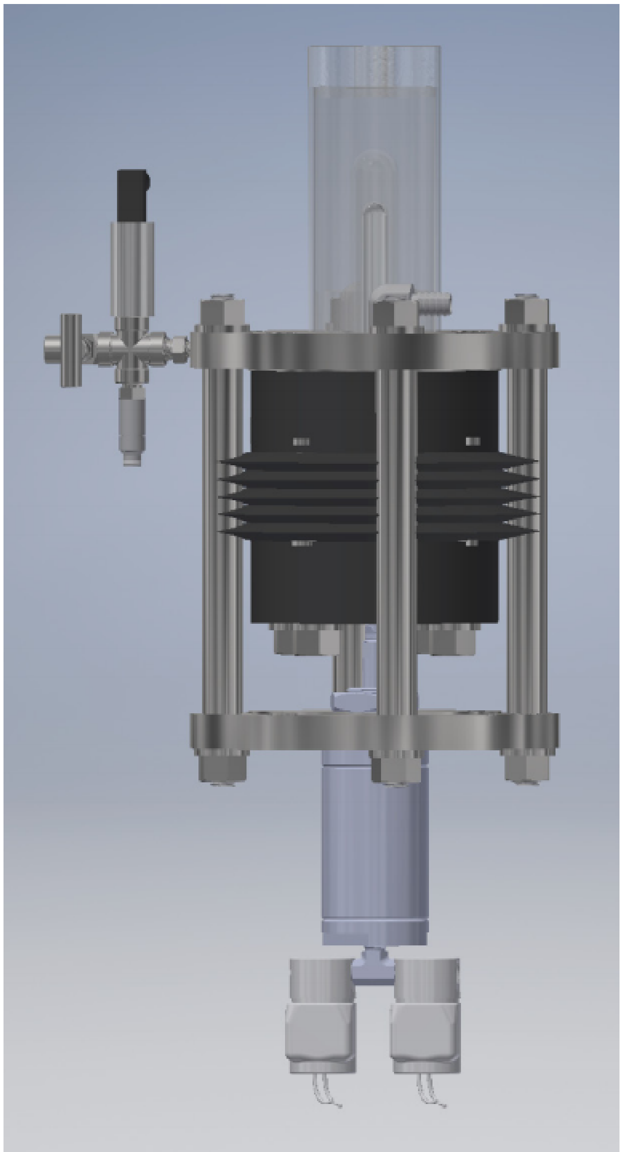

Figure 2.4: CAD rendering of fully assembled GUNTER while compressed. Figure courtesy P. Jordan (private communication).

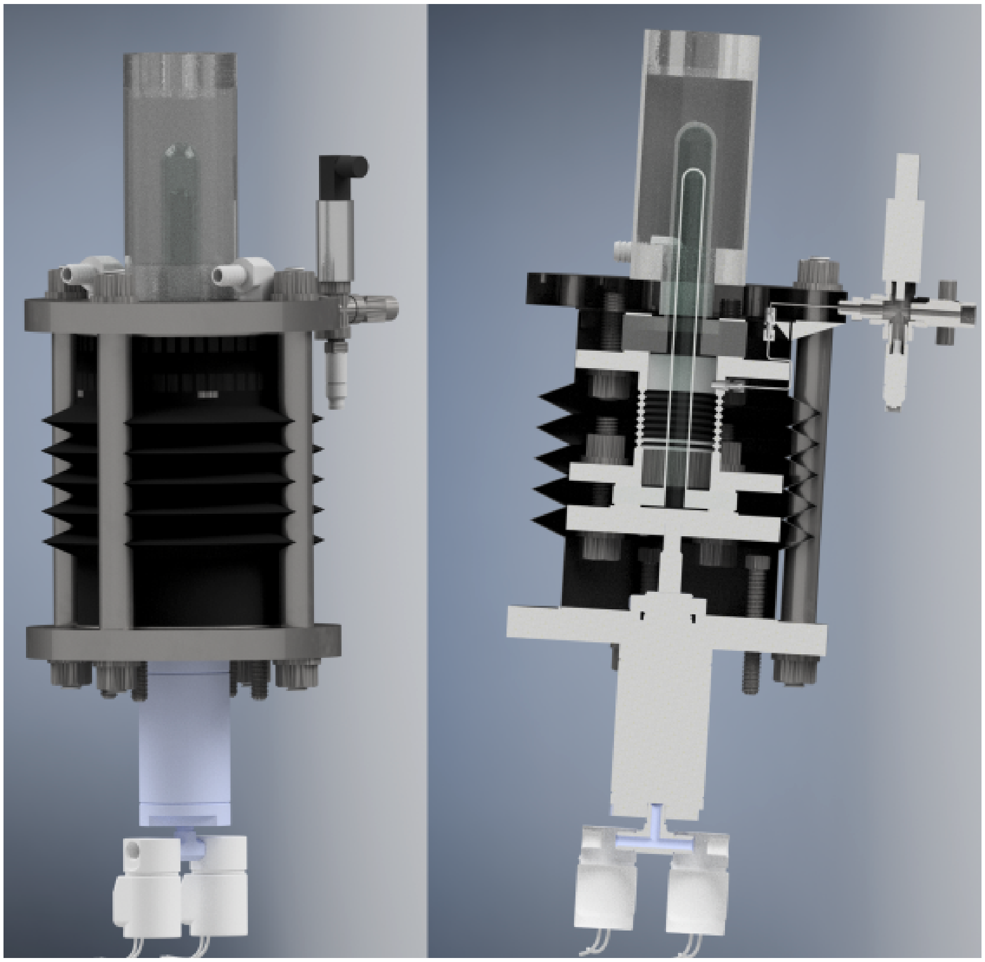

Figure 2.5: CAD rendering of GUNTER cross-section while expanded. Figure courtesy P. Jordan (private communication).

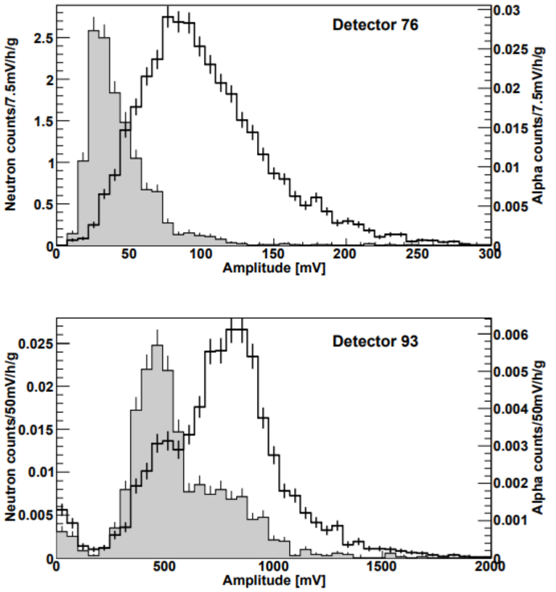

Figure 2.6: Amplitude distribution for neutron and alpha particle induced events, where the PICASSO experiment observed alpha particles generating significantly 'louder' emissions. Figure from Aubin et al. (2008).

examines the main implications of this result: electron recoil nucleation probability scales differently from that of nuclear recoils with operating pressure and temperature. Hence, the careful selection of operation parameters can maximize the ratio of nuclear recoil signals accepted over electron recoil backgrounds. This is achieved in practice by running at the lowest operating temperature for a given nuclear threshold. However, the current chamber design for PICO-40L is limited to pressures above atmospheric. PICO aims to develop a sub-atmospheric pressure system and improve thermal control to exploit this newly demonstrated model in future experiments with this conceptual design work in mind.

2.1.2 Acoustic Studies

The acoustic distinction of alpha particles from nuclear recoil events is one of the critical classification efforts within the PICO collaboration. This endeavor relies on a discovery by the PICASSO experiment (Aubin et al. 2008), which showed that alpha particles generate significantly louder emissions (see Figure 2.6). A way of understanding the underlying physics

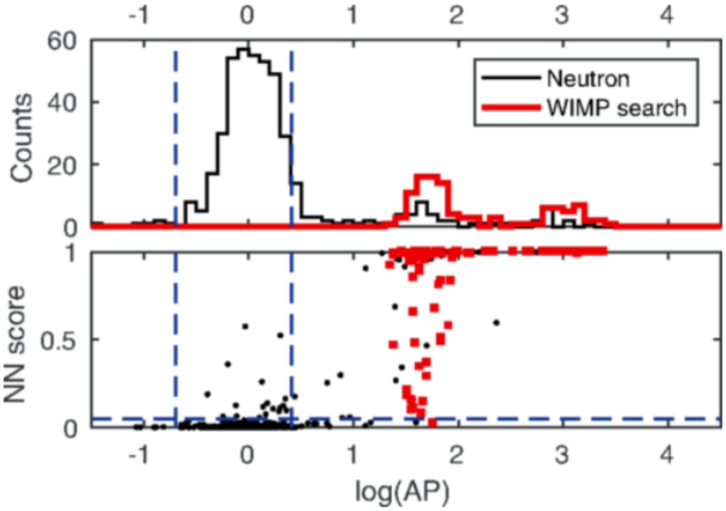

Figure 2.7: Acoustic analysis variables for WIMP search data and neutron calibration runs. The top plot shows the standard acoustic parameter (AP) and the bottom plot shows the same but with the addition of a neural net output score. Figure from Amole et al. (2017).

behind this observation is to consider that in alpha events, there is both scattering and stopping alpha particles and the recoil of the nucleus whence the radiation was emitted. From this phenomenon, at least two ionization tracks or proto-bubbles are produced, and this information lives on acoustically via the production of the single macroscopic bubble. The pressure waves emitted as bubbles expand during the kinematic growth phase create the acoustic waves that propagate through the target medium and the silica vessel and are detected by the piezoelectric sensors. Maximum acoustic sensitivity for standard PICO sensors ranges from 1–300 kHz.

Standard acoustic analysis typically consists of extracting variables connected to the measured acoustic energy across different frequency bands and the reconstructed 3D position and using this information to build simple neural networks. An example of acoustic parameter distribution for a standard WIMP-search run is shown in Figure 2.7. The collaboration has demonstrated that the energy of alphas can be inferred through acoustic observations. Additionally, efforts within the PICO collaboration have explored the possibility of acoustic electron recoil rejection. The use of deep neural networks to distinguish gamma particles

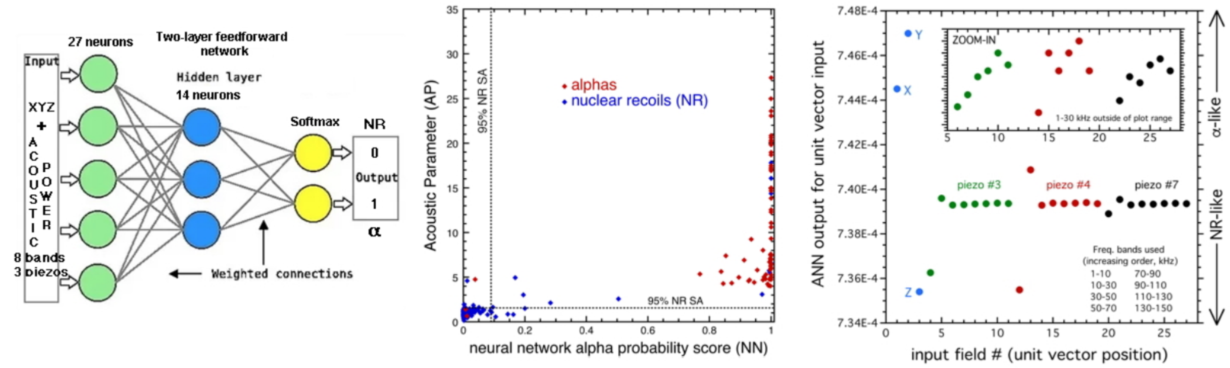

Figure 2.8: Left: architecture of the ANN employed by the University of Chicago group for alpha and nuclear recoil discrimination in PICO-60 (Amole et al. 2017). Center: comparison of AP and ANN performance for the training of sets used in Amole et al. (2017). ANNs are deemed ideal for a future expansion of particle identification in PICO since they exploit all available acoustic information. Right: it is possible to recognize the patterns identified by the network by feeding unit vectors into the ANN input and observing the generated output. Subtle frequency dependencies able to distinguish alphas from nuclear recoils, similar for all transducers, can be noticed in the inset. An unaided human observer is unable to spot these patterns.

from both alpha and neutron events is shown in Figure 2.8. However, the final results have been limited due primarily to the poor performance of PICO-60 acoustics and the scarcity of calibration data. PICO aims to further its approach to acoustic analysis by using additional information extracted with improved sensors as high and lower frequencies become available (see Figure 2.9). Hence, GUNTER calibration studies aimed to inform acoustic sensor design and explore further indications of acoustic discrimination between electron and nuclear recoils using neural networks.

The rapid loss of intrinsic electron recoil rejection with increasing degree of superheat (i.e., decreasing nuclear recoil detection threshold) (see left panel of Figure 1.15) emphasizes the need to distinguish between electron and nuclear recoils through acoustic means. This rejection loss limits the sensitivity to low-mass WIMPs presently reachable. The recently published PICO-60 runs at thresholds as low as 1.2 keV showed an observed background in good agreement with the environmental gamma flux at the detector (Amole et al. 2019) and the loss of intrinsic ER rejection visible in Figure 1.15. Improvements in acoustic analysis, limited to a modest 99.5% electron recoil rejection efficiency, are expected to provide the slight recovery of discrimination against electron recoils needed to generate the leading low-mass WIMP sensitivity shown in the right panel of Figure 1.23. The environmental gamma flux of PICO-500 is expected to be two orders of magnitude lower than for PICO-60 since a much larger water shield will be used, and a higher degree of superheat will lead to a much stronger acoustic yield. Again, it is worth emphasizing that a reduction in the Seitz threshold leads to larger acoustic emissions. This is the equivalent to saying that the speed of bubble expansion increases the further away the target is from thermodynamic equilibrium. The advantage of observing larger, clearer signals at lower detection thresholds arguably places PICO in a unique position in the field of dark matter searches.

2.1.3 PICO-LowMass

PICO-40L will cease operations when both its final sensitivity reach to SD dark matter is exhausted, and PICO-500 operations begin. Shortly after that, PICO-40L will be re-optimized as a dedicated low-mass dark matter detector: PICO-LM. PICO-LM will extend low-mass dark matter sensitivity using hydrogen-rich compounds such as R-134a. Hydrogen is the most sensitive target for low-mass nuclear recoils since it maximizes kinetic sensitivity. The newly developed electron recoil response model will allow fine-tuning the operating threshold to low masses while also achieving maximum electron recoil suppression. Additional external gamma shielding will be used for direct rejection of electron recoils, which will lower the Carbon-14 content of the target and further improve the purity of materials. Initial nuclear recoil calibrations for R-134a at the Universite de Montreal and the University of Chicago (GUNTER) shown in Figures 2.10 and 2.11, respectively, have demonstrated stable operations at thresholds down to below 2.5 keV, and electron recoil rejection comparable to C_3F_8.

Projected sensitivities for eventual electron recoil background rejection for PICO-LM are

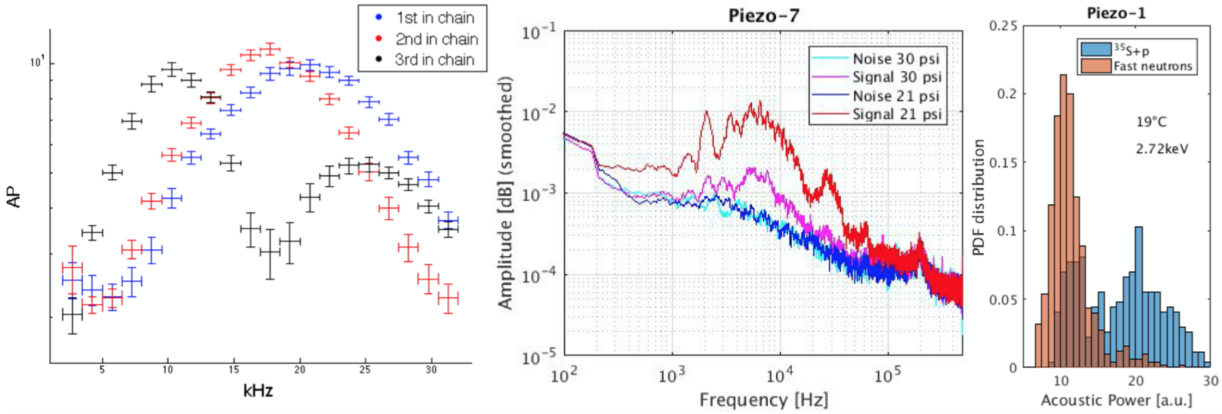

Figure 2.9: Left: AP parameter expression of the power spectrum in the few kHz frequency range, for the three alpha energies emitted by ^{222}Rn. The average value for all alphas identified during the first phase of PICO-60 are shown. PICO aims to exploit this abundance of spectral information for particle identification. Center: present limited range of frequencies available to PICO piezoelectric transducers as a result of inefficiencies in ceramic geometry. Acoustic information from stages of bubble development prior to a few hundred microns falls outside of their reach. Particle identification is expected to be maximal toward higher frequencies. Visible in the plot is the rapid increase in acoustic signal with decreasing energy threshold for nuclear recoil detection, where the drop in operating pressure shown reduces this acoustic threshold by a mere 0.5 keVnr. Right: preliminary evidence for acoustic identification of proton recoils in C_2CIF_5, induced via $^{35}Cl(n_{th},p)^{35}$. As expected, the long range of these monochromatic 600 keV proton recoils were observed to generate a higher acoustic yield than for carbon, chlorine, and fluorine recoils induced via elastic scattering of fast neutrons. PICO plans to investigate these differences at much lower proton energies in $C_2H_2F_4$ (refrigerant R-134a), using existing data from calibration chambers such as GUNTER.

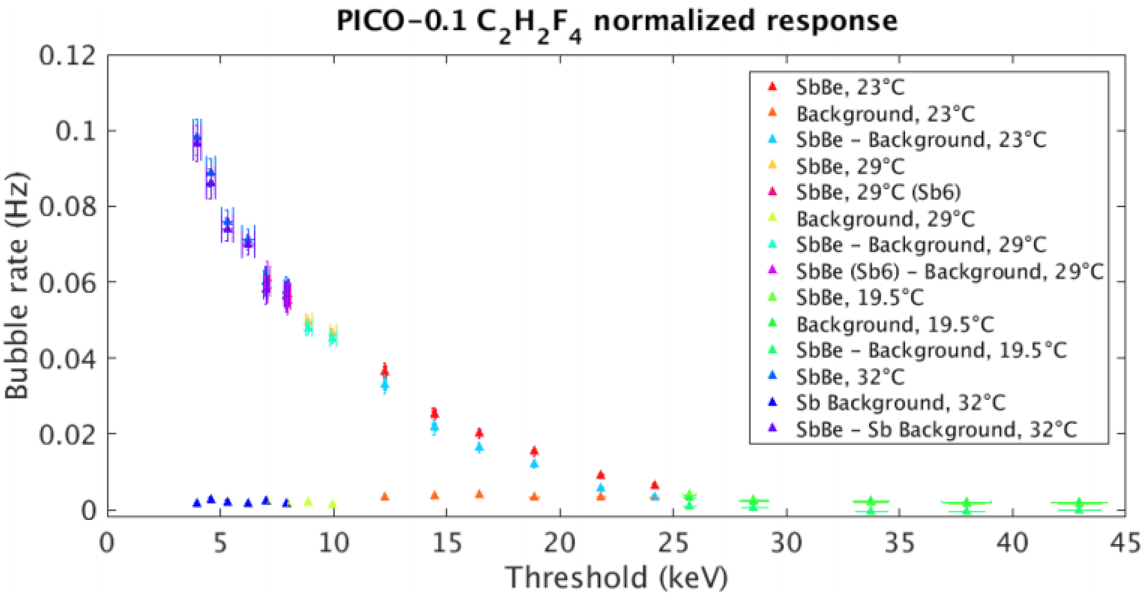

Figure 2.10: Preliminary calibrations at Universite de Montreal of R-134a response to low-energy neutrons generated by photonuclear reactions. This technique is described in great detail in Collar (2013). GUNTER was used for similar preliminary studies that indicated a good efficiency for bubble nucleation by few-keV proton recoils in R-134a.

shown in Figure 2.12. The projected sensitivity extends below dark matter masses of 200 MeV and is close to 10^{-40} in spin-dependent cross sections for dark matter masses below 1 GeV, far exceeding current detection bounds. GUNTER was operated for pressure scans at a fixed temperature to validate the models of response to monochromatic ^{88}Y/Be low-energy neutrons, down to nuclear recoils of O(1) keV, to define the optimal conditions of operational pressure and temperature for maximum sensitivity to low-mass dark while retaining excellent recoil rejection. Chamber upgrades that allow for sub-atmospheric pressures are expected to explore O(0.1) keV thresholds. GUNTER calibration data helped define the parameters that describe the response of the hydrogenated target R-134a to electron recoils. These studies tested the new model for electron recoil response to check for concordance with what was observed using C_3F_8. Lastly, GUNTER data served as a starting point to study the target's response to nuclear recoils, assuming a linear threshold model for bubble nucleation efficiency (see Sections 4.2 and 4.3, respectively).

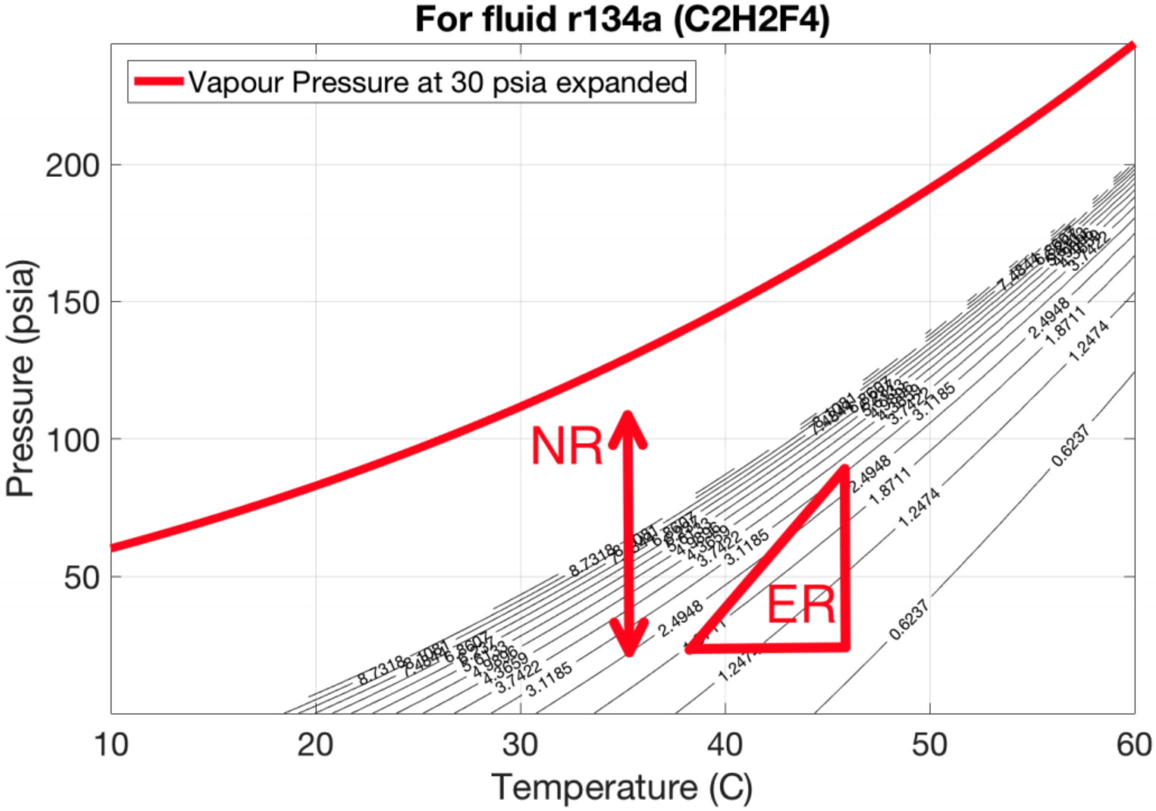

Figure 2.11: Preliminary R-134a electron recoil calibrations in GUNTER, restricted to the solid red triangle. An electron recoil (ER) rejection comparable to that of C_3F_8 was observed (see Figure 1.15). The pressure and temperature curves are labelled by nuclear recoil (NR) Seitz threshold in keV. Chamber upgrades. GUNTER was used to define the optimal regions of PICO-LM operational pressure and temperature space leading simultaneously to the minimum proton-recoil threshold and maximum electron recoil rejection. GUNTER was used for monochromatic neutron calibrations scanning pressure at fixed temperature (Collar, 2013) to expand the presently reachable $\sim$ 2 keV NR threshold, shown as a solid arrow, and expand it to below 0.5 keV, shown as a dashed arrow.

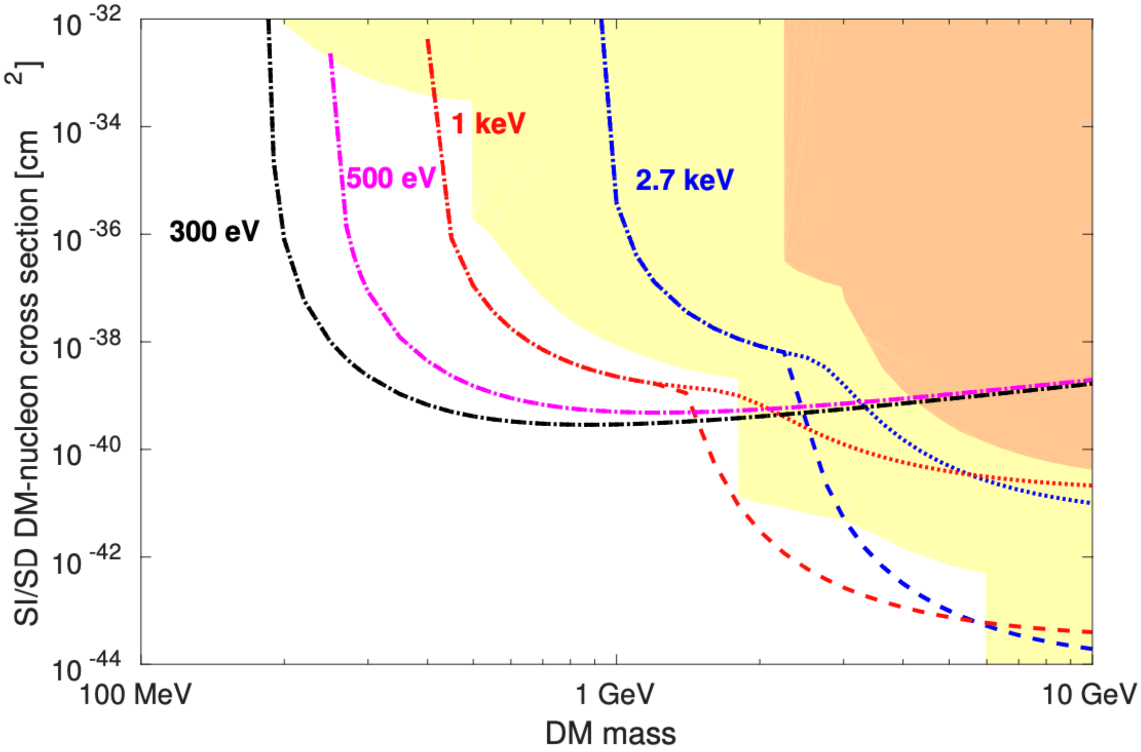

Figure 2.12: Projected SI and SD limit curves, shown as dashed and dotted, respectively, in one live-year for R-134a-filled PICO-40L under multiple assumptions for ER background reduction, labeled by operating thermodynamic threshold. SI and SD limits are identical below 1 GeV as only hydrogen contributes. The 2.7 keV curve in blue shows no improvement in the electron recoil background assuming target fluid replacement alone. The 1 keV curve in red shows a reduction of two orders of magnitude in the electron recoil background via gamma shielding, ultrapurity upgrades, and an active veto. The magenta and black curves for 500 eV and 300 eV, respectively, assume a rejection factor of 10^2 and 10^3, respectively, in electron recoil background between proton and electron recoils. One electron recoil background event per live-month is expected for the lowest three thresholds. Only proton recoils are considered in projecting the limit for the lowest two thresholds. SI and SD bounds are shown as yellow and orange shaded regions, respectively.

2.2 Critical Subsystems

A proper analysis of bubble events in the GUNTER chamber requires the extraction of many parameters via sensors, some of which are highlighted herein. Bubble events in GUNTER are registered with relevant output variables for analysis such as temperature, pressure, and acoustic information. GUNTER's temperature control is achieved with a CC-100 immersion chiller that provides 180W at -20°C and is monitored by a computer in the chamber's DAQ system through 5 thermocouple probes. Signals from the temperature and pressure sensors are fed into the National Instruments (NI) DAQ chassis for modular interfacing with LabVIEW software. The signal from acoustic sensors is managed by a two-channel Agilent U1071A fast digitizer (40 ms traces at 200Ms/s). The digitizer was mounted on the computer used as the GUNTER control station. The two pressure sensors in GUNTER are Dytran 2005V and Noshok-200 transducers. Quantitative processing of the dytran rise time allowed for the characterization of bubble event multiplicity and wall events (constrained bubble expansion). Combined with position reconstruction and acoustic information, this processing effectively implemented semi-automatic quality checks, which led to negligible contamination of events not of interest, depending on the analysis.

2.2.1 PID Temperature Control

This section discusses the theory behind the PID control algorithm and the specific PID system used for controlling heating and cooling elements in the GUNTER bubble chamber using NI LabVIEW software, NI plug-in data acquisition devices, and LabVIEW PID toolset features. A robust study of classical PID control theory and PID control of continuous processes is found in Goodwin et al. (2000) and Han and Edgar (2014). Proportional-Integral-Derivative (PID) control has been universally accepted for purposes of industrial control. It is the most widely used control algorithm in the industry, known for its robustness and wide range of operating conditions. PID algorithms consist of three coefficients: proportional,

Figure 2.13: External pump used for GUNTER. It allowed for pressures of up to 250 psig in the chamber.

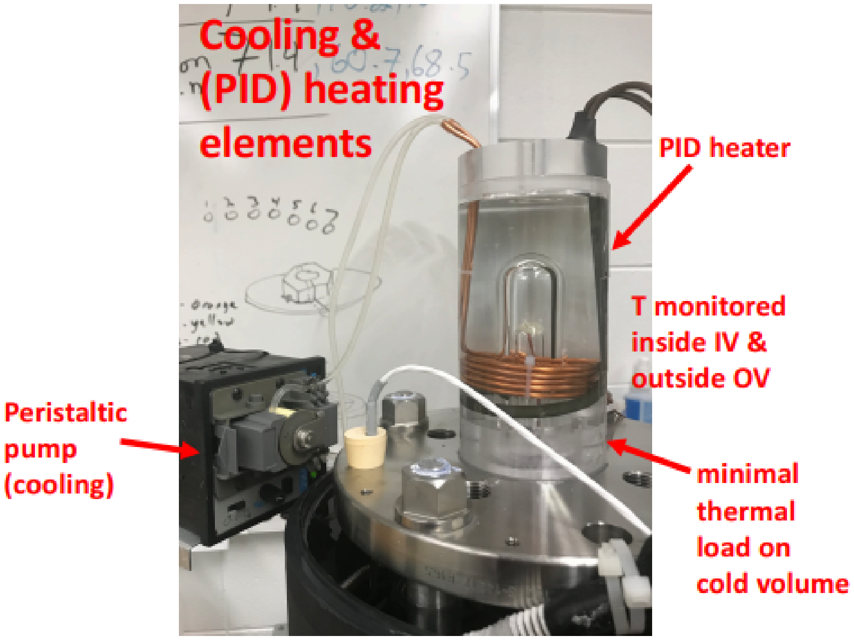

Figure 2.14: Cooling and heating elements in GUNTER with labeled components and details of operation.

integral, and derivative. These are typically fine-tuned manually or automatically to achieve optimal response. The PID control variable $u(t)$ is typically written as

$$u(t) = K_p e(t) + K_i \int e(t)dt + K_p \frac{de}{dt} \tag{2.2}$$

where K_p is the proportional value, $e(t)$ is the error value, K_i is the integral gain, and de/dt is the ratio of the change in error value to the change in time.

The system parameter in a basic control system is typically referred to as the process variable. A few of the most common process variables used in control systems are pressure, temperature, and flow rate. The process variable is measured with a sensor and used to provide feedback to the control system. The command value for a process variable is called the set point. The control system algorithm, also commonly referred to as the compensator, inputs the difference between the measured process variable and the specified setpoint to determine the command output used in driving the system or plant.

The continuous process of providing constant feedback based on sensor readings is characteristic of a closed-loop system. The command actuator output calculation is repeated at a fixed loop rate, as shown in Figure 2.15. It is worth mentioning that signals besides that of the actuator can influence the system. An example of this would be the inside of a bubble chamber exposed to sporadic waves of cool or warm air, disturbing the temperature. As a rule of thumb, control systems are designed to minimize disturbances on the process variable.

In summary, a PID controller is designed to read a sensor and compute the desired actuator output based on the sum of the proportional, integral, and derivative responses. In GUNTER, an immersion heater (see Figure 2.14) is used with a solid-state relay that switches on and off when with the application of an external voltage to modulate the flow of electric current at the rate calculated by the PID (see Figure 2.19). The PID toolset in LabVIEW was used to achieve temperature control in GUNTER (see Figure 2.17).

The error term is typically defined as the difference between the setpoint and the process

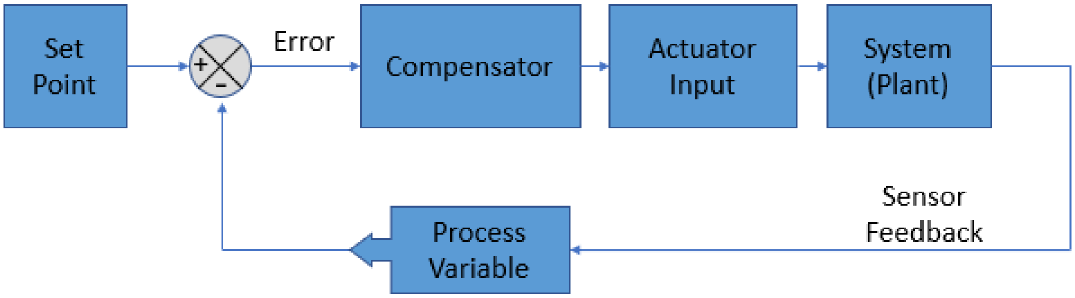

Figure 2.15: Block diagram of a typical closed loop system

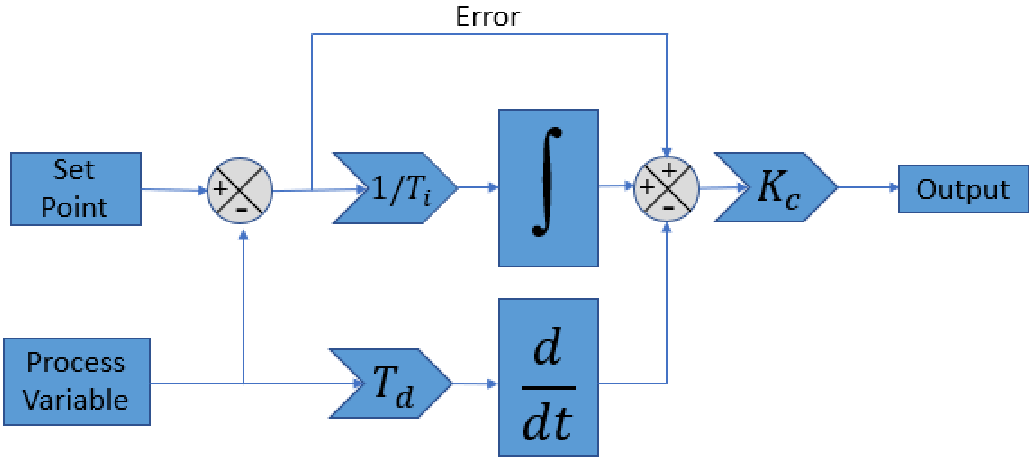

Figure 2.16: Block diagram of a basic PID control algorithm

variable. The proportional component of a PID depends only on the error term, and the proportional gain (K_c) determines the output response to the error signal ratio. For example, a proportional gain of 3 would produce a proportionate response of 30 if the error term has a magnitude of 10. It is generally the case that increasing the proportional gain increases the speed of the control system response. However, the process variable begins to oscillate if the proportional gain is too large. Hence, a system could become unstable if K_c is increased further and oscillations become larger.

The sum of the error over time corresponds to the integral component. The steady-state error is the final difference between the process variable and setpoint. The saturation of a controller by the integral action is known as integral windup. The derivative component of a

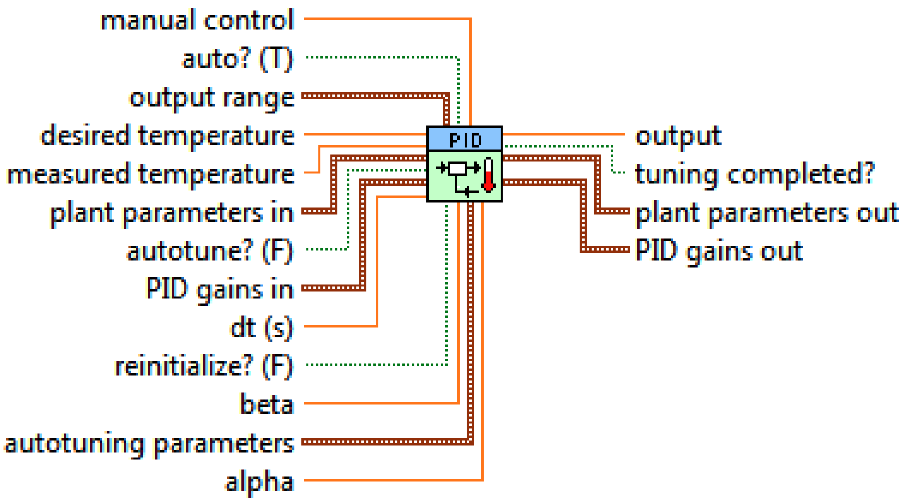

Figure 2.17: PID Autotuning (Temperature) VI. The VI was used in manual control to directly control and tune the system. It can be seen within the GUNTER PID controller VI (see Figure 2.17).

PID decreases the output if the process variable increases too quickly and is proportional to the rate of change of the process variable. An increase in the derivative time (T_d) parameter causes the control system to respond more aggressively to changes in the error term and increases overall control system response speed. However, most practical control systems use a small derivative time given how sensitive the derivative response is to noise in the process variable signal. It is common to have an unstable control system if the sensor feedback signal is too noisy or if the control loop rate is too slow.

A control system response is tuned by finding the optimal gains for P, I, and D. For instance, a popular method of tuning a PID controller, is the Ziegler-Nichols method, where I and D are fixed at zero and P is increased until the loop starts to oscillate. Upon oscillation, it is possible to note the critical gain K_c and the period of oscillation P_c, and with this information, P, I, and D are then adjusted. The PID yields excellent results for temperature control in GUNTER (see Figure 2.18) and proved successful throughout all runs.

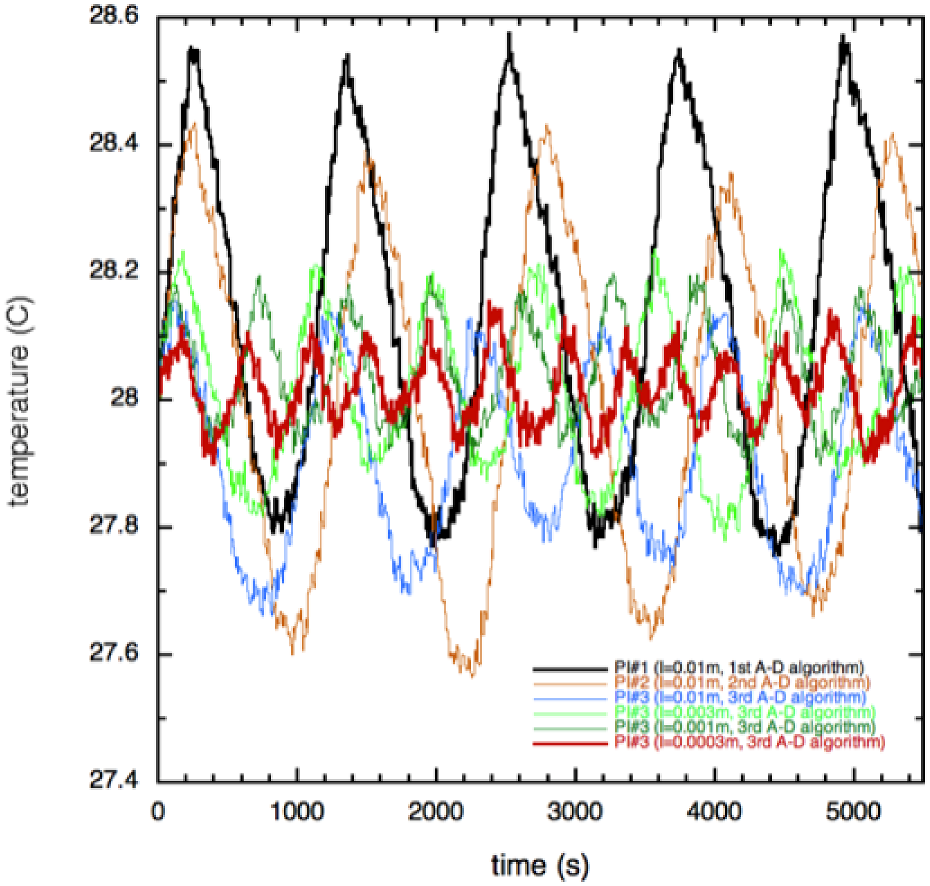

Figure 2.18: GUNTER PID temperature control optimization achieved by fine tuning parameters and monitoring performance. Details of each manual tuning iteration can be seen in the bottom right, where the parameters that optimized temperature stability in GUNTER are shown in red.

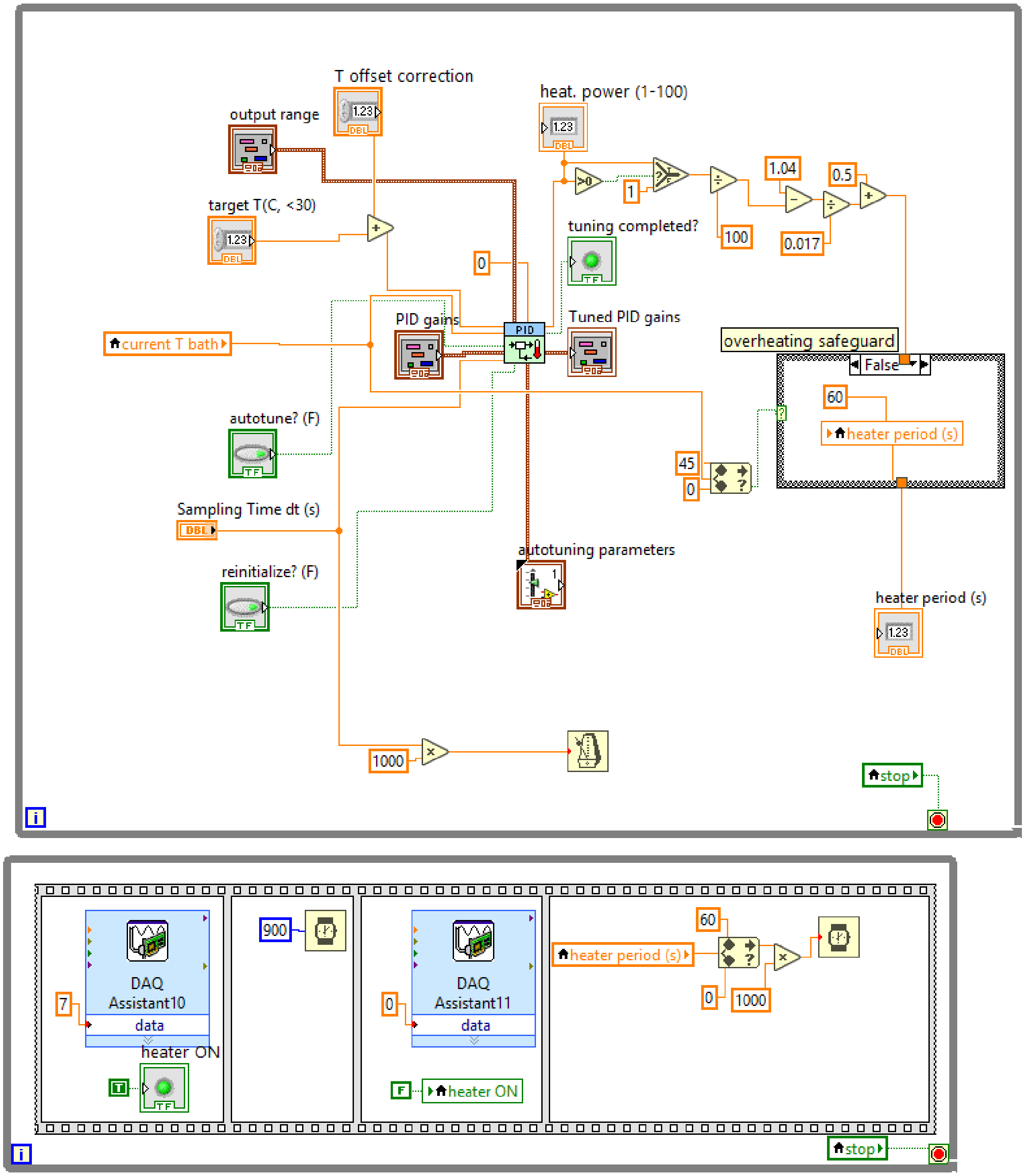

Figure 2.19: GUNTER PID controller VI with the connection to the solid-state relay at the bottom. The PID output controls the rate at which the relay switches with voltage inputs, adjusting for optimal stability around the setpoint temperature.

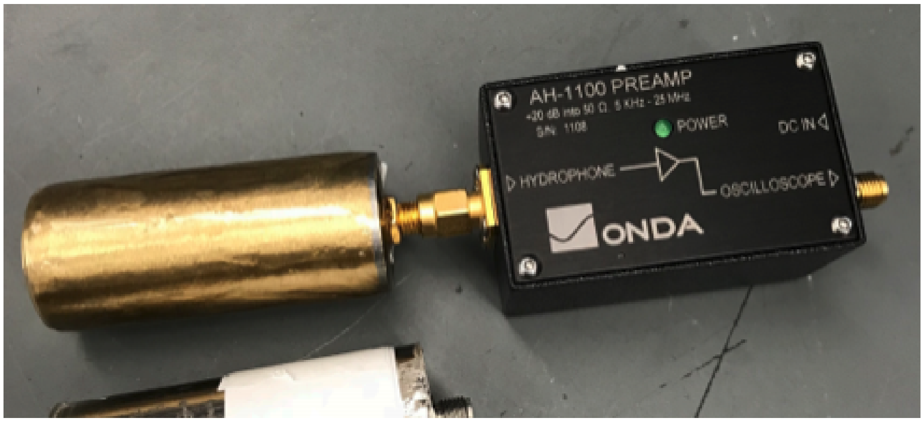

Figure 2.20: Snapshot of a piezoelectric sensor tested on GUNTER. Mechanical stress across specific materials can produce a charge known as piezoelectricity. Piezoelectric pressure sensors exploit this phenomenon by measuring the voltage across piezoelectric materials generated when mechanical stress is applied. A review of techniques for characterizing piezoelectric materials for transducer applications can be found in Sherrit and Mukherjee (2007).

2.2.2 Acoustic Detection System

PICO has demonstrated that information from the microscopic processes leading to the formation of proto-bubbles survives into the acoustic signal. Hence, PICO acoustic efforts have benefited from high and low-frequency piezoelectric sensor development. This acoustic information has been used to classify bubbles induced by alphas in PICO targets. The detection of higher frequencies is expected to provide information from the earlier process of bubble growth. Collaboration efforts have confirmed via simulation of proto-bubble growth and its acoustic generation that particles with a relatively low stopping power favor emissions at the highest frequencies, as with alphas. This phenomenon was also observed in PICO-60 acoustic data, and it is hypothesized that longer proton track lengths could signal at lower frequencies. Through further upgrades of bubble chamber acoustics access to higher frequencies and improved sensitivity, the collaboration aims to develop electron and proton recoil identification models.

PICO has conducted multiple sensor evaluations to study the response of different piezoelectric sensor designs. A combination of sensor performance studies is shown in Figure 2.22,

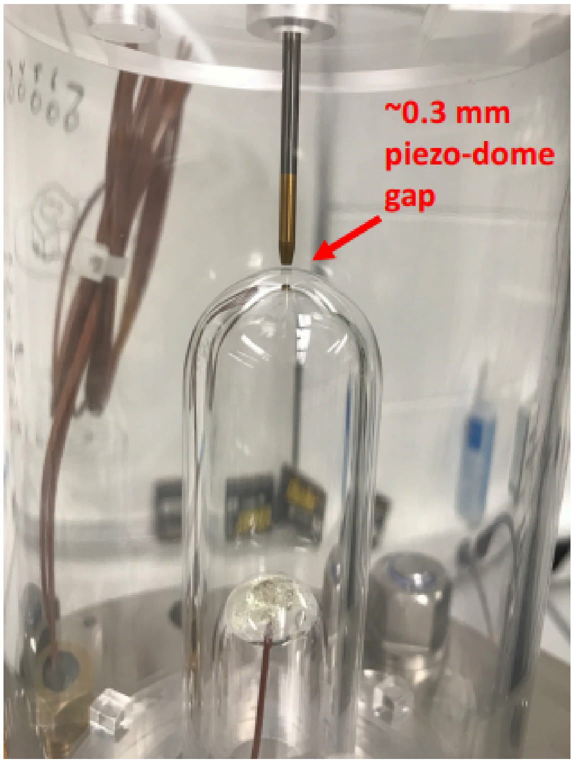

Figure 2.21: GUNTER piezoelectric transducer as seen from at the top of the outer vessel, epoxied into a ~ 0.3 piezo-dome gap to pick up the acoustic signals from bubble expansion.

wherein the IUSB group demonstrated that 1mm-transducers are sensitive up to at least 3 MHz. They also showed that when the transducer is not back-filled with epoxy, the sensitivity at frequencies below 30kHz is doubled. Hence, larger mass piezoelectric elements are favored for enhanced low-frequency sensitivity. As such, the IUSB group continues to design and construct new sensors informed by evaluation and simulation results, exploring new piezoelectric materials in the process. Examples of piezoelectric materials developed at PSU are shown in Figure 2.23. Different combinations of composition doping and ceramic geometries are used for optimizing piezoelectric response. PNNL is currently exploring alternatives to standard sensor design by testing multiple commercial devices as well. The GUNTER calibration chamber was used to test the design of seven different piezoelectric sensors during C_3F_8 operation (see Section 3.3). GUNTER chamber acoustics are monitored by an ONDA Corporation HNC-1500 piezoelectric needle hydrophone to provide a flat response to multi-

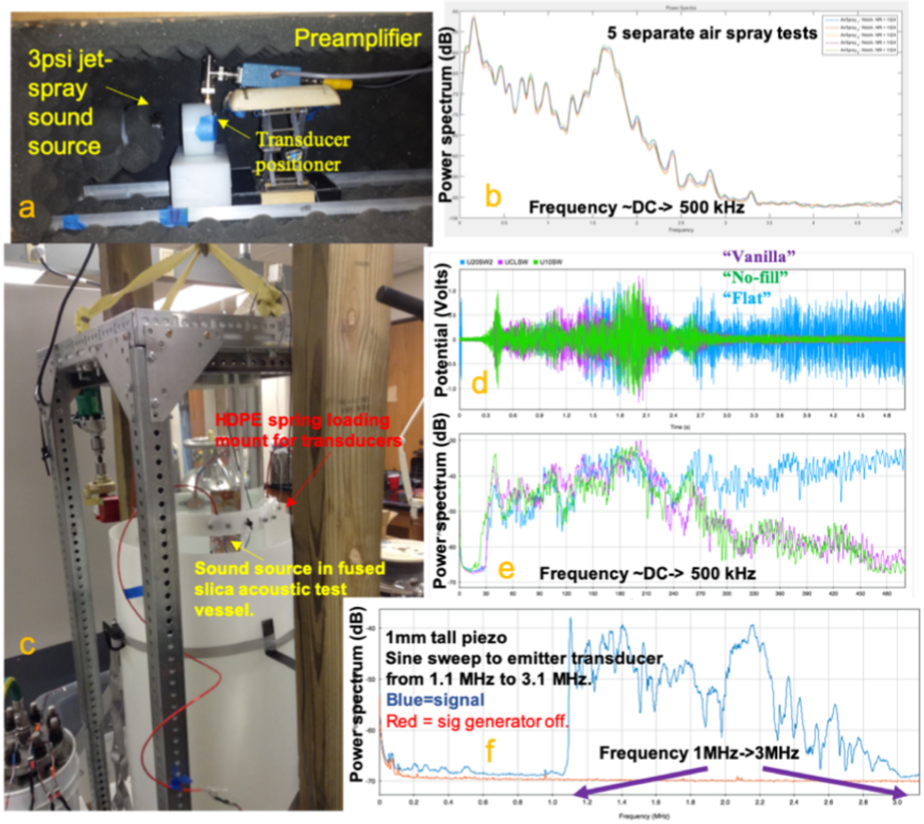

Figure 2.22: Example of piezoelectric transducer measurement and characterization system performed by the IUSB group. The group showed that 1mm-tall transducers are sensitive up to at least 3 MHz and that the sensitivity is almost doubled at frequencies below 30 kHz if the transducer is not back-filled with epoxy.

ple tens of MHz. At three orders of magnitude higher in frequency than the range presently available to PICO transducers (see Figure 2.9), this represents a much earlier stage of bubble development, closer to the spatial scale where electron, nuclear, and proton recoil differences are expected to arise.

2.2.3 Entropy Trigger

Entropy-based motion detection consists of using consecutive images to calculate the difference image at each particular pixel (Chang and Cheng, 2007). This method has been demonstrated to be an effective, reliable, and robust alternative to the background sub-

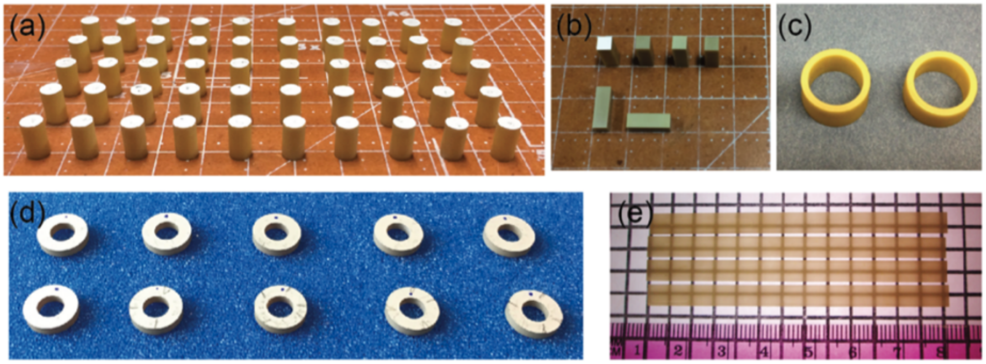

Figure 2.23: The fabrication of piezoelectric components at PSU: (a) standard acoustic transducers used in PICO dark matter searches made from radio-pure Nb-doped PZT ceramics. (b)—(e) PMN-PT and PMN-PZT textured piezoelectric ceramics with varying vibration modes.

traction method, which instead depends on maintaining a background model for successful motion detection (Sehairi, Fatima, and Meunier 2018). Hence, similar to PICO-60, entropy was used as the criterion for bubble detection in GUNTER. The trigger is defined quantitatively as the image entropy S_I of the absolute difference of the frame and the preceding frames, where

$$S_I = -\sum_i P_i \log_2 P_i. \tag{2.3}$$

The difference-images are used to construct an image histogram. The values P_i are the probabilities of pixel intensity falling into intensity bin i, so the number of pixels normalizes the histogram. The quantity S_I for this difference image is calculated via the sum in Equation 2.3 over the bins of the normalized image histogram. S_I is then compared to each camera's predefined threshold and tuned high enough to avoid triggering with pixel noise.

The entropy trigger is built entirely with LabVIEW 2015 and requires the NI Vision Development Module to run. It allows for built-in visual interfaces (VIs) to consolidate camera control and image processing in GUNTER. The GUNTER entropy trigger graphical interface is shown in Figure 2.24. An example of the entropy trigger at work is shown in Figure

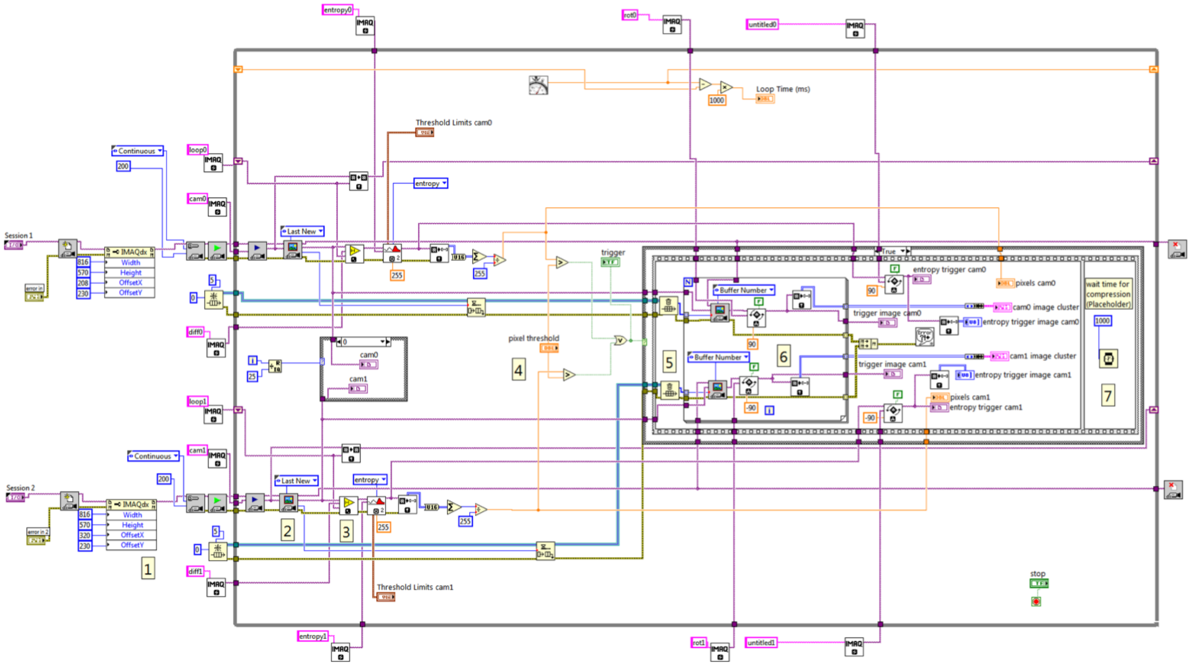

Figure 2.24: GUNTER entropy trigger VI.

2.25. Its steps are labeled and sequenced as described in the PICO technical documentation for GUNTER docdb3739 written by A. Ortega:

1. Camera configuration occurs before entering the acquisition loop. A manual region of interest (ROI) is created; the image shape changes from 1280x1024 to 816x570 for each camera, focusing on the quartz vessel.

2. Two different frames are used during acquisition: the image from the previous loop and the most recently captured. It was noted that there were skipped frames due to the camera frequency being 169 fps and the loop frequency of 83 Hz, leaving approximately one frame difference between images.

3. The absolute difference between images is computed and fed into the IMAQ AutoBThresholding2.vi, which handles the following two steps internally:

    - Calculate the entropy or available intensity states (0-255) for each pixel

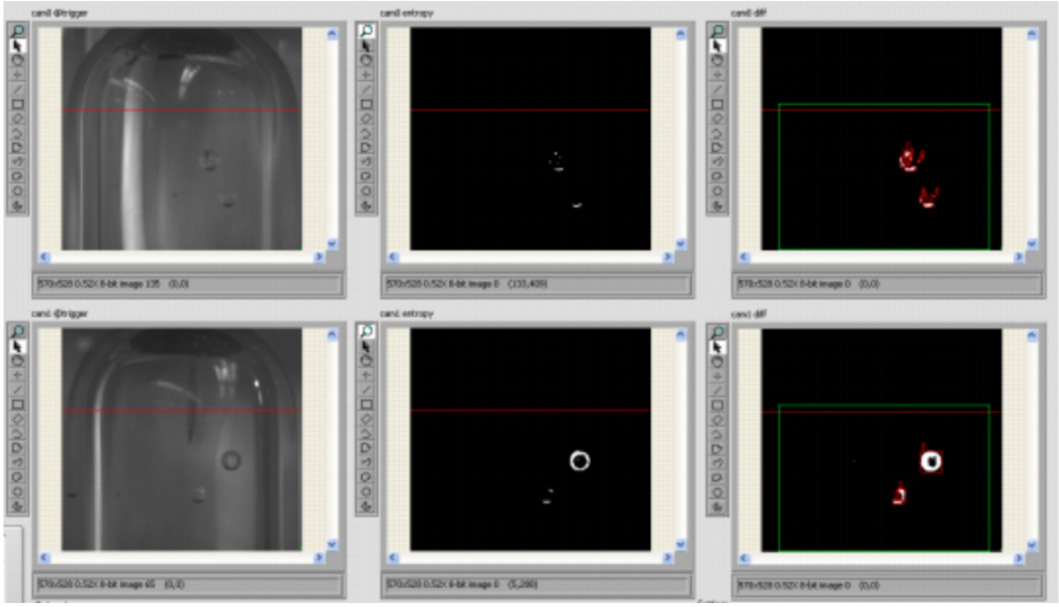

Figure 2.25: Example case of the entropy trigger during a nuclear recoil event (double bubble event).

  - Search for bright objects in the image pixels with values greater than those computed via the threshold method. e.g., entropy (see Figure 2.23).

  In the case of GUNTER, the entropy values of camera0 are [23,50], so the threshold was tuned such that pixels within this range are set to a threshold of 0 (black), and that outside and greater to 255 (white). This, in turn, would result in purely black images (zero matrices).

4. A trigger condition of 10 pixels per camera is defined due to occasional pixels outside the threshold range.

5. The queue continually updates pre-trigger. Trigger events immediately empty the queue and reference which images to store.

6. At trigger, the following images are rectified and saved per camera: trigger frame, with and without threshold, and the four previous images.

7. The acquisition loop pauses and is set to wait for compression and expansion to finish.

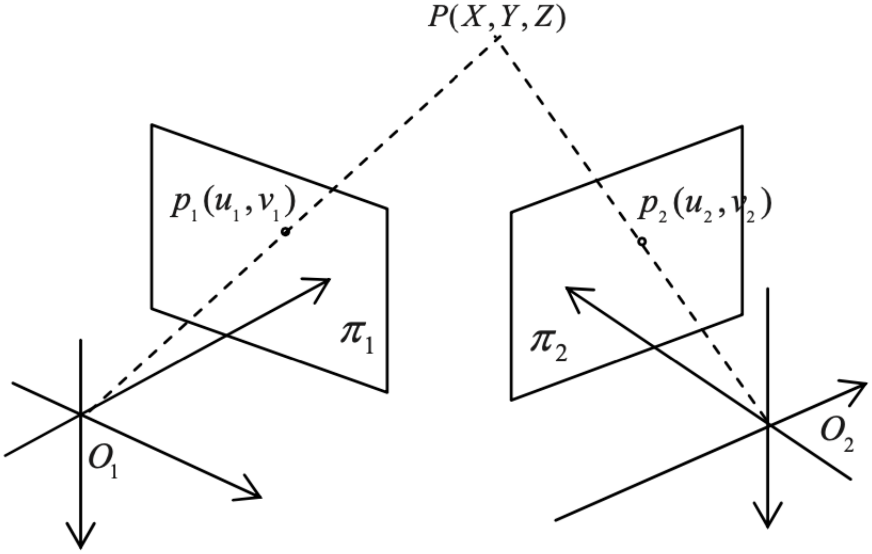

Figure 2.26: Basic geometry of a stereovision system, akin to the camera system mounted on GUNTER and used for position reconstruction of bubble events within the active volume. Figure from Hu and Yang (2007) reproduced with permission.

The cameras have no dead time, however.

2.2.4 Neural Networks for Position Reconstruction

The GUNTER calibration chamber is monitored by two stereoscopic high-resolution Basler Ace acA1300-200μm cameras. The emphasis of this chamber camera system is to obtain the best possible spatial reconstruction of bubbles generated during high-statistics electron, nuclear and proton-recoil calibrations. This is required to isolate dependencies in bubble position that might otherwise confound the identification of frequency-dependent signatures leading to particle identification. Neural networks are commonly trained to perform complex functions across many fields, solving atypical problems for conventional computers or human beings. They are typically found in applications of pattern recognition, identification, and classification, to name a few. Hence, neural networks were the choice for 3D position reconstruction in GUNTER, given their demonstrated ability to generalize information and learn nonlinear relationships between two and three-dimensional coordinate systems (Pedra et al., 2013). For a thorough overview of image-based 3D reconstruction and deep learning trends refer to Han, Laga, and Bennamoun (2019).

Spatial reconstruction in GUNTER allows the extraction of coordinate information for each bubble event within the well-defined cylindrical volume. The basic geometry of a stereovision system akin to the camera system mounted on GUNTER is shown in Figure 2.26. The camera calibration technique used for GUNTER was the double plane method. This technique develops a camera model that establishes a geometrical relationship between image points in 3D coordinates and image pixels in 2D coordinates and vice versa. Two images taken at different angles of the outer vessel wrapped with a delineated 3D grid were used for this purpose. Columns 1-3, 5, 6, 8-13, 15, 18, 19 can be observed simultaneously by both cameras, providing 18 x 6 (horizontal lines spanning 2.5 cm) = 84 fiducial vectors for neural network training. Figure 2.27 shows the fiducial markings implemented using a cylinder ($r = 1.5$ cm) of transparent plastic film snugly wrapped around the surface of the outer vessel. This cylindrical film has the advantage of being easily removable, leaving no permanent marks on the vessel.

The neural networks were developed with Matlab's Neural Network Toolbox (NNT), specifically the Neural Fitting application (nftool). This application prompts the user to select data, create and train a network (see Figure 2.28), and evaluate its performance. The evaluation metrics are calculated using mean square error and regression analysis. Neural network fitting maps between a data set of numeric inputs and a set of numeric targets. For the purpose of calibrating the cameras mounted on GUNTER (see Figure 2.30), the four numeric inputs are the x and y pixel coordinates extracted from the corresponding grid vertices in the two images, and the numeric targets are the known x, y, and z coordinates at each vertex from the geometry of the outer vessel. Even with the coarse mesh of training fiducials used, the network converged comfortably after $\sim$180 epochs.

The only noticeable issue is a blind spot unrelated to the ANN but instead due to dark

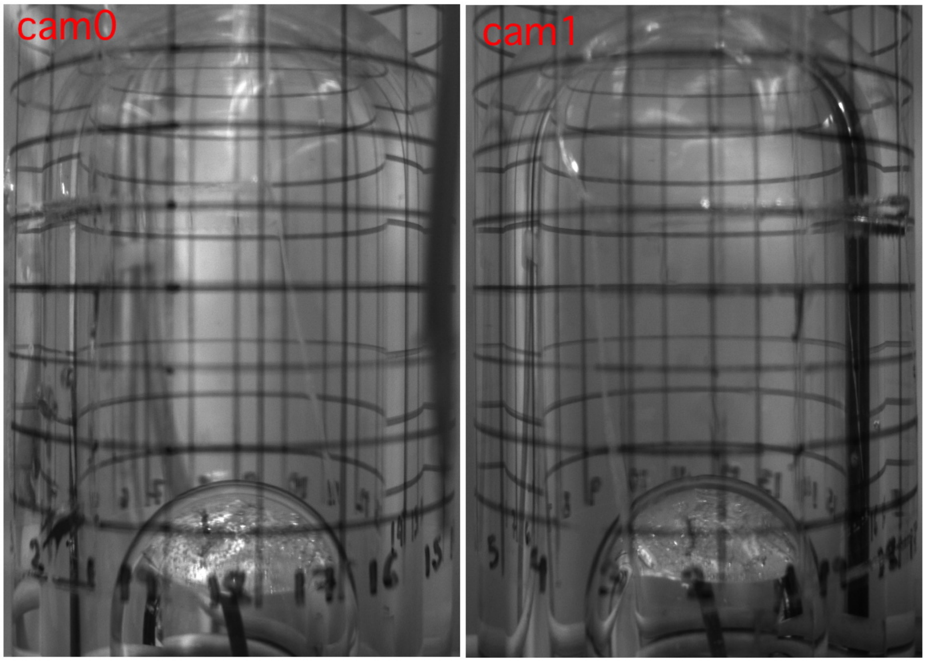

Figure 2.27: Outer vessel grid images for camera calibration using ANN's. On it, there are nineteen equally-spaced numbered vertical columns and several horizonral rows separated by 0.5 cm, the reference marks being their intersections.

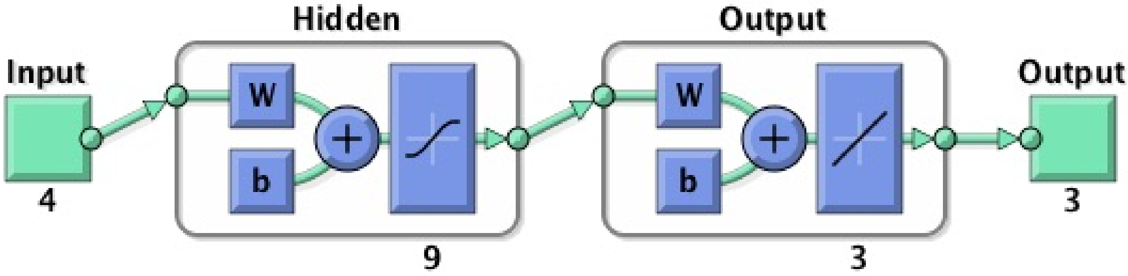

Figure 2.28: ANN architecture for position reconstruction in GUNTER. The architecture diagram highlights a two-layer feed-forward network with sigmoid hidden neurons and linear output neurons. Early stopping is implemented automatically to avoid overfitting. Multi-dimensional mapping problems are fit arbitrarily well assuming consistent data and enough neurons in the network's hidden layer.

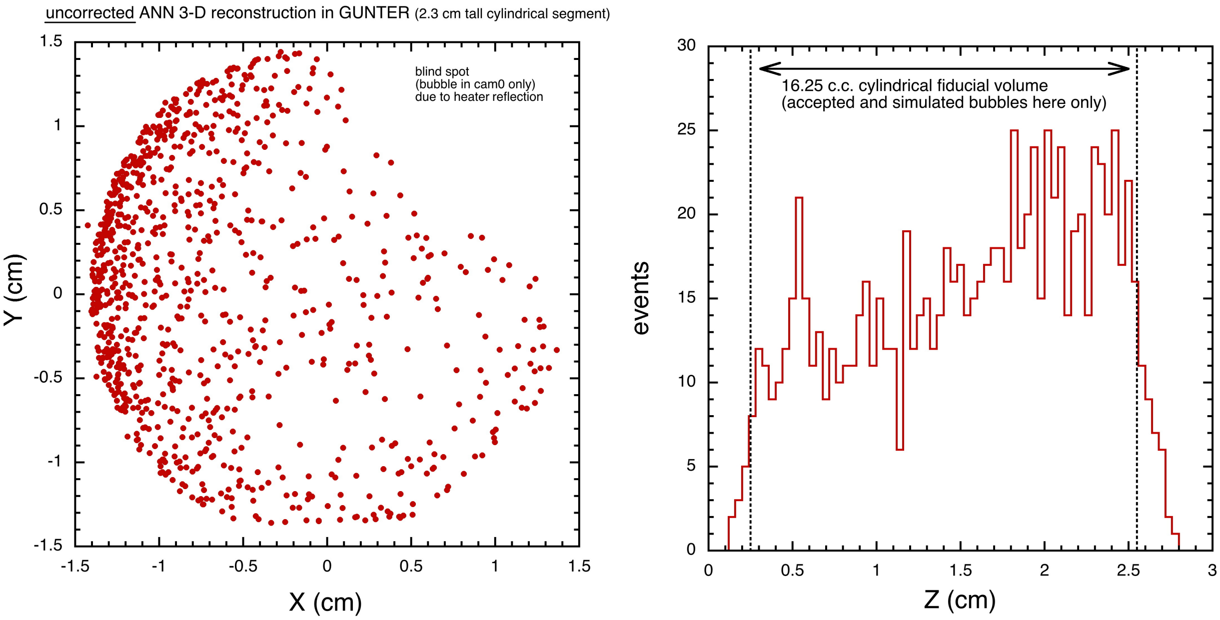

Figure 2.29: Example ANN 3D position reconstruction of bubble events in the active volume of GUNTER using C_3F_8. Left: example x and y position reconstruction of bubble events in GUNTER. Right: example z distribution of reconstructed bubble events within the 25 c.c. of cylindrical fiducial (active) volume. The z distribution reflects the location of the source.

reflections of the heating coil, which limits the visibility of bubbles through camera 1 in that spatial region (see Figure 2.29). A similar phenomenon was observed due to more minor reflections from the copper cooling coil at large negative y values (see Figure 2.29). These issues were ultimately addressed for future runs using white ceramic paint and additional fiducial markings but to little effect in improving position reconstruction. Notwithstanding, spatial reconstruction for GUNTER calibration studies pioneered the use of ANNs for bubble chamber applications. ANNs are expected to simplify bubble position reconstruction significantly in PICO-40L and beyond when in the past, the collaboration has struggled with necessary corrections to the ray-tracing method for bubble position reconstruction.

2.2.5 Bubble Finding Algorithm

A fully automatic bubble finding algorithm was developed to sift through GUNTER datasets and implement quality cuts on the data with the goal of ultimately only accepting high

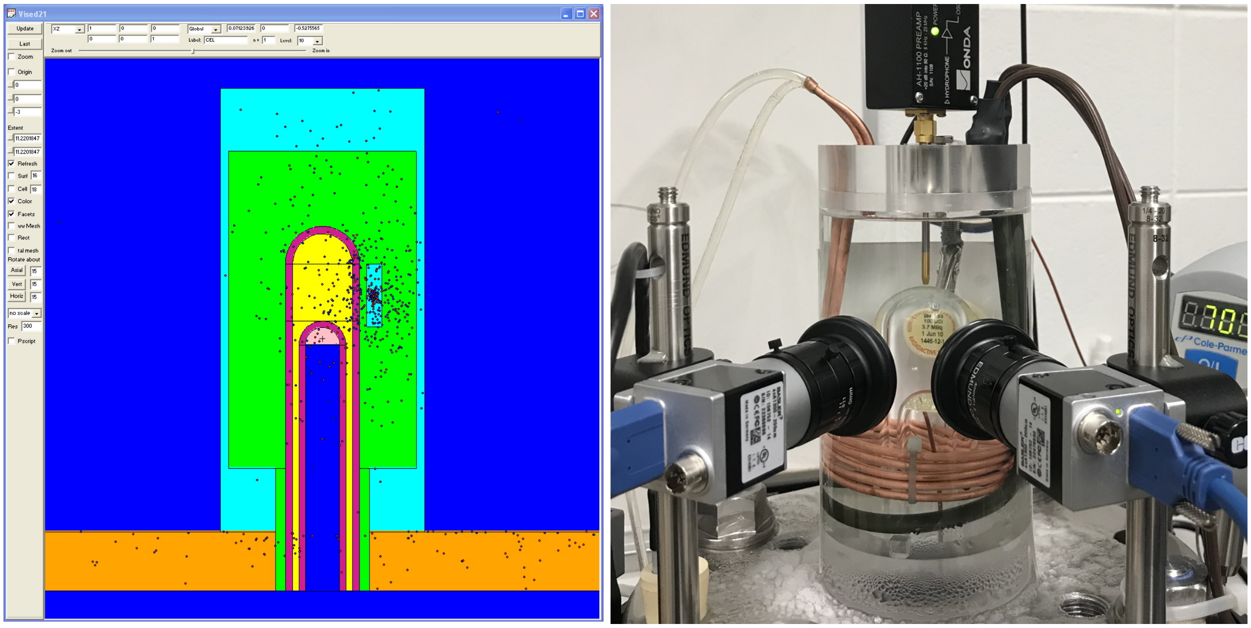

Figure 2.30: GUNTER simulation side-by-side comparison

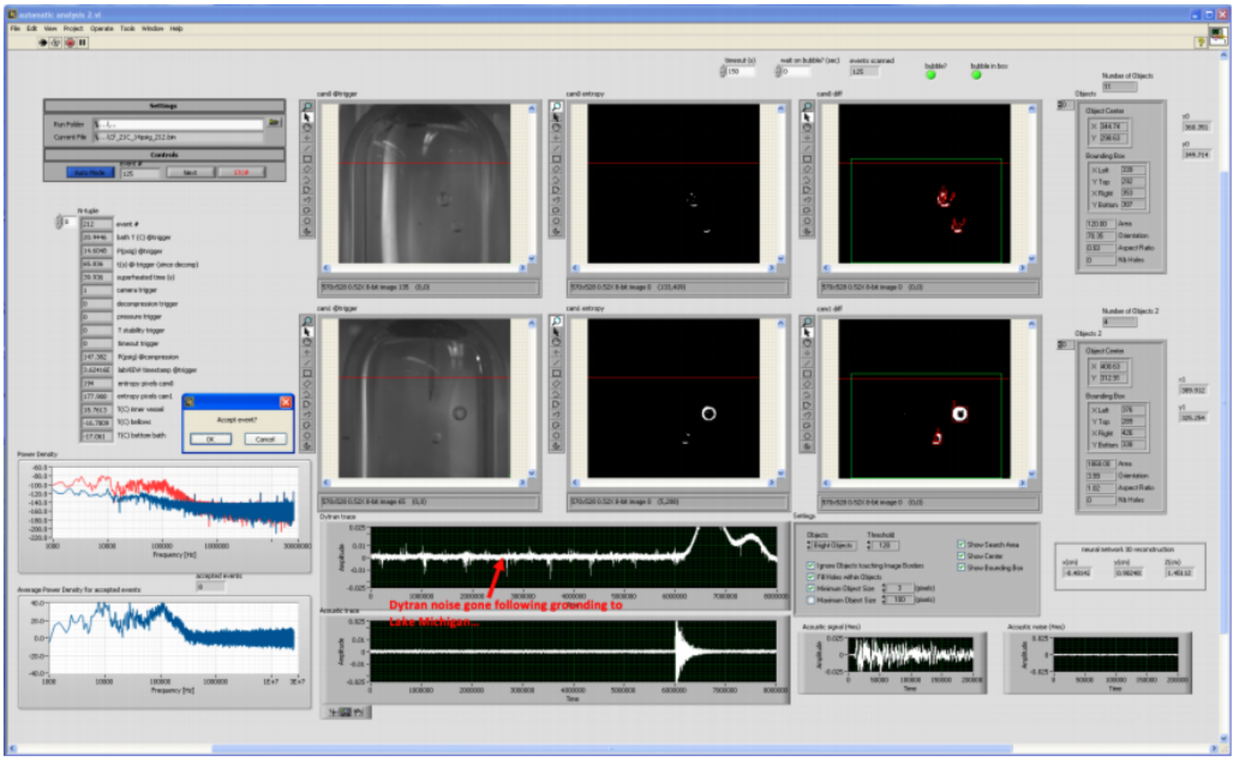

Dytran noise gone following grounding to Lake Michigan...

Figure 2.31: Control panel of the GUNTER bubble finding algorithm VI.

confidence bubble events of interest. The algorithm can accurately find the centroid of sub-millimeter bubbles and $\sim$1 cm big splashes against the wall at high degrees of superheat. The program iterates over each event in the selected dataset folder. It unpacks the binary data and processes the acoustic, image, and thermodynamic information registered from the event, implementing a series of conditions that weed out bubble events that are not of interest. Suppose an event meets all the bubble conditions put in place. In that case, the user is prompted at the end to either reject or accept the event, allowing for one last manual check before determining whether to write to file for post-processing and analysis (see Figure 2.31).

CHAPTER 3

C_3F_8 STUDIES

The GUNTER C_3F_8 datasets and deliverables were multipurpose by design. This chapter discusses the high-statistics tests of electron recoil response using ^{133}Ba to define the free parameters of a new bubble nucleation model developed by the collaboration and how it allowed for the measurement of electron recoil rejection at the planned parameters for low-mass PICO-40 operation, specifically at the ^{133}Ba 15C and 5 psig datapoint, which had not been previously measured and is necessary for determining the expected background of PICO-40 runs. In a similar vein, GUNTER was used to collect C_3F_8 neutron calibration data in planned PICO-40L conditions down to 2.25 keVnr (see Figure 3.1). This dataset was not analyzed for this thesis, given that this calibration has already been conducted multiple times within the collaboration. However, this calibration was completed with the hydrogenated target R-134a. Section 4.3 will discuss this calibration method in detail and summarize its results. GUNTER served as a testbed for acoustic sensor design using electron-induced bubbles and drawing conclusions regarding high-frequency emission. This chapter also includes the acoustic analysis results from high-statistics electron and nuclear recoil datasets acquired using the weak ^{252}Cf and intense ^{124}Sb sources. Details of the electron recoil analysis and fit methodology are included in Appendix A.

3.1 Electron Recoil Mechanism and Response Parameters

Electron recoils in C_3F_8 are different from nuclear recoils in that they are characterized by being non-local on the scale of the critical radius. Hence, each δ-electron produced via ionization behaves as a nucleation trial. PICASSO had previously shown that the probability of electron recoil nucleation scales with δ-electron production in C_4F_{10} (Archambault et al., 2011). The collaboration considered instead the probability of bubble nucleation per

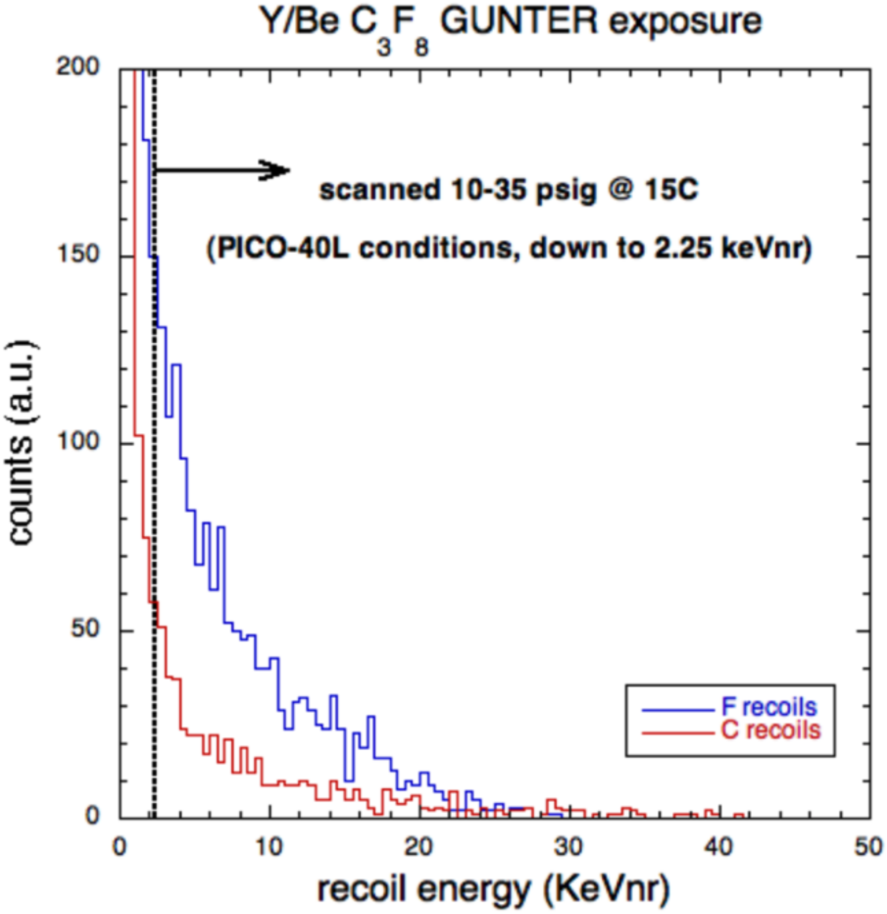

Figure 3.1: Simulated rates for ^{88}Y/Be 10-35 psig pressure scan at 15°C for GUNTER C_3F_8 neutron calibration. Simulated fluorine recoils are shown in blue and simulated carbon recoils in red.

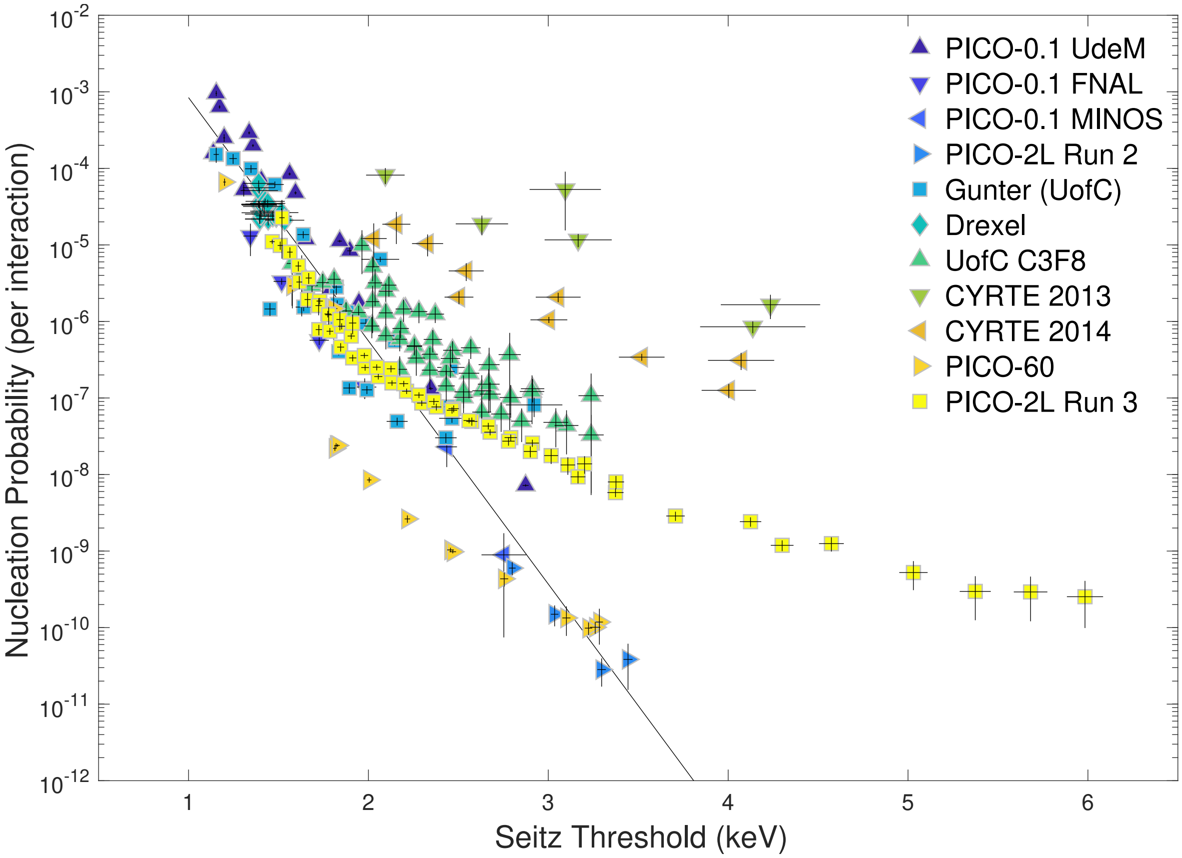

Figure 3.2: Traditional Seitz model (black line) for electron recoil bubble nucleation in C_3F_8, wherein the probability of bubble nucleation from electron recoils is a function of the Seitz threshold alone. The traditional Seitz model fails to describe bubble nucleation in pure C_3F_8 data to within an order of magnitude.

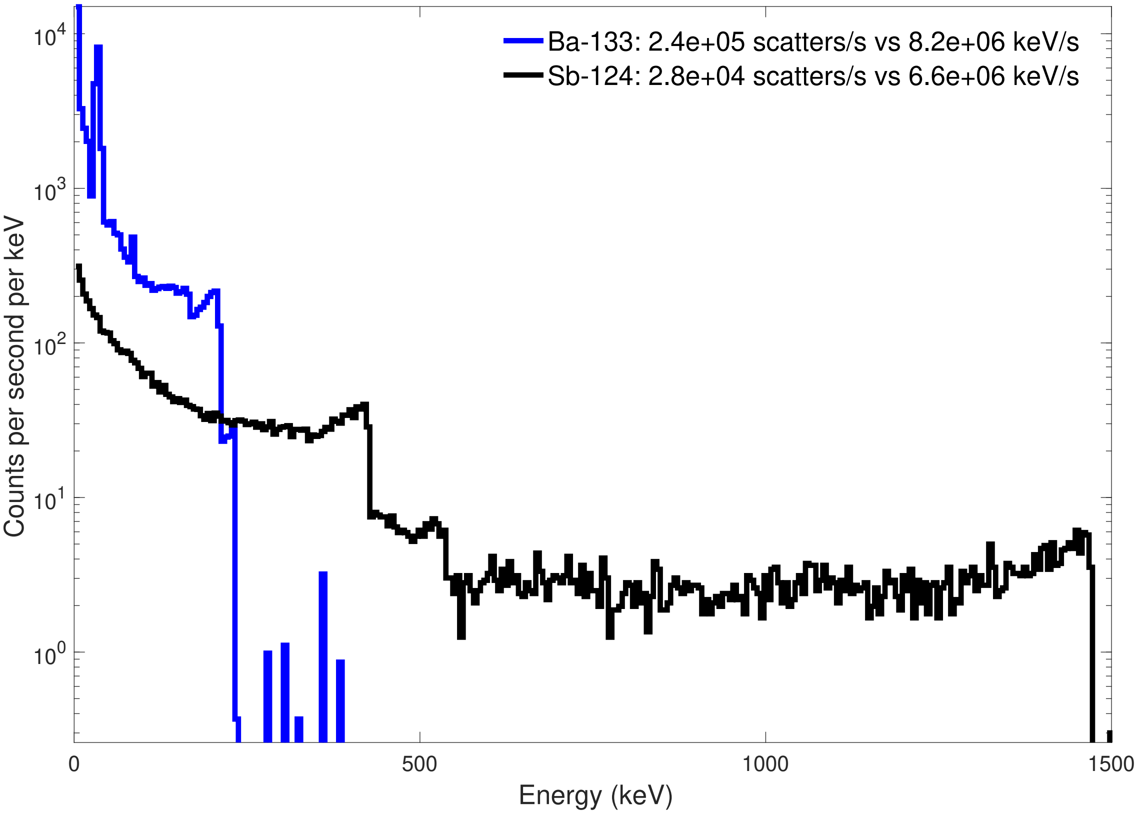

Figure 3.3: Simulated energy spectra deposited in GUNTER for photons originating from external ^{133}Ba (blue) and ^{124}Sb (black) sources. The placement of these sources is defined such that the difference in photon scattering rates is maximized while the energy deposition rates remain roughly equivalent.

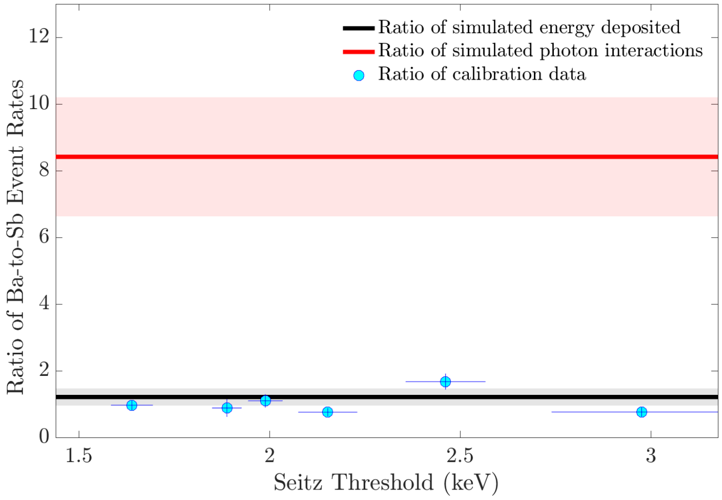

Figure 3.4: Ratio of measured event rates in GUNTER from exposure to ^{133}Ba and ^{124}Sb. Predictions from simulation are shown with 15% uncertainty bands and are given for the ratio of simulated photon interactions (red) and the ratio of simulated energy deposited. GUNTER calibration data favor bubble nucleation probability scaling with energy deposited for all Seitz thresholds explored.

total energy deposited on the basis that the δ-electron spectrum is independent of incident particle energy (Barnabe-Heider et al. 2005) (see Figure 3.2). GUNTER C_3F_8 calibration data allowed the collaboration to directly test this assumption by comparing the observed rates from ^{124}Sb and ^{133}Ba calibration sources.

The two sources were placed next to the GUNTER active volume such that the expected rate of energy deposited was roughly equal with a factor ∼8 difference in the rate of photon scatters due to the different energy spectra of the two sources (see Figure 3.2). The combined values of the Ba-to-Sb rates resulted in an observed ratio of 0.92 ± 0.07 (see Figure 3.3). This observation rejected the original hypothesis of nucleation probability scaling with scattering vertices (p-value of 2.8×10^{-5}), and it favored nucleation probability scaling with energy deposited (p-value of 0.28). The ionization threshold model for electron recoils allowed the collaboration to revise its understanding of the probability of nucleation per keV of deposited energy for all pure C_3F_8 calibration data (see Figure 3.5).

The electron recoil analysis considered the probability of nucleation $\mathcal{P}$ per trial (energy

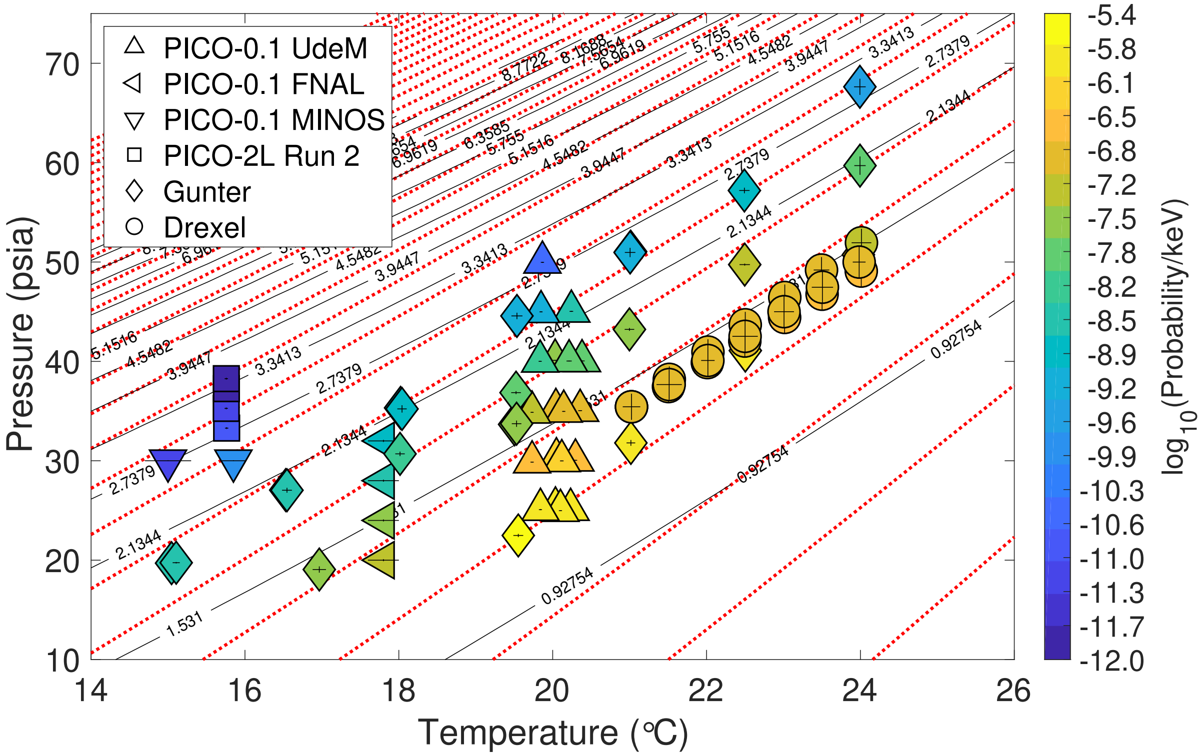

Figure 3.5: Pressure and temperature conditions of all PICO gamma calibrations using pure C_3F_8. The color axis represents the probability of bubble nucleation per keV of energy deposited for each. Shown in black, with listed values in units of keV, are the lines of constant Seitz threshold (nuclear recoil threshold). Shown in dotted red are the lines of constant stopping power using an ionization energy threshold. On the bottom left, taken with GUNTER, are the data points for the planned parameters of the PICO-40 low WIMP mass run.

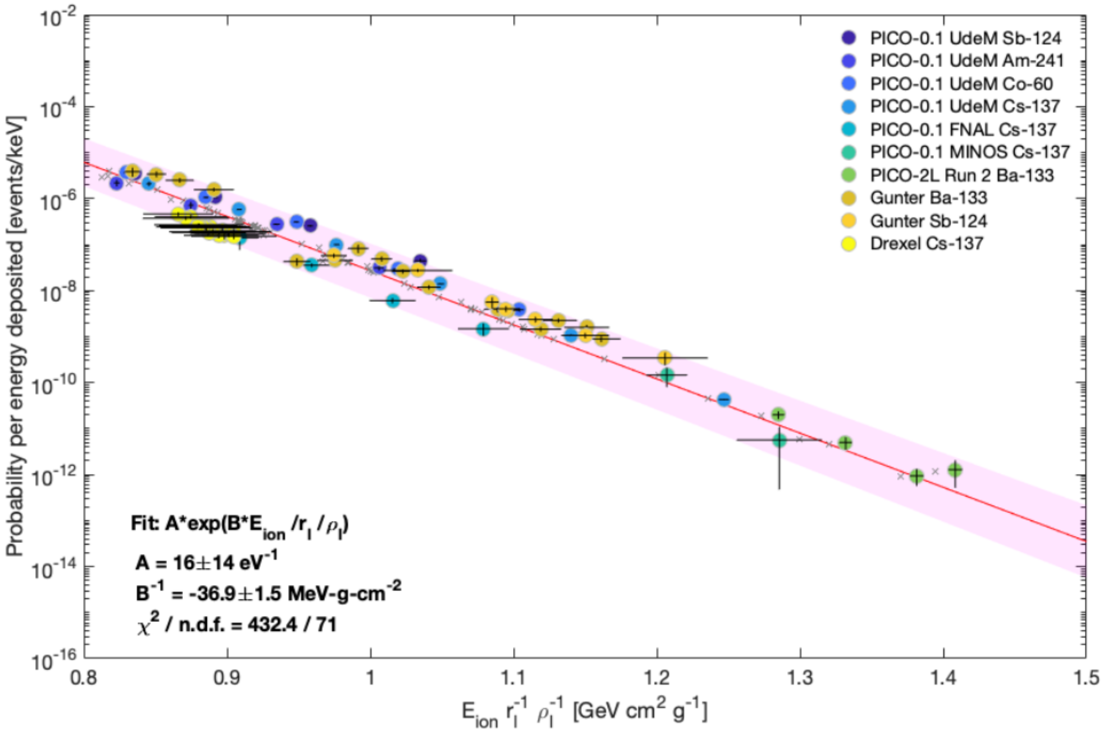

Figure 3.6: Probability of bubble nucleation per keV of energy deposited by electron recoils as a function of stopping power assuming an ionization energy threshold in C_3F_8. The best fit model is shown in red and calibrations are included with statistical error bars. The band indicates the symmetric relative uncertainty of the fit.

Dataset	Detector	Fluid	Year Operated	Calibration Sources
1	PICO-0.1 FNAL	C_3F_8	2012-2013	^{137}Cs
2	PICO-0.1 MINOS	C_3F_8	2013	^{137}Cs
3	PICO-0.1 UdeM	C_3F_8	2014-2015	^{60}Co,^{124}Sb,^{137}Cs,^{241}Am
4	PICO-2L Run 2	C_3F_8	2016	^{133}Ba
5	Gunter (UofC)	C_3F_8	2018	^{124}Sb,^{133}Ba
6	Drexel	C_3F_8	2018	^{137}Cs
7	U. of Chicago	C_3F_8 (+ I^+)	2013-2014	^{57}Co,^{88}Y
8	CYRTE	C_3F_8 (+ I^+)	2013-2015	^{88}Y, ^{124}Sb
9	PICO-60	C_3F_8 (+ I^+)	2016-2017	^{60}Co,^{133}Ba, ambient
10	PICO-2L Run 3	C_3F_8 (+ I^+)	2017	^{60}Co,^{133}Ba, ambient
11	COUPP-2kg	CF_3I	2008	^{137}Cs
12	COUPP-4kg	CF_3I	2012	^{60}Co,^{133}Ba
13	U. of Chicago	CF_3I	2012-2013	^{88}Y

Figure 3.7: Gamma calibration datasets taken using PICO C_3F_8 bubble chambers.

deposition) as the negative exponential of a pressure and temperature dependant function

$$\mathcal{P} = Ae^{-Bf(P,T)}, \tag{3.1}$$

where A and B are unknown free parameters and $f(P,T)$ is forced to scale with pressure and temperature. Implicit assumptions about what constitutes a trial are contained in A. However, the underlying nucleation mechanism at the lowest level is unknown, making the proper definition of a nucleation trial unclear. Figure 3.6 shows the best fit model for nucleation probability and best fit values for the exponential parameters. The E_{ion} range probed was 0.63–1.67 keV, wherein the stopping power of an electron is ~ 100 MeV cm^2 g^{-1} (Berger et al., 2017). Something worth noting is that the best fit value for B^{-1} is roughly half the stopping power of an electron within the range of E_{ion} probed, suggesting that the model may only have one free parameter A, as explained in (Amole et al., 2019). This semiempirical model spans seven orders of magnitude in nucleation probability and is constrained primarily by GUNTER calibration data, which provides the broadest coverage to date in pressure-temperature space for C_3F_8 calibrations.

In summary, the PICO collaboration experimentally established a new bubble nucleation model for gamma-induced bubbles in light element fluids such as C_3F_8, not favoring the traditional energy hot-spike model but instead one driven by ionization via δ-electron production (see Figure 3.6). This distinction between electron and nuclear recoil mechanisms (Seitz threshold) introduces a new degree of freedom that can be exploited to reduce the nuclear recoil threshold of bubble chamber detectors even further while simultaneously maintaining excellent electron recoil background rejection.

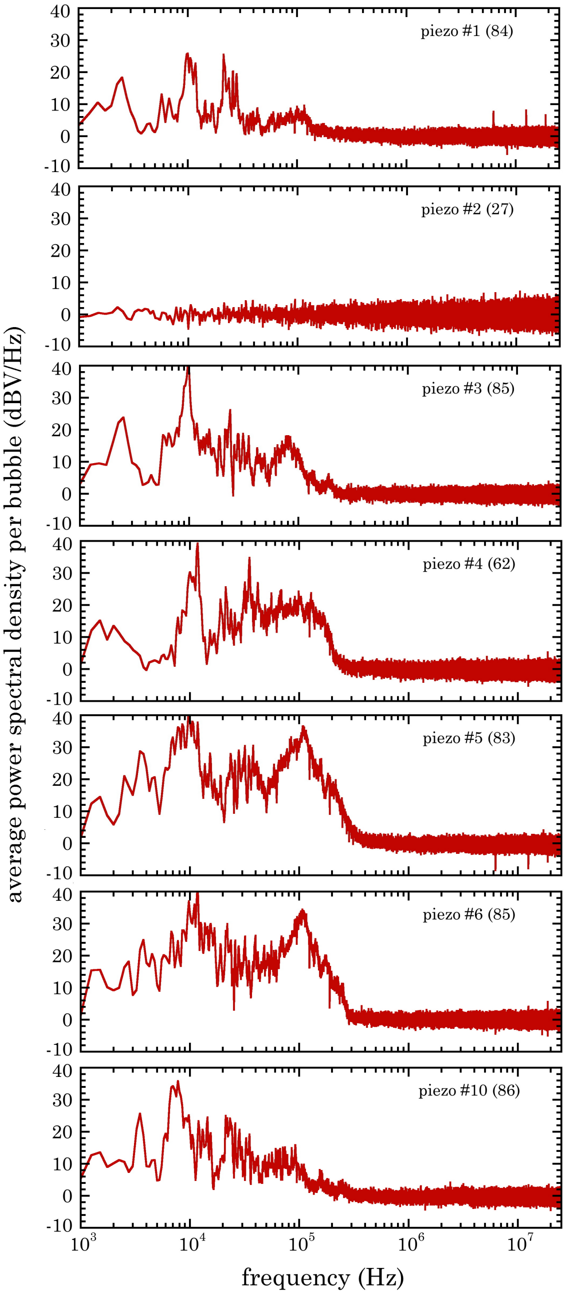

Figure 3.8: Comparative tests for acoustic response of alternative piezoelectric transducer designs in GUNTER. The tests were performed by measuring the average power over a number of electron recoil events, the quantity of which is specified in the top right corner. The design for piezo 5 stood out as providing the optimal response of all the tested designs, whereas piezo 2 proved to have the worst design. Piezo 5 was subsequently used for all remaining GUNTER calibration studies once testing was completed.

3.2 Acoustic Sensor Design

Acoustic studies using target C_3F_8 in GUNTER primarily consisted of testing seven distinct piezoelectric sensor designs and searching for possible indications of acoustic discrimination between electron and nuclear recoils. Section 2.2.2 discussed the importance of sensor design for acoustic detection systems in PICO. The conclusion drawn for studies in acoustic sensor design was that either no significant bubble emissions above $\sim$ 300 kHz are to be found, or their attenuation in liquid or interfaces occurs too rapidly to be detected (see Figure 3.8). However, GUNTER can sense a factor of $\sim$ 10 higher frequencies than what was possible in PICO-60, in turn reaching bubble sizes in the order of tens of microns. Sound interference from multiple sources (i.e., multiple bubbles) generates measurable power above 300 kHz, demonstrating that high-frequency sensitivity is in place, where high-frequency emission from single bubbles is not. Piezo 5 provided the optimal response of all the tested designs (see Figure 3.8). The collaboration intends to study this specific design further in pursuit of fabricating more sensitive radio-pure acoustic transducers (see Figure 2.21) to be used in future experiments.

3.3 Electron and Nuclear Recoil Classification

Neural networks are quite effective at solving pattern recognition problems that require classifying inputs into a set of target categories (Kim, 2010). Thus, similar to position reconstruction in GUNTER, the neural networks for acoustic discrimination were developed with Matlab's Neural Network Toolbox (NNT), specifically the Neural Pattern Recognition application (nprtool). This application offers a modular approach to selecting data, creating and training a network, and evaluating its performance using cross-entropy and confusion (error) matrices.

The input features used for training the neural networks include the coordinate outputs from the position reconstruction (see Figure 3.12) and the acoustic power across four different frequency bands (see Figure 3.13), labeled as r, z, P1, P2, P3, and P4, respectively, where $r = \sqrt{x^2 + y^2}$ is the radial distance from the center of the cylindrical fiducial volume. Before training the network, constraints on temperature and pressure are imposed on the data for optimal statistical significance of comparison studies (see Figures 3.11, 3.12). The input features are then normalized independently to the same scale (i.e. [0,1]) and used for training. Building and evaluating the networks required splitting the data into three samples: training, validation, and testing. The training samples are presented to the network during training, allowing it to adjust itself according to its error. The validation samples are used to measure network generalization and halt training when generalization becomes negligible or nil (i.e., the network stops improving). The testing samples do not affect training and thus provide an independent measure of network performance during and after training.

Additionally, the Pearson's correlation technique was used to understand the relationship between the input features used for training the network (Nettleton, 2014). The Pearson's correlation coefficient (R) measures the strength of the linear association between two continuous variables. It is mathematically defined as

$$R = \frac{\sum_i (x_i - \overline{x})(y_i - \overline{y})}{\sqrt{\sum_i (x_i - \overline{x})^2 \sum_i (y_i - \overline{y})^2}}, \tag{3.2}$$

where x_i are the first variable's samples, $y_i$the second variable's samples, $\overline{x}$ the mean of values in variable x, and $\overline{y}$ the mean of values in variable y. The input feature correlation matrix for C_3F_8 (see Figure 3.13) showed a slightly more notable degree of correlation (i.e., collinearity) in acoustic power across the different frequency bands compared to that of R-134a (see section 4.1). High correlation or multicollinearity among input features is a common problem in logistic regression analysis (Chen, 2009). In some cases, it corresponds to less 'useful' information available for effective neural network training (Ayinde, Inanc, and Zurada, 2019). Interpretations of the correlation coefficient vary notably (Schober, Boer, and Schwarte,

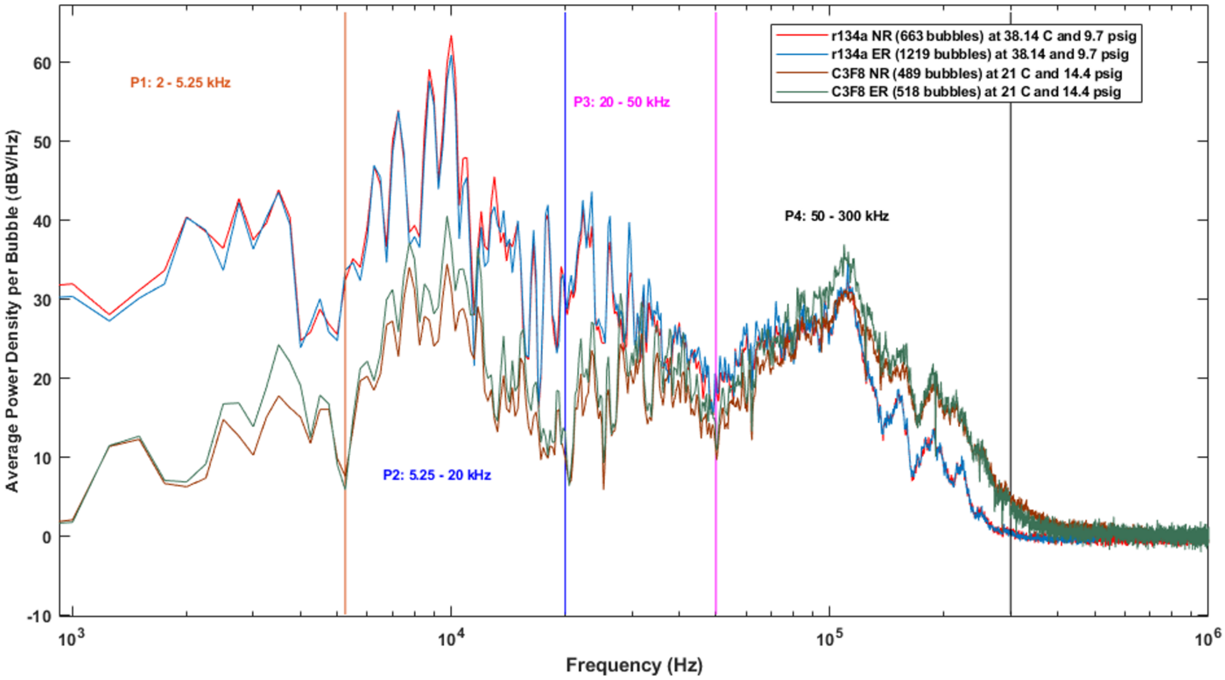

Figure 3.9: GUNTER average power density comparison of accepted events (before post-processing analysis) from electron and nuclear recoils using R-134a and C_3F_8. Acoustic emissions are partitioned across four different frequency bands as input features for the neural network. The acoustic power in each frequency band is calculated by integrating the average power density per bubble.

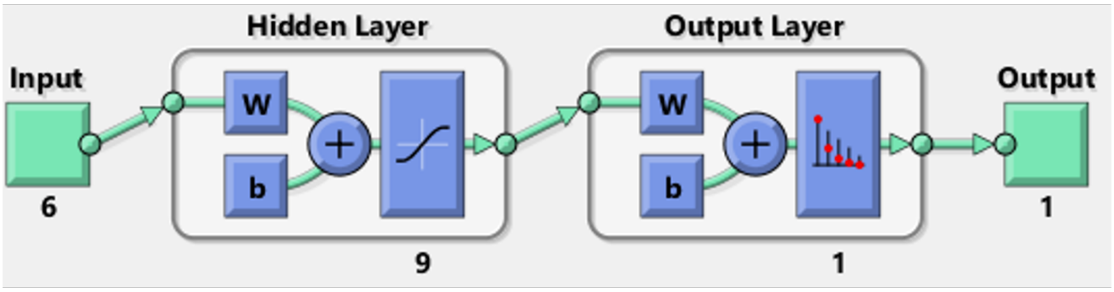

Figure 3.10: ANN architecture for acoustic classification in GUNTER. The architecture diagram highlights a two-layer feed-forward network with sigmoid hidden neurons and softmax output neurons. Vectors can be classified arbitrarily well assuming consistent data and enough neurons in the network's hidden layer. The network is trained with scaled conjugate gradient backpropagation.

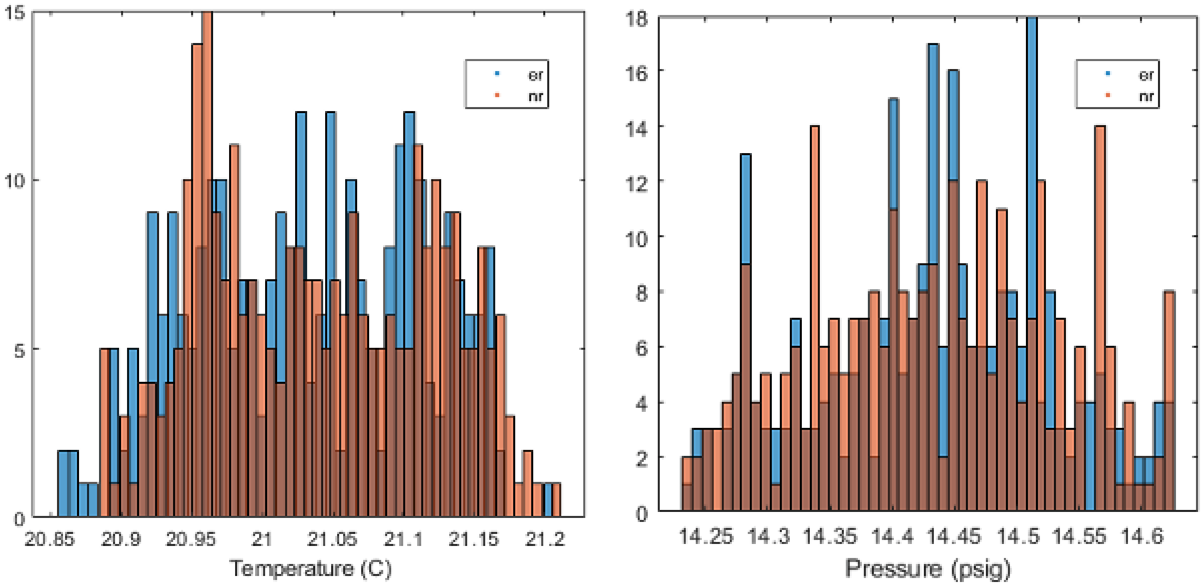

Figure 3.11: Temperature (left panel) and pressure (right panel) distributions for C_3F_8 acoustic cuts of single-bubble events used in the training of neural networks for classification of electron and nuclear recoils.

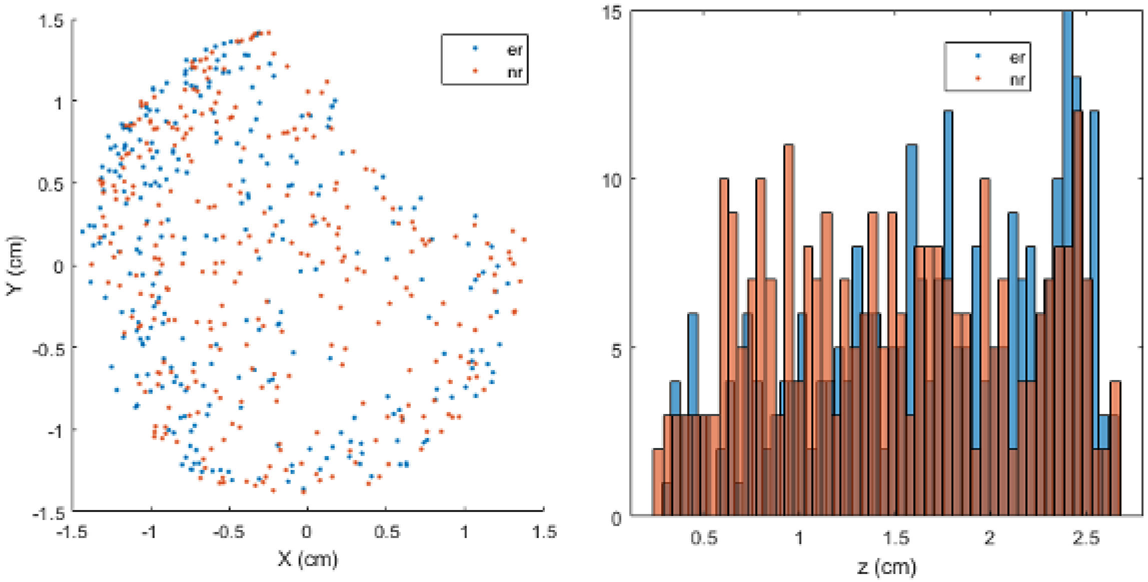

Figure 3.12: Position reconstruction of C_3F_8 acoustic cuts for electron and nuclear recoil discrimination in GUNTER. Left: x and y position reconstruction of bubble events from C_3F_8 acoustic analysis cuts. Right: Z distribution of reconstructed bubble events from C_3F_8 acoustic analysis cuts.

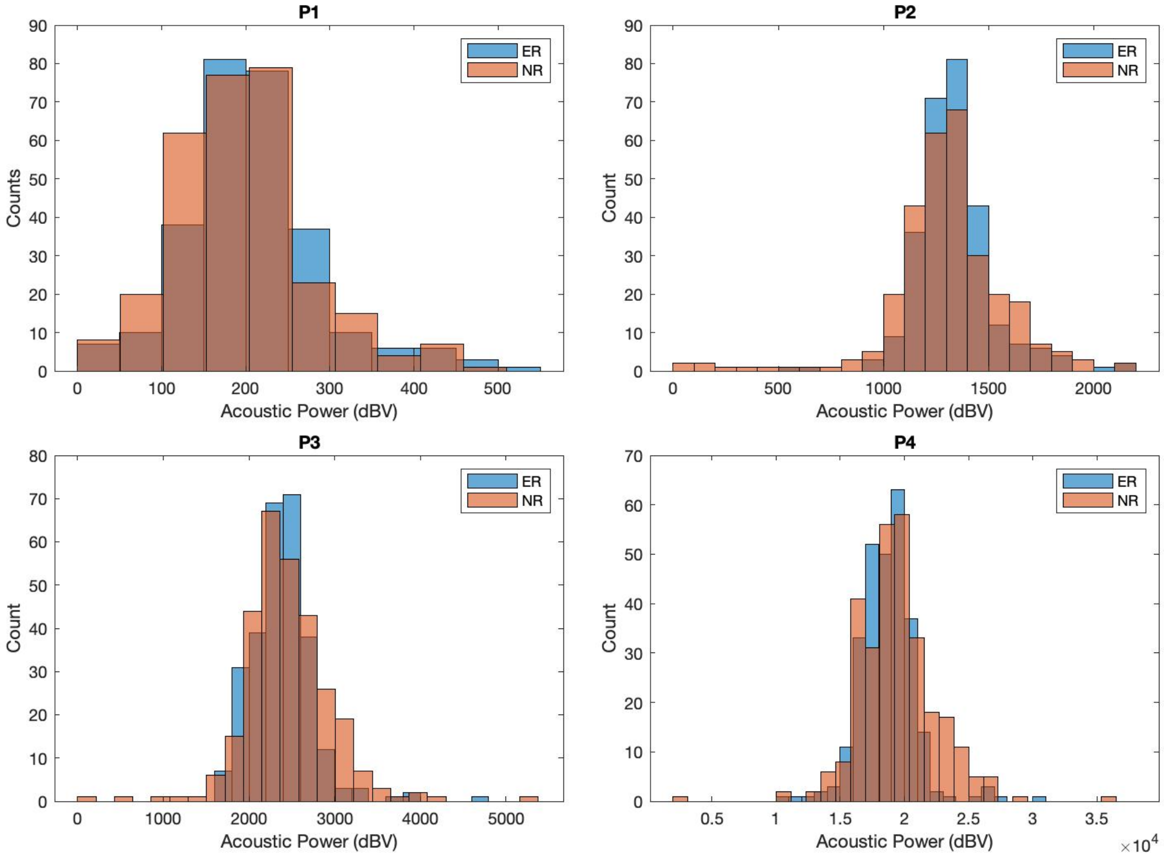

Figure 3.13: Acoustic power from electron and nuclear recoil induced bubble events in C_3F_8 across four different frequency bands.

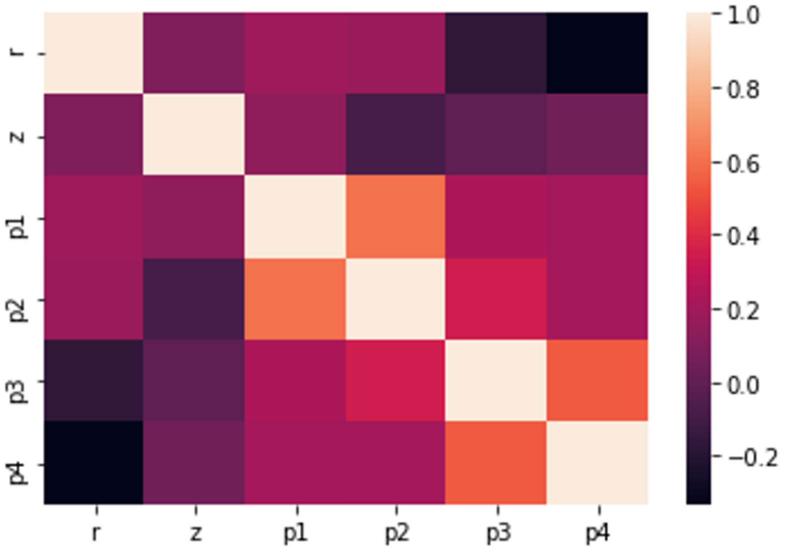

Figure 3.14: Correlation matrix for C_3F_8 acoustic classification input features.

2018). Still, it is common to see correlation coefficients of 0.65 be interpreted as moderate to good correlations, depending on what rule of thumb is applied. However, it is worth noting that a broader range of values tends to show a higher correlation than a smaller range. For future use of neural networks to classify the acoustic output of electron and nuclear recoils across different frequency bands, the author suggests exploring feature clustering solutions (Tolosi and Lengauer, 2011) to investigate classification bias with correlated features that may be degrading classification performance.

Physical considerations were made in the interpretation of acoustic differences. Training inputs that do not generate acoustic differences between electron and nuclear recoils were disregarded to avoid locking in on slight differences that could produce networks prone to overfitting. Position reconstruction information r and z were observed to contribute minimally to effective neural network training compared to acoustic power across different frequency bands. An argument of scale was made to explain the weaker network response to position reconstruction input features. Position reconstruction could, in theory, be more useful for electron and nuclear recoil discrimination studies in larger chambers, given the broader spatial range over which bubbles are triggered. However, the counterargument is

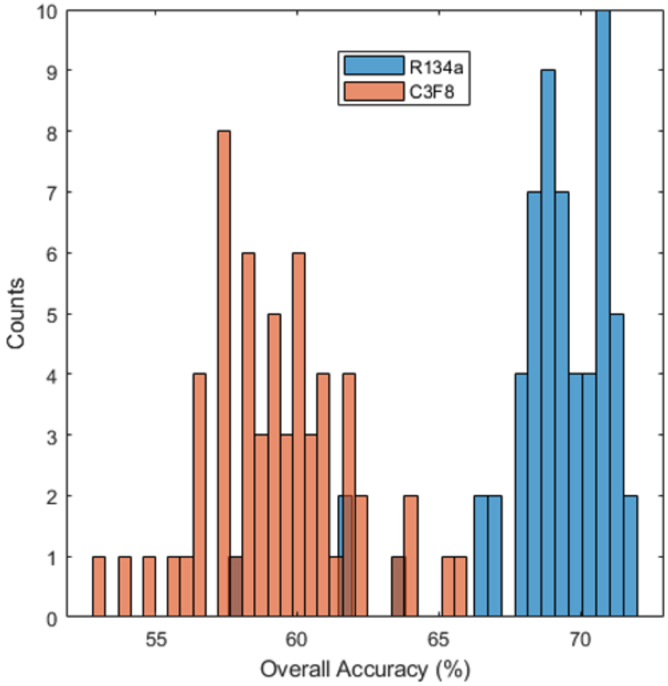

Figure 3.15: Overall accuracy histogram of electron and nuclear recoil acoustic discrimination in C_3F_8(277 ERs, 296 NRs) and R-134a (320 ERs, 191 NRs) for 60 networks trained (for each target).

that acoustic signals in larger chambers must travel longer distances before being detected. In short, if there are subtle distinctions between the acoustic output of electron recoils and nuclear recoils in C_3F_8 that a neural network can perceive, they are expected to be more difficult to exploit in larger chambers.

The overall accuracy or recognition rate (sensitivity) of the neural network is used to measure how often the classifier is correct. It is defined as the sum of the number of correctly classified values divided by the total number of values, typically written as

$$\frac{T_P + T_N}{T_{total}}, \tag{3.3}$$

where T_P is the number of true positives, T_N the number of true negatives, and T_{total} the total number of values. The average overall accuracy was measured by quantities of overall accuracy for many network training iterations, each with its own random sampling

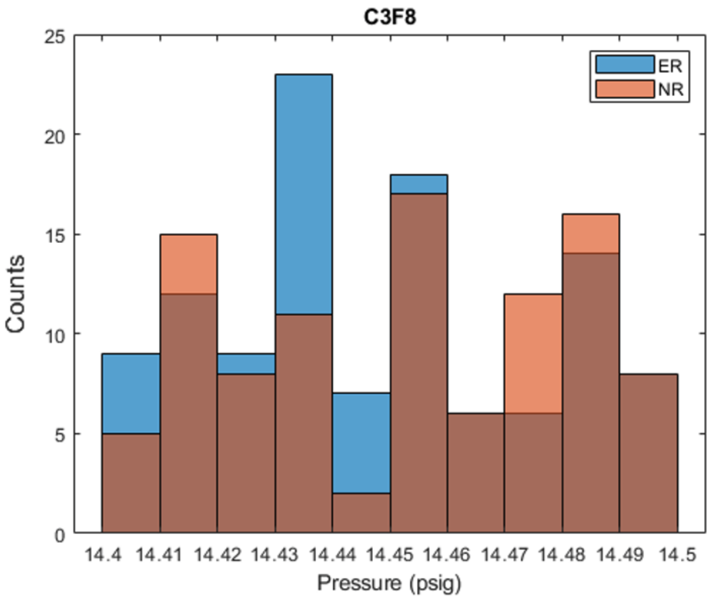

Figure 3.16: Pressure distribution for electron and nuclear recoil events within 0.1 psig of each other.

for training, testing, and validation. No significant indications of acoustic discrimination between electron and nuclear recoils were found in GUNTER C_3F_8 calibration data. For a total of 60 networks trained, the average overall accuracy was 59.3% (see Figure 3.15), not much better than a random coin flip for classifying two possible cases. Imposing even stricter bounds on pressure, within 0.1 psig (see Figure 3.16), resulted in roughly the same average overall accuracy of classification between electron and nuclear recoils in C_3F_8 (see Figure 3.17).

Understanding the patterns detected by neural networks is non-trivial. One way of studying these patterns is through sensitivity analysis (Fu and Chen, 1993). A simple but effective method to study them is to read out the neural network output from unit vectors (i.e., a one at a single input neuron while keeping the rest of the inputs as zeroes). This method is known to miss many cross-correlations (Diamantaras and Kung, 1994) but sheds light on perceived distinctions for classification purposes. The magnitude of the output, relative to all others, sheds light on the importance of the neural weights for each feature input.

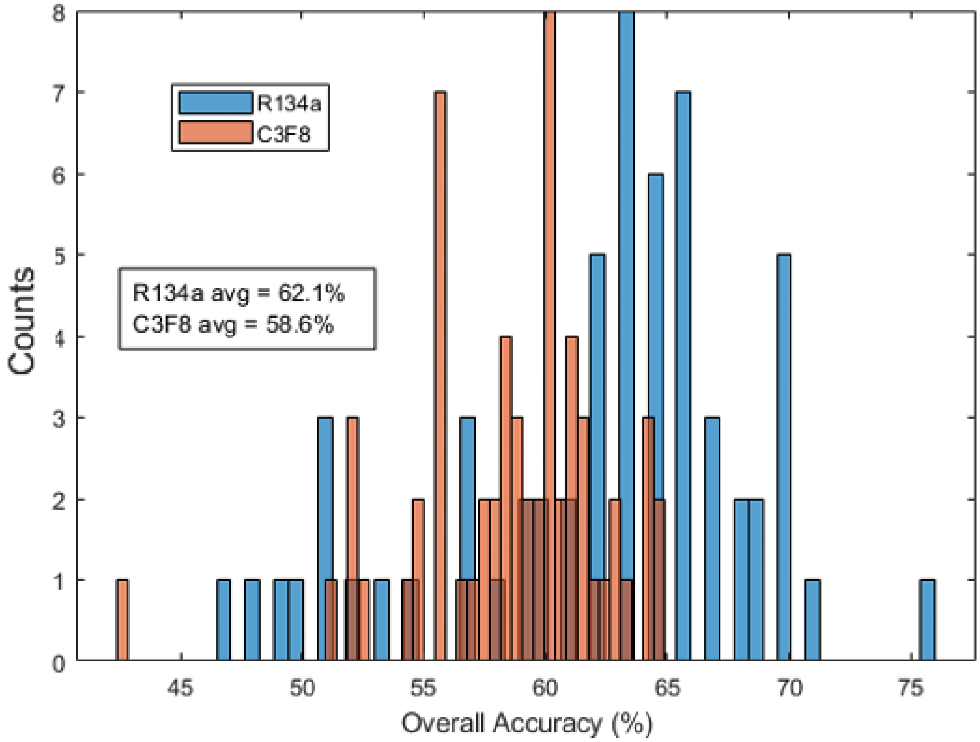

Figure 3.17: Overall accuracy histogram of electron and nuclear recoil acoustic discrimination in C_3F_8(112 ERs, 99 NRs) and R-134a (44 ERs, 46 NRs) for stricter bounds on pressure, based on 60 networks trained (for each target).

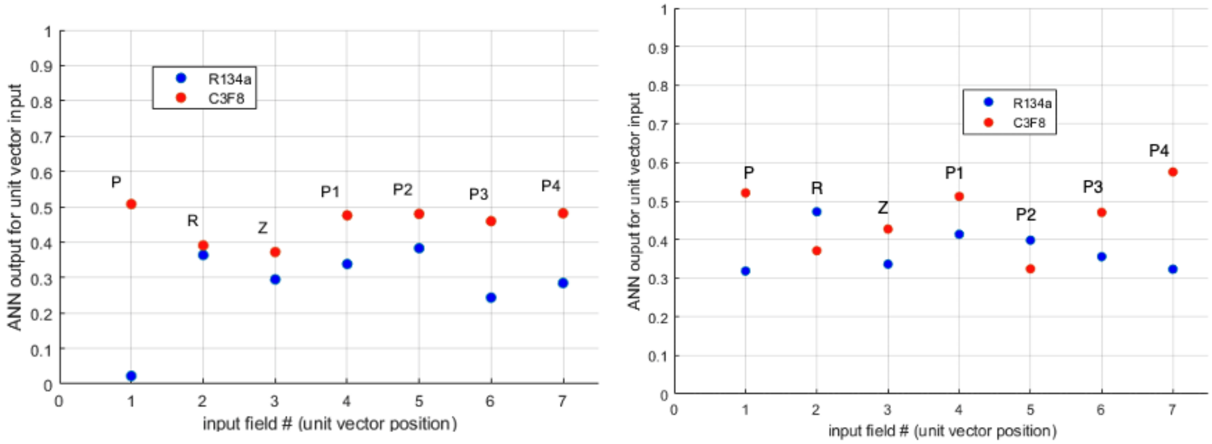

Figure 3.18: ANN output for unit vector inputs. Left: C_3F_8 (465 ERs, 597 NRs) and R-134a (1003 ERs, 363 NRs) for samples within 1 psig. The ANN output for pressure as unit vector input overshoots in its response, showing a strong bias toward electron recoils for larger pressures. Right: C_3F_8 (277 ERs, 296 NRs) and R-134a (44 ERs, 46 NRs) for samples within 0.1 psig. The strong bias for electron recoils at larger pressures is strongly mitigated after implementing stricter bounds on pressure for accepted events.

A sensitivity demonstration was conducted with C_3F_8 and R-134a, wherein pressure was included as an input. The input features for comparable relaxed and strict constraints on pressure were used to test the neural network output with unit vectors as just described (see Figure 3.18). The findings confirmed that using pressure with relaxed constraints lent itself to overfitting (see Figure 3.18, left panel) when pressure stability is not ideal, as with R-134a (see Figure 4.4). For samples within 1 psig, larger pressures showed a bias for electron recoils in R-134a. In contrast, implementing strict bounds on pressure mitigated this effect (see Figure 3.18, right panel). No overshoot in response to input vectors was observed in C_3F_8 for relaxed constraints, which was expected given excellent temperature and pressure stability for comparison purposes (see Figure 3.11). This discussion continues in Section 4.2 and is folded into the electron and nuclear recoil classification studies in R-134a.

CHAPTER 4

R-134A STUDIES

The most favored hydrogen-rich target within the collaboration is R-134a ($C_2H_2F_4$). This industrial refrigerant is relatively cheap ($12 per kg), non-flammable, and non-toxic, offering many advantages favored for operation in underground facilities. The physics reach of R-134a in bubble chambers for low-mass dark matter searches has been reviewed by PICO collaborators (Seth et al., 2019) and was discussed in Chapter 2 as part of the motivation behind the GUNTER calibration chamber. Recall from Section 2.1 that hydrogen is the most sensitive target for low-mass nuclear recoils since it maximizes kinetic sensitivity (see Figure 4.2).

GUNTER required a few minor upgrades and modifications for R-134a operation after completing its C_3F_8 goals. The fluoropolymer elastomer and synthetic rubber compound Viton worked well with C_3F_8 but was fundamentally incompatible with R-134a. Evidence of this was the rupture of the Viton seat within minutes of exposure. The next elastomer tested was Butyl, but it was barely an improvement. Finally, the elastomer Neoprene W was found to work well with R-134a and used for subsequent runs. A switch to R-134a in PICO-40L for low-mass runs will require a thorough screening of all elastomers. Other notable chamber upgrades included a simplified cooling design that works well to -20°C and a smaller inner vessel diameter (see Appendix B).

The MCNP input files for GUNTER simulations using ^{88}Y/Be (see Figure 4.1) and ^{22}Na are included in Appendix C. The activity of ^{88}Y/Be was measured to be 0.73 mCi on 8/28/17. Using this information, it was possible to use the dates each data point was taken to correct for source decay in post-processing the simulation output. For simulation purposes, ^{22}Na was treated as a point source, whereas the complex geometry of the photo-neutron source ^{88}Y/Be is well defined in simulation (see Figures 2.2, 2.3).

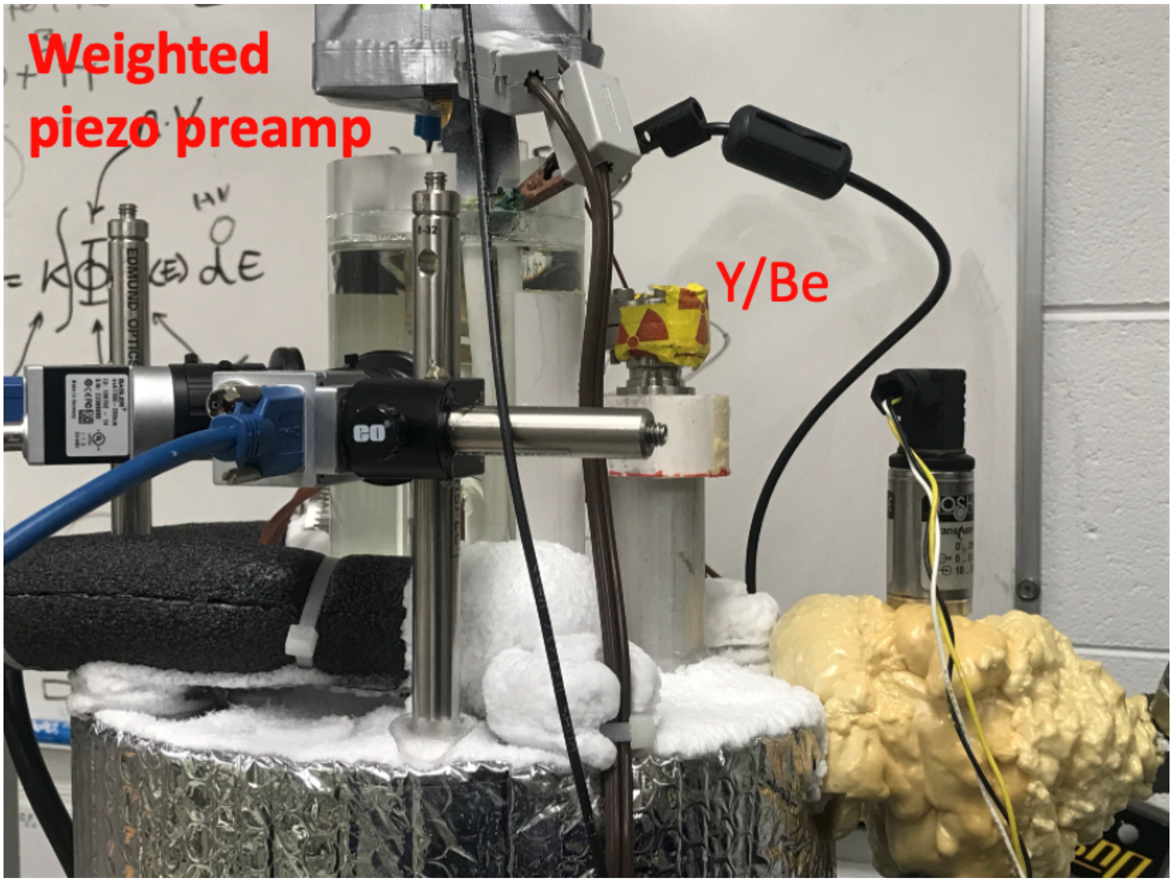

Figure 4.1: GUNTER during R-134a operation using an ^{88}Y/Be source. The weighted piezo preamp (2 lbs for good acoustic coupling) can be seen on top.

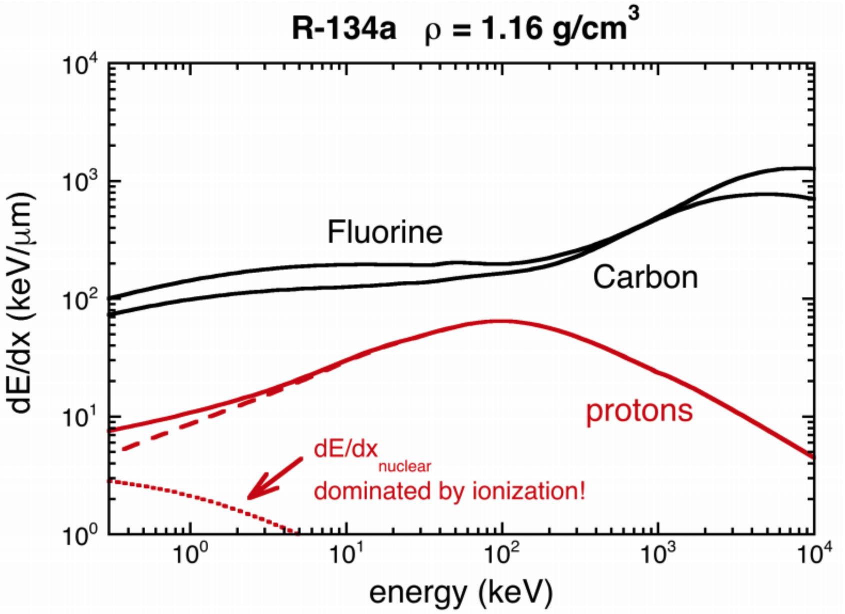

Figure 4.2: Instantaneous stopping power (dE/dx) versus energy for carbon, fluorine, and proton recoils in R-134a. Assuming the traditional Seitz threshold for nuclear and proton recoils, only particles in the thermodinamically-defined quadrants can produce bubbles, by surpassing minimum energy and dE/dx thresholds.

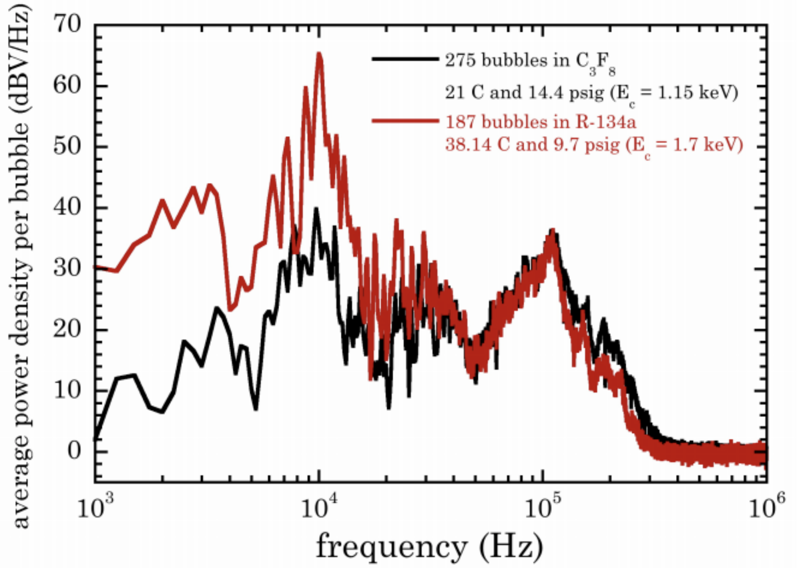

Figure 4.3: GUNTER acoustic output comparison of electron recoils in R-134a and C_3F_8. A first-look at R-134a showed a stronger response to that of C_3F_8 at lower frequencies for electron recoils.

4.1 Acoustic Response

Sections 2.1 and 2.2 discussed the role of acoustic information in identifying alpha-induced bubbles in PICO targets and the information that survives into the acoustic signal. Electron recoils and proton (hydrogen nuclei) recoils are expected to have longer proto-bubble nucleation tracks than those from nuclear recoils from fluorine and carbon, indicating the possibility of effective methods for acoustic gamma rejection or proton tagging. Recall that higher frequencies correspond to earlier stages in the growth of a bubble (Levi et al., 1978). PICO collaborators have used molecular dynamic simulations of proto-bubble growth acoustics to confirm that particles with a relatively low stopping power favor high-frequency emissions (Kozynets, Fallows, and Krauss, 2019). This trend was also observed in PICO-60 acoustic data. It is hypothesized that longer proton track lengths could enhance lower frequency signals as well. As was emphasized in Sections 2.1 and 2.2, access to higher frequencies and enhanced sensitivity at lower frequencies via upgrades to bubble chamber acoustics is expected to provide additional acoustic information, potentially paving the way to electron and proton recoil identification.

The acoustic response to electron and nuclear recoils in R-134a was measured for the first time using GUNTER data. Electron recoil calibrations allowed for a direct single bubble acoustic output comparison of R-134a and C_3F_8. Acoustic emissions from R-134a were observed to be notably ‘louder’ for comparable energy thresholds, and otherwise, near-identical operating conditions. The most notable response difference to C_3F_8 acoustic output was observed at lower frequencies (see Figure 4.3).

4.2 Electron and Nuclear Recoil Classification

GUNTER was operated with R-134a at 10 psig and 38.25°C for long electron and nuclear recoil runs using ^{22}Na and ^{88}Y/Be, respectively, with the ultimate goal of using electron

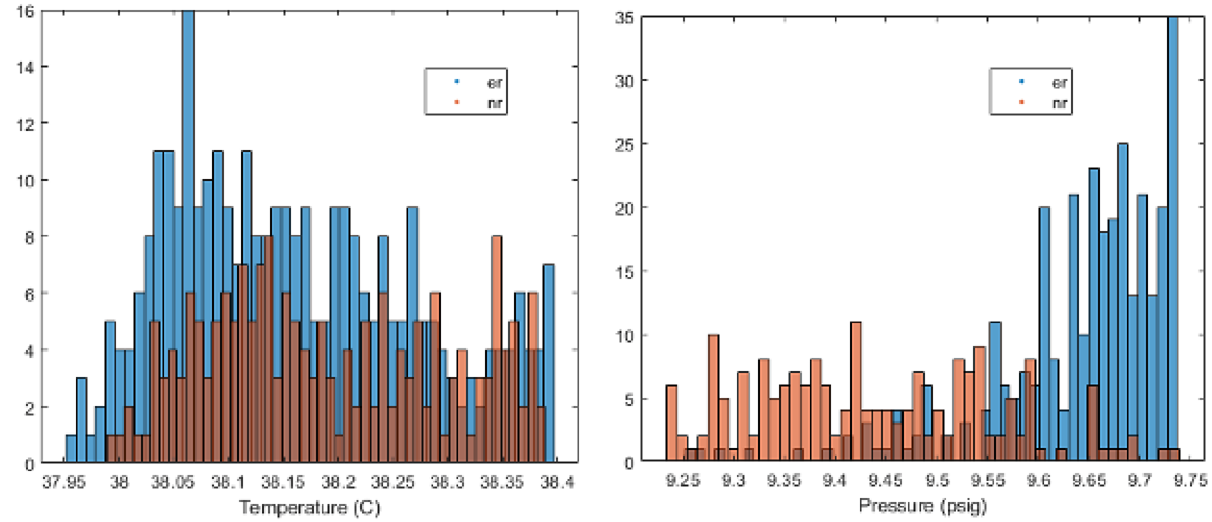

Figure 4.4: Temperature and pressure distributions for R-134a acoustic cuts of single-bubble events used in the training of neural networks for classification of electron and nuclear recoils.

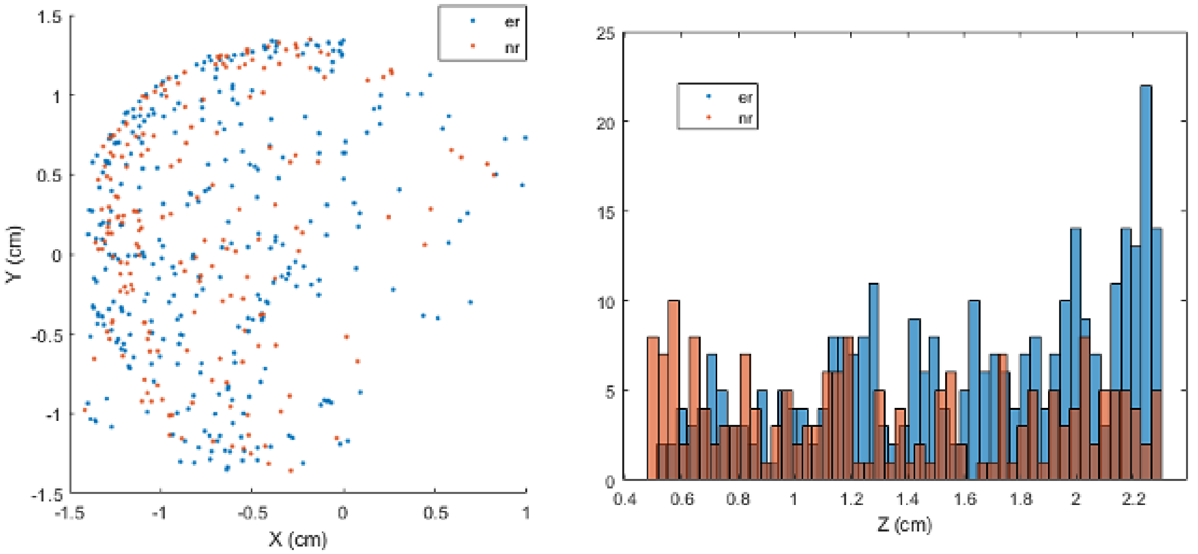

Figure 4.5: Position reconstruction of R-134a acoustic cuts for electron and nuclear recoil discrimination in GUNTER. Left: x and y position reconstruction of bubble events from C_3F_8 acoustic analysis cuts. Right: Z distribution of reconstructed bubble events from C_3F_8 acoustic analysis cuts.

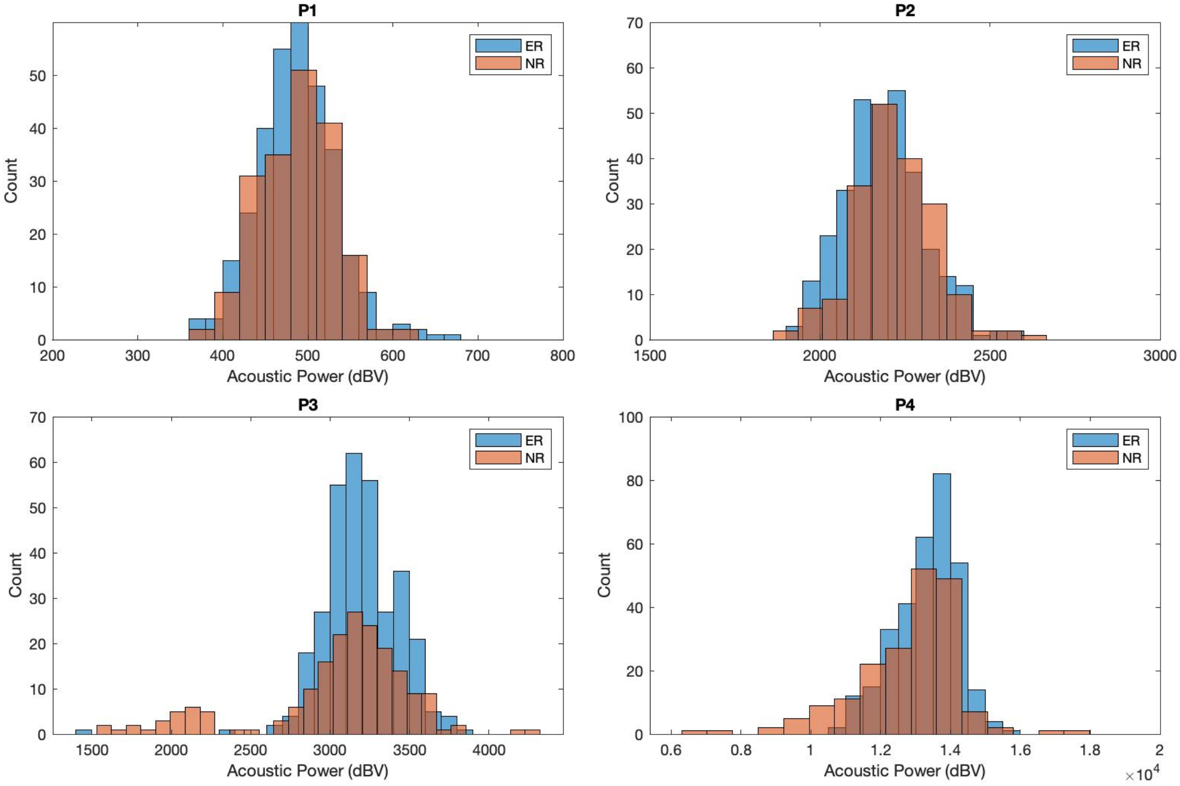

Figure 4.6: Acoustic power from electron and nuclear recoil induced bubble events in R-134a across four different frequency bands.

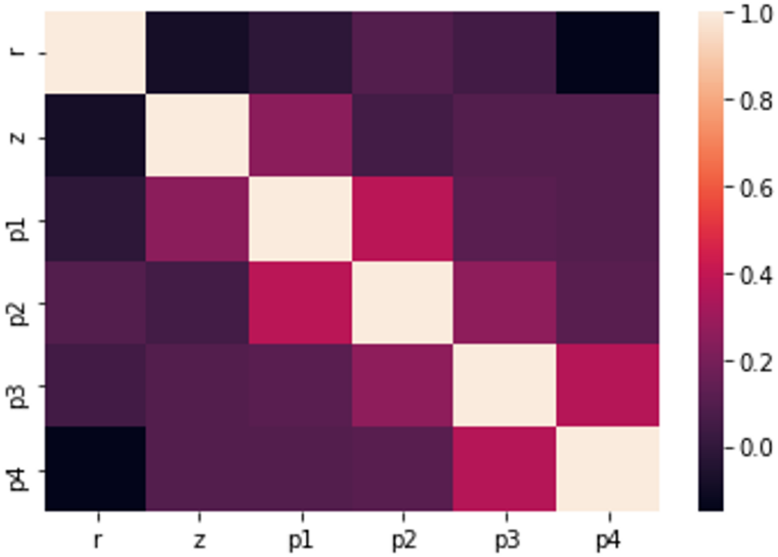

Figure 4.7: Correlation matrix for R-134a acoustic classification input features.

recoils runs to provide an acoustic template to compare with nuclear recoils and eventually inform possible proton recoil discrimination. The analysis is very similar to that of C_3F_8, discussed in Section 3.3.

R-134a runs did not benefit from the same pressure stability as C_3F_8 (see Figures 3.11 and 4.4). Despite this issue, it was particularly significant not to relax the constraints on pressure for accepted events by too much since the intensity of acoustic emission goes with the cube of the operating pressure in the form of $(P - P_0)^3$, where P_0 is the operating pressure and P is the local pressure at the boundary of the expanding bubble (Martynyuk, Smirnova, and Wood, 1991). Given the nature of this dependency, the relaxing of constraints on pressure for electron and nuclear recoil cuts in R-134a were expected to substantially increase the overall accuracy of the classification neural network by way of overfitting (modeling error) (see Figure 3.18). For a total of 60 networks trained for events within 0.5 psig of each other, the average overall accuracy was 68.9% (see Figure 3.15), slightly better than that of C_3F_8 but not particularly significant for adequate classification.

Applying even stricter bounds on pressure (within 0.1 psig) led to an average overall

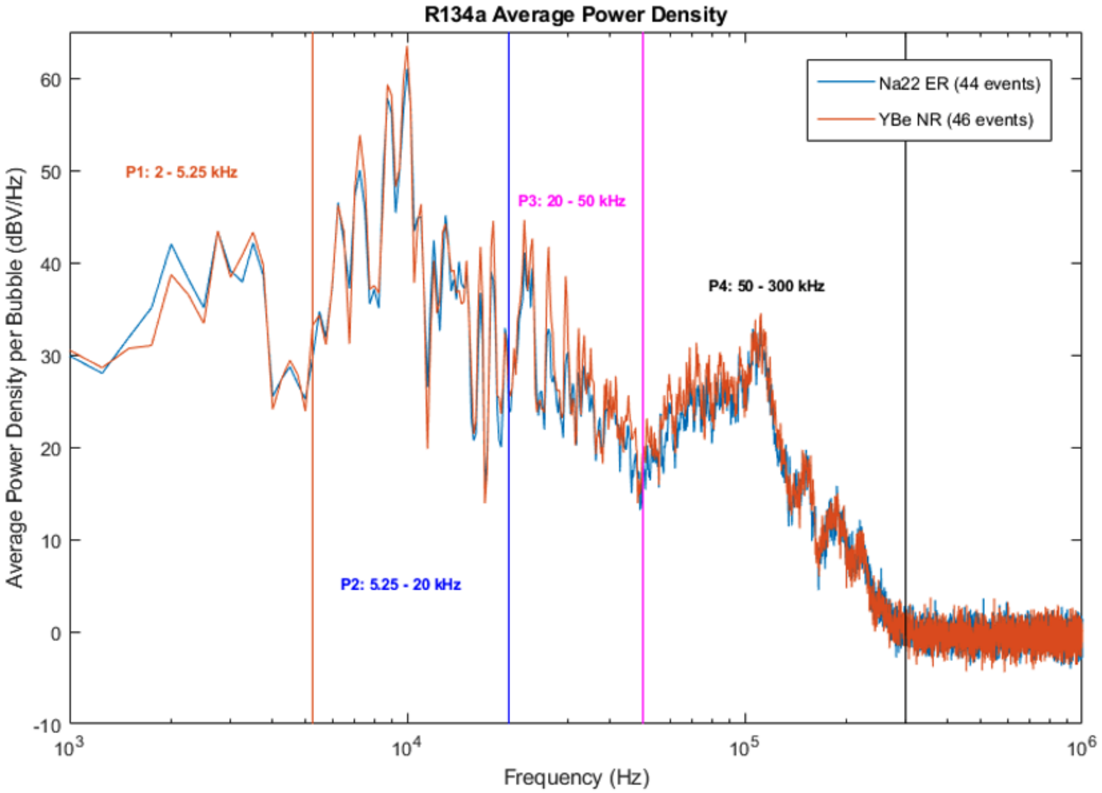

Figure 4.8: Average power density per bubble of well-constrained electron and nuclear recoils in R-134a.

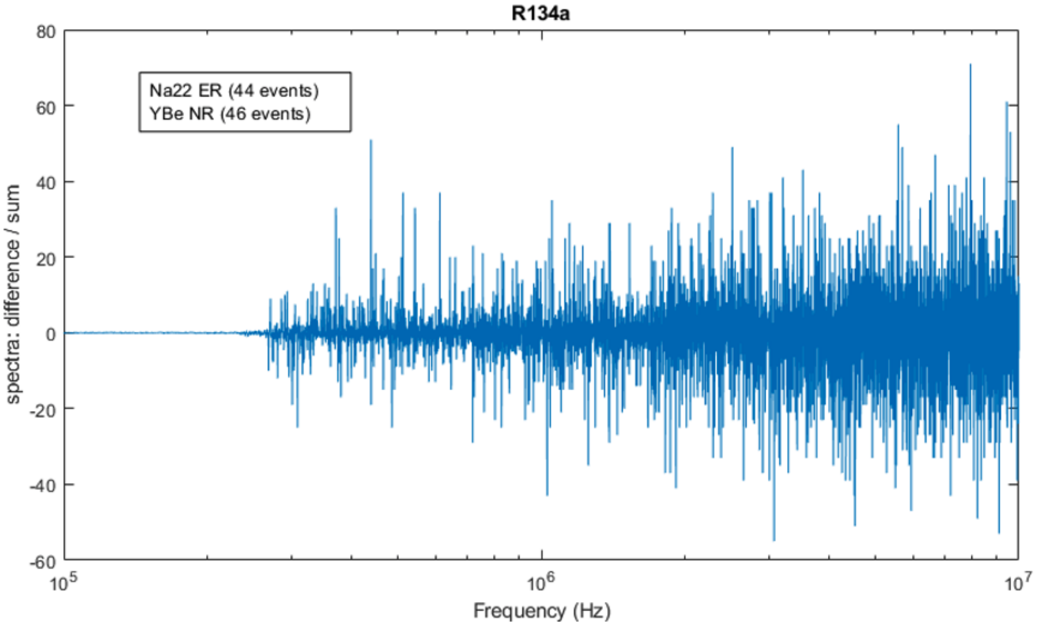

Figure 4.9: Ratio of average spectral difference and its sum for well-constrained electron and nuclear recoils in R-134a

accuracy of 62.1% (see Figure 3.17). For such a small and well-constrain number of events, the author argues that there are acoustic differences yet to be exploited with neural networks in R-134a (see Figures 4.8 and 4.9). Consider that applying those same strict bounds on C_3F_8 (see Figure 3.16), with roughly four times the number of events, fell short of significantly improving the average overall accuracy for acoustic classification (see Figure 3.17). The stronger acoustic response observed in R-134a from recoils at lower frequencies and lesser correlated acoustic power input features than those of C_3F_8 suggests that there may be more available acoustic differences to exploit in R-134a. Recall that alphas have been inferred through acoustic observations by PICO before (see Section 2.1). Increased sensitivity via upgrades in acoustic sensor technology and design and access to more significant amounts of quality calibration data could further probe these intrinsic acoustic differences.

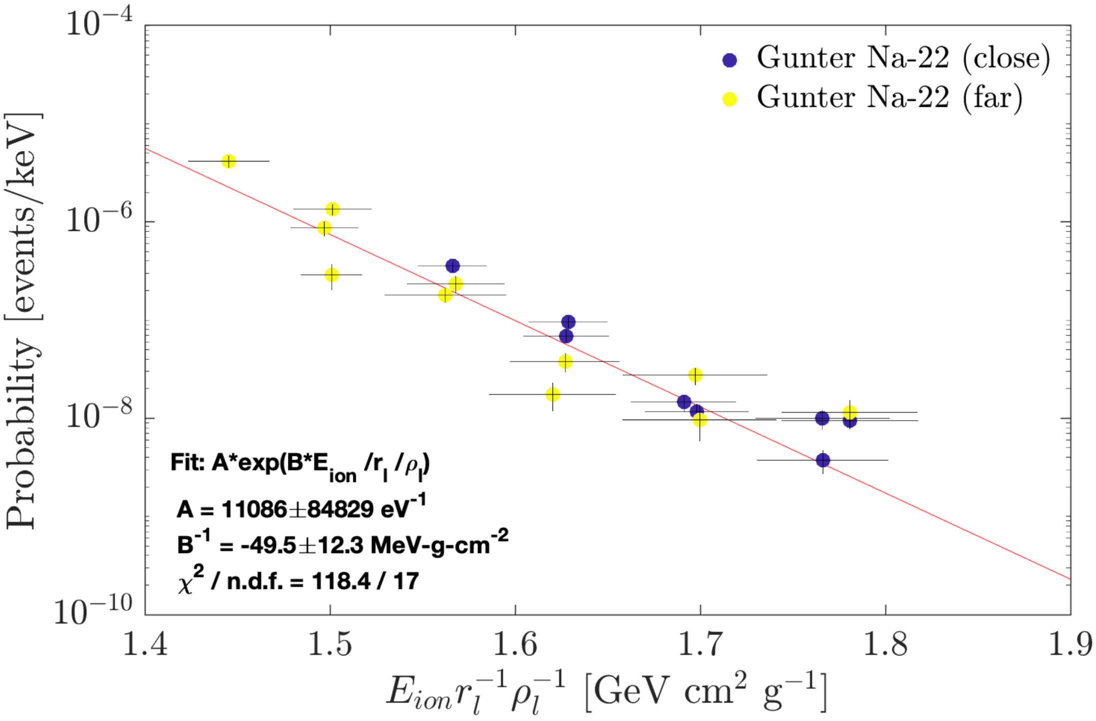

Figure 4.10: Probability of bubble nucleation per keV of energy deposited by electron recoils as a function of stopping power assuming an ionization energy threshold in R-134a using ^{22}Na. The labels “close” and “far” in the legend refer to the position of the source relative to the active volume during that run. The position of the source was adjusted accordingly for simulation purposes (see Appendix C). Figure courtesy D. Baxter (private communication).

4.3 Response Parameters

4.3.1 Electron Recoil Mechanism

To define the parameters of the ionization threshold model for electron recoil response (see section 2.1.1) in R-134a, GUNTER was operated at different pressures and temperatures using ^{22}Na as the radioactive source for gamma-induced electron recoils. For simulation purposes, ^{22}Na was considered as a point source (see Appendix C). Data were collected with the source at two different distances from the fiducial volume. The ultimate goal of this experiment was to inform the operating conditions that simultaneously minimize threshold and sensitivity to electron recoils in R-134a. Based on GUNTER C_3F_8 data, of which there is

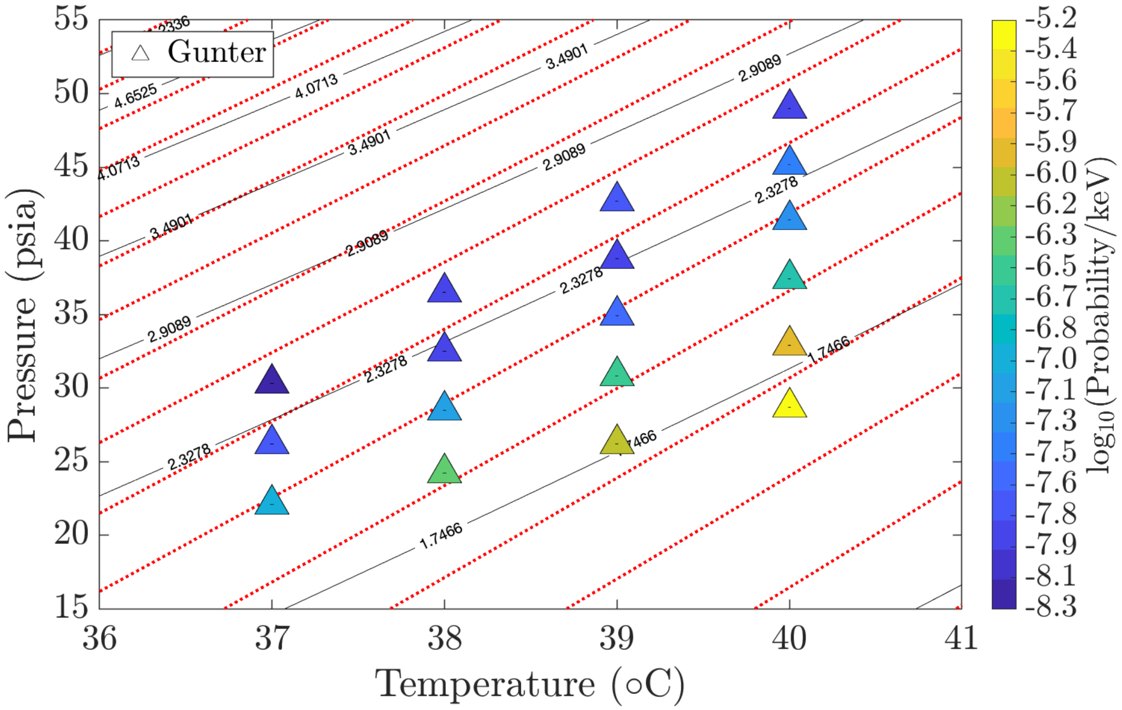

Figure 4.11: Probability of nucleation per unit of energy deposited for multiple pressure and temperature combinations in R-134a. The lines of constant Seitz threshold (nuclear recoil threshold) are shown in black, with listed values in units of keV. The lines of constant stopping power using an ionization energy threshold are shown in dotted red. Figure courtesy D. Baxter (private communication).

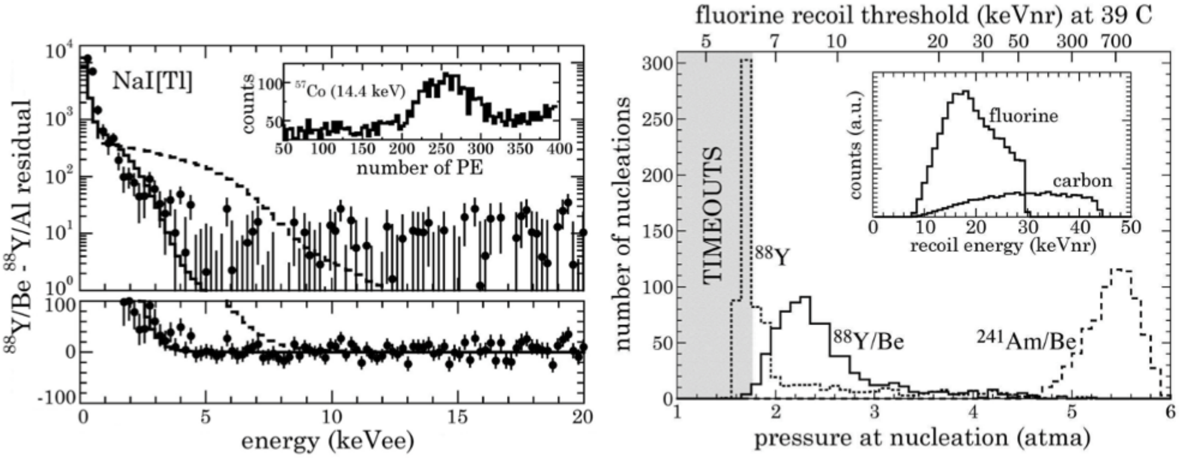

Figure 4.12: ^{88}Y/Be photo-neutron calibration source applications. Left: Response measurement of NaI[Tl] to low-energy nuclear recoils produced using an ^{88}Y/Be source. Right: response measurement of superheated CF_3I to neutrons emitted from ^{241}Am/Be and ^{88}Y/Be. The inset figure shows the distribution of simulated ^{88}Y/Be nuclear recoil energies explored via decompression. Figures from Collar (2017).

a more considerable amount, the fundamental constant (see Equation 3.1) was expected to be 55.5 ± 3 compared to the best fit 49.5 ± 12.3. Similar to C_3F_8 (see Figure 3.6), the bubble nucleation probability was observed to follow an exponential decay with a fundamental constant depending on the attenuation of a threshold-energy photon (see Figure 4.10). The probability of nucleation per keV of deposited energy for GUNTER R-134a calibration data is shown in Figure 4.11. These results will be critical references for low-mass PICO-40 operation and a planned publication from the PICO collaboration on the studies involving hydrogen-rich target R-134a.

4.3.2 Neutron Calibration and Threshold Model

Low-energy monochromatic neutron emission from an ^{88}Y/Be source was exploited using R-134a to mimic the few keVnr recoils in GUNTER expected from low-mass WIMPs. This new and convenient calibration method was recently demonstrated using a NaI[Tl] target for confirmation (Collar, 2017), illustrating its application for other target materials such as superheated and noble liquids as well (see Figure 4.12). For pressures below 45 psig, an

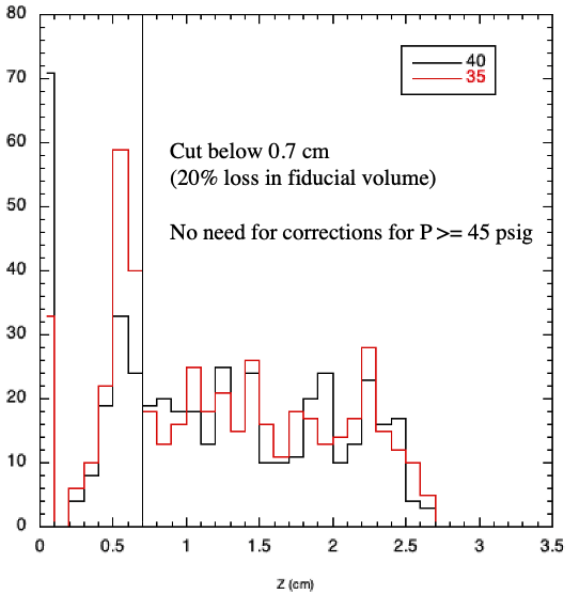

Figure 4.13: Fiducial volume artifacts due to reflections. A cut below 0.7 cm corresponds to a 20% loss in fiducial volume.

excess of artifacts due to reflections was observed below 0.7 cm, accounting for a 20% loss in fiducial volume (see Figure 4.13). For consistency, this cut below 0.7 cm was applied to all data points and adjusted for in simulation.

The calibration results are shown in Figure 4.14. Right off the bat, one can notice that even the best possible case scenario considered from simulation falls short of explaining the rates observed at the lowest threshold energies. A critical inference drawn from this exercise is the importance of accounting for proton recoils to describe the observed bubble nucleation rates effectively. For increasing Seitz thresholds (e.g., increasing pressure at a fixed temperature), proton recoils begin to vanish as they move through what is informally referred to as the transition regime and become less likely to produce bubble nucleations. This transition naturally culminates in the vanishing of proton recoils altogether. Recall that their stopping power is notably smaller than those of carbon and fluorine recoils (see Figure 4.2), so much so that for many combinations of pressure and temperature, proton recoils are unable to produce bubble nucleations (i.e., the stopping power threshold is never surpassed

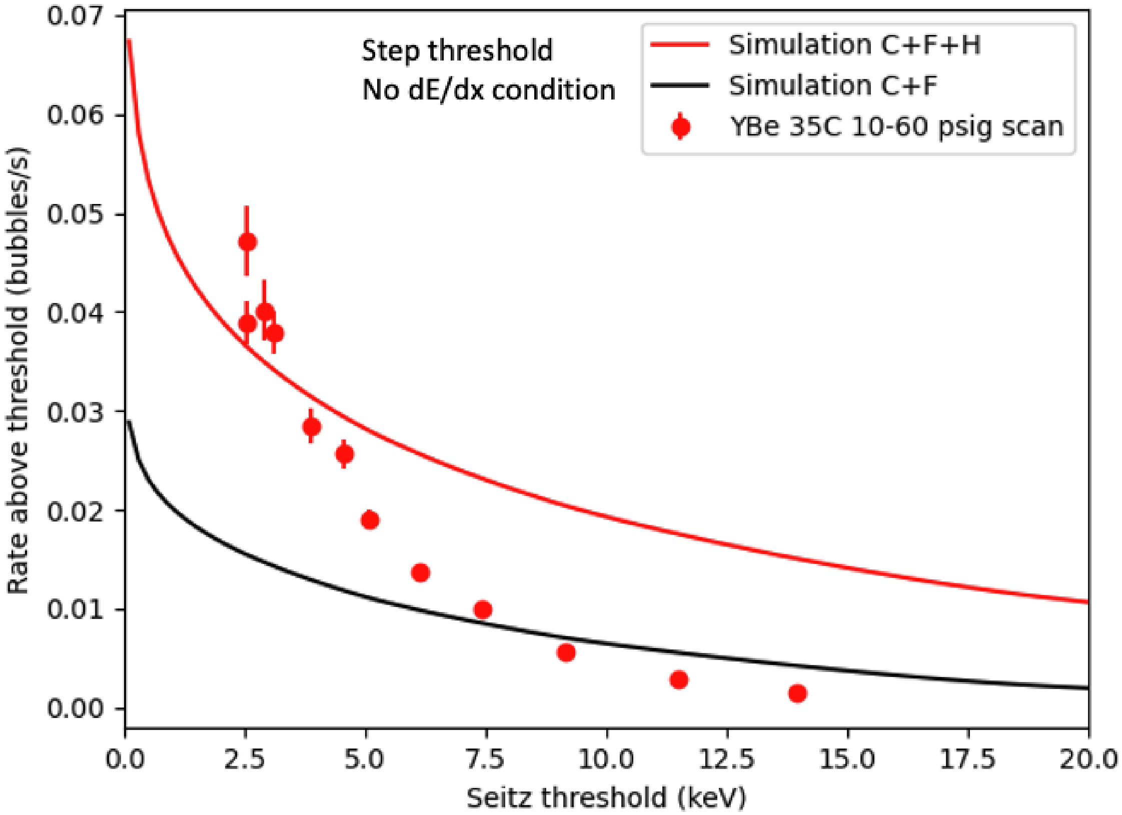

Figure 4.14: ^{88}Y/Be 10-60 psig pressure scan at 35°C for GUNTER R-134a calibration. The smooth lines represent the rate above step threshold with no dE/dx nucleation condition with the consideration of proton recoils (red) and the exclusion of those same recoils (black).

for any recoil energy).

A robust analysis program was developed for simulating bubble nucleation rates in GUNTER using R-134a and a ^{88}Y/Be photo-neutron source with the ultimate goal of finding the best fit which describes its response parameters. It employs all the thermodynamic properties described in Section 1.3 to calculate the Seitz threshold and minimum stopping power required for any combination of pressure, temperature, and Harper factor (See Figures 4.15 and 4.16). Previous PICO efforts to characterize the softness of threshold for recoiling species in C_3F_8 have relied on computationally intensive methods, notably the use of piecewise linear functions with energies as free parameters and most recently, MCMC methods for likelihood function maximization to obtain the best-fit efficiency curves from PICO-60

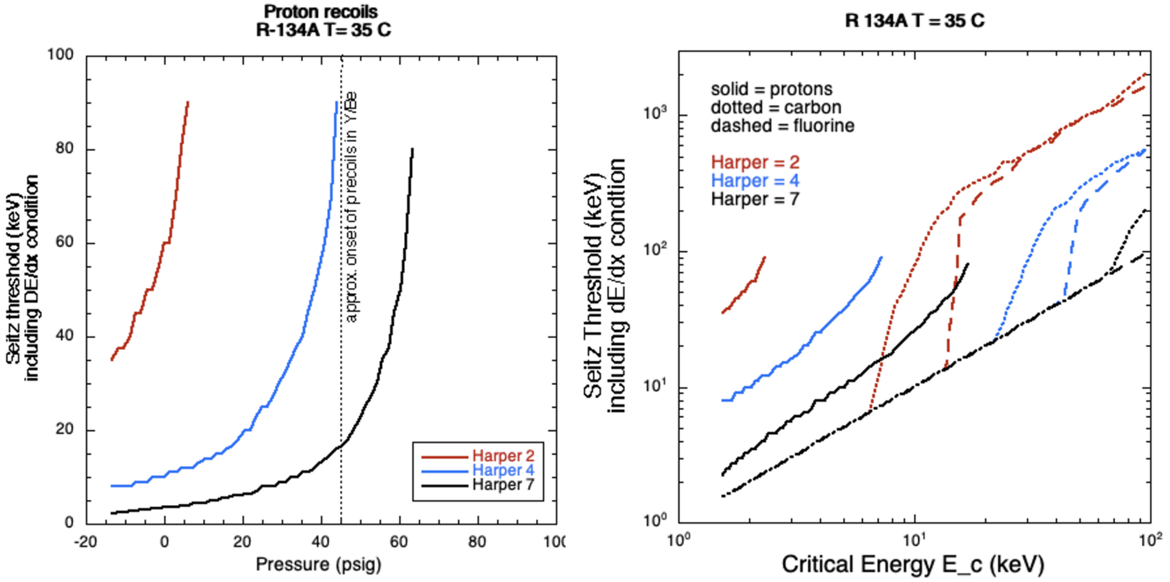

Figure 4.15: Seitz threshold calculation in R-134a for different Harper factors. Left: Seitz threshold with dE/dx condition of proton recoils in R-134a for different Harper factors. A line is included at 45 psig, where we expect the approximate onset of proton recoils in ^{88}YBe to occur (see Figure 4.14). Right: Seitz threshold with dE/dx condition for proton, carbon, and fluorine recoils at different critical energies for multiple Harper factors.

data (see Figure 4.15).

Intuitively and for simplicity, a linear threshold model was approximated for bubble nucleation efficiency using the traditional Seitz threshold formulation discussed in Section 1.3. In the simplest case, GUNTER data were used to constrain two free parameters, Harper factor and softness of threshold (see Figure 4.17). The latter is some energy above the Seitz threshold where bubble nucleation has yet to reach total efficiency. A basic diagram of the linear threshold model for bubble nucleation is shown in Figure 4.16. The program begins by initializing all the necessary variables and functions and calculates the bubble nucleation energy thresholds for each recoiling species, in the case of R-134a, carbon, fluorine, and hydrogen. Lastly, the program scans the MCNP-PoliMi output for energy depositions originating from each recoiling species to determine if bubble nucleation occurred based on the threshold model being tested. For each data point, the bubble nucleations of each recoiling species are then tallied and used to calculate the nucleation rate in bubbles per

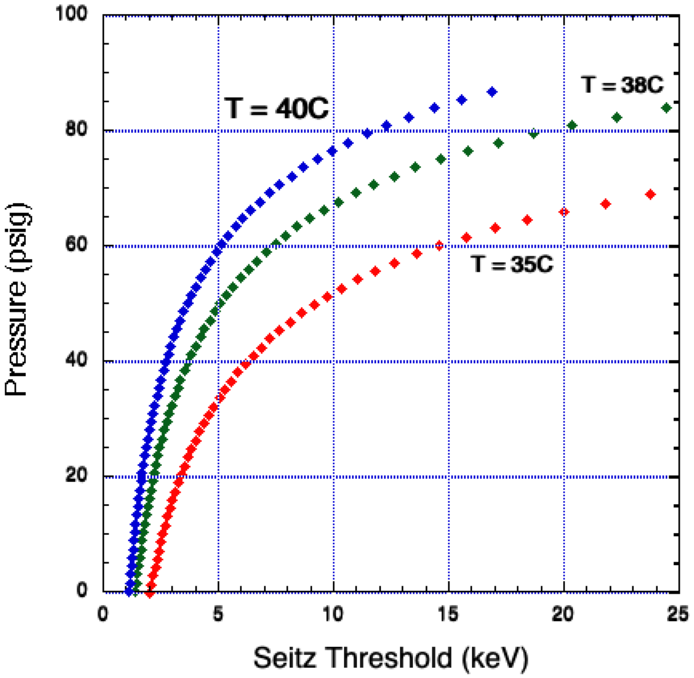

Figure 4.16: Seitz threshold calculation in R-134a for increasing pressures at fixed temperatures. The GUNTER neutron calibration with ^{88}Y/Be was conduced at 35 C with excellent temperature stability (see Section 2.2).

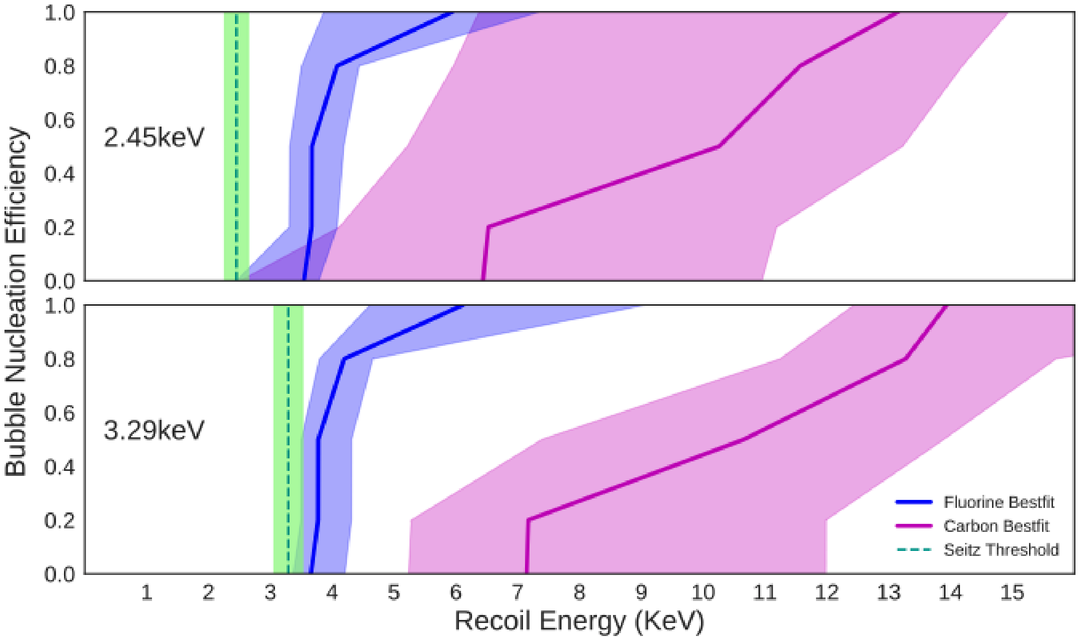

Figure 4.17: Best-fit efficiency curves for 2.45 keV and 3.29 keV PICO-60 C_3F_8 data. The calculated Seitz threshold is shown as a green dashed line. The shaded regions represent all efficiency curves fitted within 1σ. Figure from Amole et al. (2019).

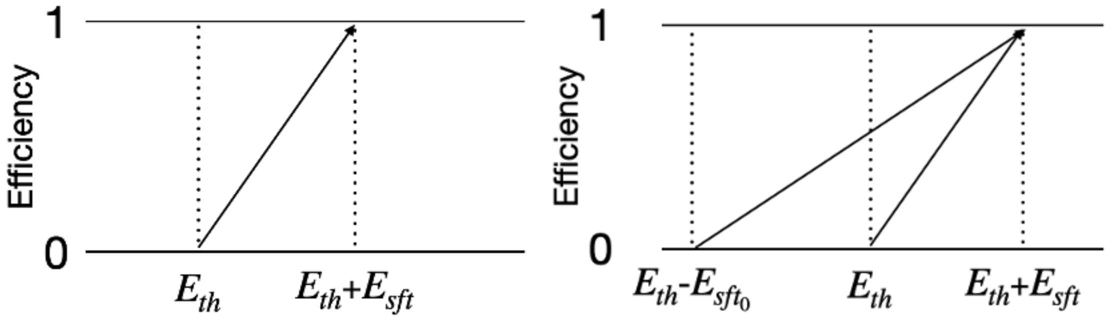

Figure 4.18: Diagrams of linear threshold models for bubble nucleation efficiency. Left: in the simplest linear threshold case explored, E_{th} is the calculated Seitz threshold, and E_{sft} is the softness of threshold (see text) being considered. If a unique softness of threshold were to be considered for each recoiling species, that would make for three additional free parameters besides the Harper factor, bringing it to a total of four free parameters. Right: this more involved linear threshold model considers a softness of threshold defined at some energy below E_{th} as well, labeled E_{sft_0}. If two unique softness of thresholds as described were to be considered for each recoiling species, that would make for six additional free parameters besides the Harper factor, bringing it to a total of seven free parameters.

second.

For the simplest version of the threshold model, all energy depositions larger than or equal to $E_{th} + E_{sft}$ are assumed to have full efficiency. In contrast, all events with energy deposited lower than the threshold $E_{th}$are assumed to have zero efficiencies. For every energy deposition falling between E_{th} and $E_{thr} + E_{sft}$, a weighted coin Monte Carlo simulation is invoked to determine whether or not a bubble is produced based on the calculated probability $(E_d - E_{th})/E_{sft}$, where E_d is the energy deposited and $E_{th} < E_d \leq E_{sft}$ (see Figure 4.18). The first case considered explored a broad range of combinations for Harper factor and softness of threshold (see Figure 4.19). The latter was constant across all recoiling species, although we know this is not true (see Figure 4.17). As expected, the fit was quite poor, but a few things stood out. For a parameter space probed between 1-20, the best fit Harper factor at 4.88 seemed in line with literature values that have been determined experimentally and theoretically (see Section 3.1). The best fit softness of threshold at 2.12 keV is not too dissimilar to what one would expect given the best-fit efficiency curves for the softness of threshold of carbon and fluorine (see Figure 4.17). However, it must be emphasized that the

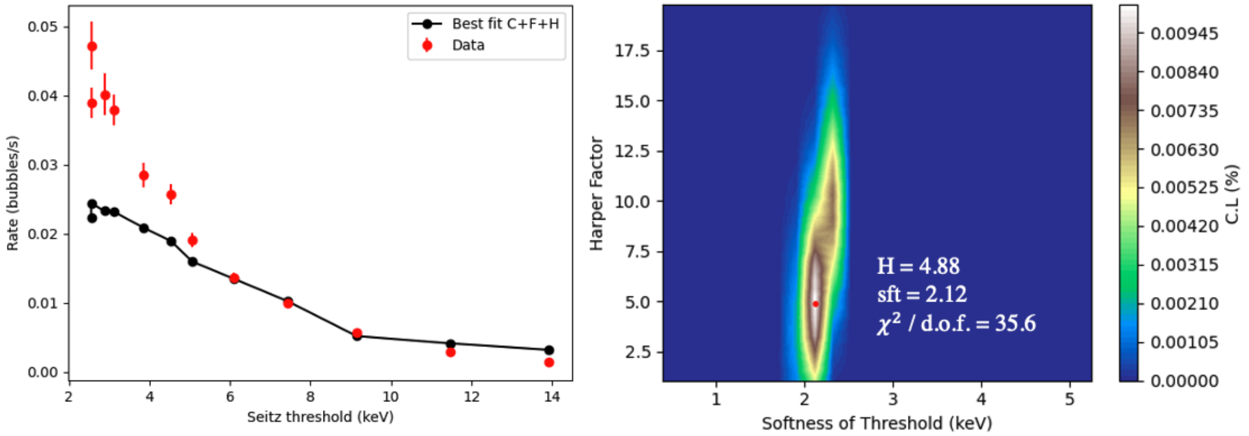

Figure 4.19: Simulated bubble nucleation rate in R-134a for the simplest linear threshold model, which considered an equal softness of threshold above E_{th} across all recoiling species. It is quite a poor fit with a reduced chi-squared $\chi^2_\nu = 35.6$ (see right panel), but it served as a starting point for scaling the complexity of the linear threshold model (see text).

best-fit model did not even come close to describing the bubble nucleation rates dominated by proton recoils at the lowest thresholds (2.6-3.1 keV). Still, it can be noted that the simulation begins to converge with the data halfway through the transition regime as proton recoils begin to vanish considerably fast (see Figure 4.14).

Many visual and quantitative checks were conducted to verify the quality of accepted bubble events from the data with consistent results. However, not much else could be done about the dead spot in the spatial reconstruction (see Figure 4.5), which is considered a factor that could explain the excess rates at low threshold energies if multiple-bubble events were to have made the cuts unnoticed. The ionization threshold model for R-134a (see Figures 4.10 and 4.11) was used to calculate the potential contribution of electron recoil contamination due to energy deposited from gammas produced by ^{88}Y/Be. The leading bubble nucleation rate from electron recoils was estimated to be subdominant by two orders of magnitude ($\approx 1.18 \times 10^{-4}$ bubbles/s at the 30 psig data point) and hence considered negligible throughout. The simulated spectra of energy deposited in the active volume of GUNTER from gammas produced by ^{88}Y/Be are shown in Figure 4.20.

The following hypothesis involved considering different Harper factors, one unique to

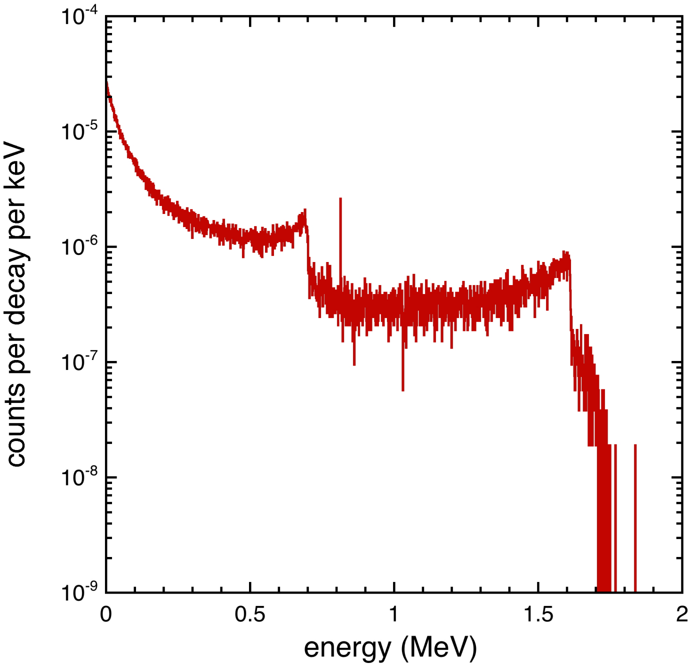

Figure 4.20: Energy deposited in the active volume of GUNTER by gammas emitted from the ^{88}Y/Be source. The bubble nucleation rate from gamma-induced electron recoils was found to be negligible (see text).

hydrogen recoils and another unique to carbon and fluorine recoils. The motivation behind this test was the different dominant recoil mechanisms between proton recoils and nuclear recoils and the possibility of an "effective" Harper factor being better suited to describe the response of R-134a to proton and nuclear recoils. However, it was determined that this was not well-motivated, recalling that even the best-case scenario rates acquired from simulation using step thresholds disregarding stopping power conditions failed to explain the excess rates at low energy thresholds relative to simulation. Instead, additional free parameters and constraints on low threshold data were considered using the linear threshold model described for all recoiling species (see Figure 4.21).

Given that proton recoils are driven by ionization, as previously discussed, compared to nuclear recoils from heavier counterparts like carbon and fluorine (see Figure 4.2), this model may be incorrect in its assumptions of the double threshold imposed for proton recoils. Per-

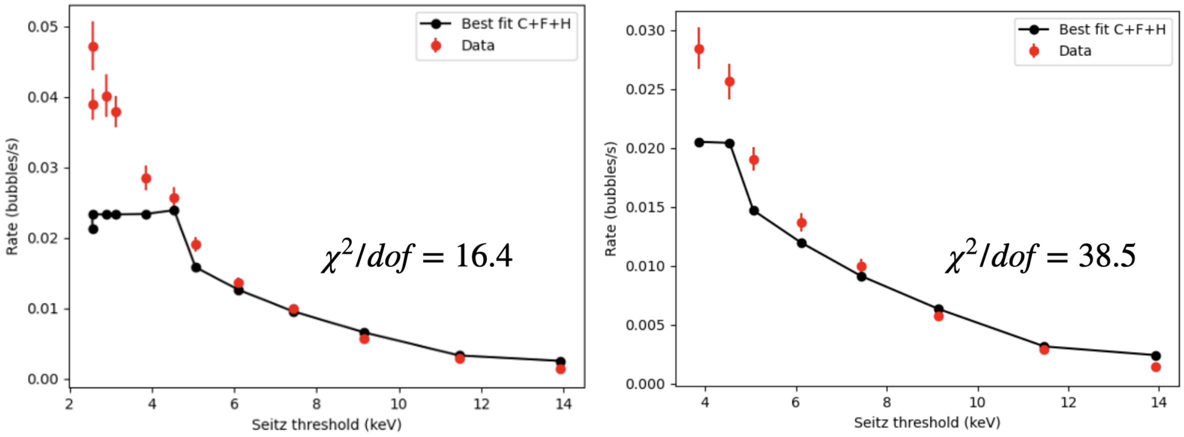

Figure 4.21: Best fit comparison between all data and constrained data to bubble nucleation rates in R-134a for the linear threshold model with seven free parameters, as described in Figure 4.18. It is worth emphasizing how poor the fits are.

haps an unknown ionization energy threshold model or extension to the traditional double threshold set by Seitz theory describes the proton recoil mechanism more accurately than one that treats proton recoils as nuclear recoils. If true, the probability of nucleation per unit of energy deposited could take a similar form, in principle, to that of the ionization threshold derived and demonstrated for electron recoils in C_3F_8 (see Sections 2.1 and 3.1) and R-134a (see the previous section). Keep in mind this is the first-time exploration of R-134a to define its response parameters. Recall that bubble nucleation probability from electron recoils was observed to follow an exponential decay with a fundamental constant depending on the attenuation of a threshold-energy photon. The author suspects that there are bubble nucleations unaccounted for in R-134a simulation from proton recoils that do not meet the two imposed conditions for nucleation but still occur via some mechanism of ionization that dominates at low threshold energies (see Figure 4.2). It is unclear how this hypothetical ionization energy threshold for proton recoils would look combined with the conditions imposed by traditional Seitz theory, which, again, effectively describes nuclear recoils. The implications of an ionization energy threshold for proton recoils would play a crucial role in informing efforts aimed at extending low mass dark matter sensitivity using hydrogen-rich compounds (see Section 2.1). Lastly, it would also expand the current understanding of the proton recoil mechanisms that can lead to bubble nucleations in superheated liquids.

Appendices

APPENDIX A

ELECTRON RECOIL ANALYSIS

A.1 Fit Methodology

The fitting software tools used for electron recoil analysis were developed as MATLAB functions. Chi-square minimization was considered using Poisson statistics on the number of events observed. These notes on the fit methodology follow closely the electron recoil analysis technical documentation written by Dan Baxter to summarize the analysis performed on all PICO electron recoil calibration data.

Pure C_3F_8 data is first fit to a simple two-parameter exponential

$$\nu = t_e \times (r_b + s_E A e^{-BQ_1}), \tag{A.1}$$

where ν is the expected number of counts, t_e the expansion time, r_b the measure background rate, s_E the simulated rate of energy deposited due to the source, A and B are free parameters, and Q_1 is the threshold for the bubble nucleation model being tested.

$$Q_1 = \frac{W_{min}}{r_l} = \frac{(4\pi/3)\sigma r_c^2}{(r_c^3 \rho_b/\rho_l)^{1/3}} = \frac{4\pi}{3}\sigma r_c \left(\frac{\rho_l}{\rho_b}\right)^{1/3}, \tag{A.2}$$

where W_{min} is the minimum work required to produce a critically sized bubble within a liquid, r_c the critical radius, σ the surface tension, r_l the critical radius of the liquid that must boil to produce a critically sized gas bubble, and ρ_l and ρ_b are the densities of the liquid and bubble, respectively. The threshold Q_1 is a function of pressure and temperature that scales differently from the Seitz threshold Q_T

$$Q_1 = Q_1(P, T) \not\approx Q_T. \tag{A.3}$$

Given an expectation ν, the probability of observing k events is given by the probability function for a Poisson process

$$P(k,v) = \frac{e^{-\nu}\nu^{k}}{k!}. \tag{A.4}$$

Hence, the chi-squared is calculated as the log likelihood function times a factor of -2

$$\chi^2 = -2(k - \nu + k\log(\nu/k)). \tag{A.5}$$

A nuisance threshold Q_1' is considered such that the total χ^2 of each data point is minimized with an additional χ^2 given to each datapoint

$$\chi_Q^2(Q_1 - Q_1')^2/\sigma_Q^2. \tag{A.6}$$

Similarly, a χ^2 is given to each correlated nuisance parameter N

$$\chi_N^2 = (N - N')^2/\sigma_N^2. \tag{A.7}$$

The correlated nuisance parameters include the normalization of simulation by detector and source, regardless of whether or not each detector used the same source. The threshold minimization occurs after the application of these nuisance parameters. Lastly, the total χ^2 for all data points and nuisance parameters is tabulated and minimized to find the best fit.

APPENDIX B

GUNTER R-134A MCNP INPUT FILES

B.1 ^{88}Y/Be

B.1.1 Neutrons

```
c ********************* GUNTER GEOMETRY
c ----- top hemisphere of active liquid -----
1  3  -1.16  -1  3
c ----- top hemisphere of the OV -----
2  1  -2.72  -2  3 1
c ----- active liquid cylinder -----
3  3  -1.16  -5 -3 69
c ----- non-active liquid cylinder -----
30  3  -1.16  -5 -69 4
c ----- glass wall of OV around active volume -----
4  1  -2.72  -6  -3 4 5
c ----- hemisphere IV (epoxy) -----
5  7  -1.18  -7  9
c ----- hemisphere IV (glass) -----
6  1  -2.72  -8  9  7
c -----  IV cylinder -----
7  2  -0.00125  -11 -9 10
c ----- IV cylindrical wall -----
8  1  -2.72  -12 -9 10 #7
c ----- C2F4H2 (prev C3F8) between IV and OV -----
9  3  -1.16  -5 -4 10 #5 #6 #7 #8
c ----- glass wall -----
10 1  -2.72  -6  -4 10 #5 #6 #7 #8 #9
c ----- main volume of water -----
12 4  -1. -15 -13 14 #1 #2 #3 #4 #5 #6 #7 #8 #9 #10 #30
c ----- water in neck -----
13 4  -1.  -16 -14 10 6
c ----- acrylic -----
14 5  -1.2  -17 -18 19 #1 #2 #3 #4 #5 #6 #7 #8 #9 #10 #12 #13 #30
c ----- SS flange -----
15 6  -8.0  -20 -19 10 16
c ****************************----- Y/Be GEOMETRY
c ----- BeO -----
20  10  -2.7337 -35 -81 80:-86 -85 84 80
c ----- J-B Weld -----
21  11  -1.16 -46 -43 -45
c ----- glass -----
22  9  -2.23 36 -45 -42 (43:46)
c ----- source capsule  -----
23  6  -7.87  35 -40 -34 (-37:38:-32) (37:-33) (-36:30:39) (39:31:-37)
c ----- Air -----
18  2  -0.00125  -50 #1 #2 #3 #4 #5 #6 #7 #8 #9 #10 #12 #13 #14 &
                     #15 #20 #21 #22 #23 #30
c ----- outside world -----
19 0  50
```

```
c ********************* SURFACE CARDS
1 SO 1.2
2 SO 1.5
3 PZ 0
69 PZ -1.84
4 PZ -2.3
5 CZ 1.2
6 CZ 1.5
7 1 SO 0.7
8 1 SO 0.95
9 1 PZ 0
10 2 PZ 0
11 CZ 0.7
12 CZ 0.95
13 3 PZ 0
14 4 PZ 0
15 CZ 3.81
16 CZ 1.905
17 CZ 4.1275
18 3 PZ 2.54
19 5 PZ 0
20 CZ 11.43
21 8 C/X 0 8.27 1.27
22 8 PX -9.77
23 8 PX -9.14
24 7 C/Z 4.3 0. 0.16
25 7 C/Z 4.79 0. 0.65
26 7 PZ 0.765
27 PZ -1.785
28 PZ -0.515
50 SO 25 $ World Sphere
c ****************************----- Y/Br -----
c ----- Steel conflat source body -----
30 6 cx 0.635
31 6 cx 0.8
32 6 cx 0.9525
33 6 cx 1.27
34 6 cx 1.69
35 6 px 0
36 6 px 0.279
37 6 px 2.54 $ Not exactly measured
38 6 px 3.048
39 6 px 3.81
40 6 px 4.572
c ----- High-recovery vial -----
42 6 cx 0.584
43 6 cx 0.45
45 6 px 3.479
46 6 kx 0.479 1 1
c ----- BeO $ 6.72 + 1.197 + .175 = 8.092 -----
80 6 px  -0.92
81 6 cx  1.327
84 6 cx  1.375
85 6 cx  2.30
86 6 px  1.7475
```

```
c  ********** MODES AND IMPORTANCES ***********
c changed importances to have correct number of Cells
imp:n 1 1 1 1 1 1 1 1 1 1 1 1 1 1 1 1 1 1 1 1 0
imp:p 1 1 1 1 1 1 1 1 1 1 1 1 1 1 1 1 1 1 1 1 0
mode  n p
c mode n
tr1 0 0 -3.25
tr2 0 0 -13.12
tr3 0 0 4.5
tr4 0 0 -8.2
tr5 0 0 -10.74
tr6 6.45 0 -2.7722 0 0 1 0 1 0 -1 0 0
tr7 -33.1 0 35.1
tr8 -30.1 0 33.1
c ----- quartz (2.32) -----
m1    14028.70c 1 &
       8016.70c 2
c ----- air  O-23.2, N-75.5,Ar-1.3 (0.00125) -----
m2    8016.70c 23  &
      7014.70c 75  &
     18036.70c 1
c ----- C2F4H2 $C3F8 (1.38) -----
m3    6000.70c  2 &
      9019.70c  4 &
      1001.70c  2
c ----- H2O (1.0) -----
m4    1001.70c  2 &
      8016.70c  1
c ----- acrylic (1.2) -----
m5    1001.70c  8 &
      6000.70c  5 &
      8016.70c  2
c ----- steel alloy 304 -----
m6   6000.70c -0.0002  &
     7014.70c -0.0005  &
    14028.70c -0.0045  &
    15031.70c -0.0003  &
    22046.70c -0.0002475 &
    22047.70c -0.0002232 &
    22048.70c -0.0022119 &
    22049.70c -0.0001623 &
    22050.70c -0.0001554 &
    24050.70c -0.0081 &
    24052.70c -0.1570 &
    24053.70c -0.0178 &
    24054.70c -0.0044 &
    25055.70c -0.013  &
    26054.70c -0.0410 &
    26056.70c -0.6434 &
    26057.70c -0.0148 &
    26058.70c -0.0020 &
    27059.70c -0.0039 &
    28058.70c -0.0553 &
    28060.70c -0.0213 &
    28061.70c -0.0009 &
    28062.70c -0.0030 &
    28064.70c -0.0008 &
    29063.70c -0.0033 &
```

```
    29065.70c -0.0015
c ----- cast epoxy (dens. = 1.18) -----
m7     6000.70c 18 &
       1001.70c 19 &
       8016.70c 3
c ----- antimony rod -----
m8    51121.70c 1
c ----- Borosilicate Glass -----
m9    5010.70c       -0.008 &
      5011.70c       -0.032 &
      8016.70c       -0.541 &
      11023.70c       -0.03 &
     14028.70c        -0.3477 &
     14029.70c        -0.0177 &
     14030.70c        -0.0116 &
     13027.70c        -0.012
c ----- BeO -----
m10   4009.70c 0.5 &
      8016.70c 0.4985 &
      16032.70c 0.0015
c - J-B-Weld Approximation -
m11  1001.70c  0.156 &
     6000.70c  0.251 &
     7014.70c  0.002 &
     8016.70c  0.271 &
     20040.70c 0.0037 &
     26054.70c 0.0117 &
     26056.70c 0.1835 &
     26057.70c 0.0042 &
     26058.70c 0.00061
sdef  pos=6.45 0.0 -2.29 cel=20 erg=d2 rad=d1 par=1
si1 0. 4.
sp1 -21 0
si2 L 0.152 0.963
sp2 0.995 0.005
phys:n j 20.
phys:p 0 1 1
cut:n 200000 0.
cut:p 200000 j 0
nps 1E8
ipol 0 0 0 0 2j 1 3
rpol 1e-7 1e-7
files 21 dumn1     3j 22 dumn2
```

B.1.2 Gammas

```
c ********************* GUNTER GEOMETRY
c ----- top hemisphere of active liquid -----
1  3  -1.16  -1  3
c ----- top hemisphere of the OV -----
2  1  -2.72  -2  3 1
c ----- active liquid cylinder -----
3  3  -1.16  -5 -3 69
c ----- non-active liquid cylinder -----
30  3  -1.16  -5 -69 4
c ----- glass wall of OV around active volume -----
4  1  -2.72  -6  -3 4 5
c ----- hemisphere IV (epoxy) -----
5  7  -1.18  -7  9
c ----- hemisphere IV (glass) -----
6  1  -2.72  -8  9  7
c -----  IV cylinder -----
7  2  -0.00125  -11 -9 10
c ----- IV cylindrical wall -----
8  1  -2.72  -12 -9 10 #7
c ----- C2F4H2 (prev C3F8) between IV and OV -----
9  3  -1.16  -5 -4 10 #5 #6 #7 #8
c ----- glass wall -----
10 1  -2.72  -6  -4 10 #5 #6 #7 #8 #9
c ----- main volume of water -----
12 4  -1. -15 -13 14 #1 #2 #3 #4 #5 #6 #7 #8 #9 #10 #30
c ----- water in neck -----
13 4  -1.  -16 -14 10 6
c ----- acrylic -----
14 5  -1.2  -17 -18 19 #1 #2 #3 #4 #5 #6 #7 #8 #9 #10 #12 #13 #30
c ----- SS flange -----
15 6  -8.0  -20 -19 10 16
c *****************************----- Y/Be GEOMETRY
c ----- BeO -----
20  10  -2.7337 -35 -81 80:-86 -85 84 80
c ----- J-B Weld -----
21  11  -1.16 -46 -43 -45
c ----- glass -----
22  9  -2.23 36 -45 -42 (43:46)
c ----- source capsule  -----
23  6  -7.87  35 -40 -34 (-37:38:-32) (37:-33) (-36:30:39) (39:31:-37)
c ----- Air -----
18  2  -0.00125  -50 #1 #2 #3 #4 #5 #6 #7 #8 #9 #10 #12 #13 #14 &
                     #15 #20 #21 #22 #23 #30
c ----- outside world -----
19 0  50

c ********************* SURFACE CARDS
1 SO 1.2
2 SO 1.5
3 PZ 0
69 PZ -1.84
C 30 PZ -2.176 $ old plane, incorrectly calculated
4 PZ -2.3
C 4 PZ -2.72   $ old plane, incorrectly calculated
5 CZ 1.2
6 CZ 1.5
```

```
7 1 SO 0.7
8 1 SO 0.95
9 1 PZ 0
10 2 PZ 0
11 CZ 0.7
12 CZ 0.95
13 3 PZ 0
14 4 PZ 0
15 CZ 3.81
16 CZ 1.905
17 CZ 4.1275
18 3 PZ 2.54
19 5 PZ 0
20 CZ 11.43
C 21 C/X 0 -0.96 1.27
C 22 PX 1.78
C 23 PX 2.41
21 8 C/X 0 8.27 1.27
22 8 PX -9.77
23 8 PX -9.14
24 7 C/Z 4.3 0. 0.16
25 7 C/Z 4.79 0. 0.65
26 7 PZ 0.765
27 PZ -1.785
28 PZ -0.515
50 SO 25 $ World Sphere
c *****************************----- Y/Br
c ----- Steel conflat source body -----
30 6 cx 0.635
31 6 cx 0.8
32 6 cx 0.9525
33 6 cx 1.27
34 6 cx 1.69
35 6 px 0
36 6 px 0.279
37 6 px 2.54 $ Not exactly measured
38 6 px 3.048
39 6 px 3.81
40 6 px 4.572
c ----- High-recovery vial -----
42 6 cx 0.584
43 6 cx 0.45
45 6 px 3.479
46 6 kx 0.479 1 1
c ----- BeO $ 6.72 + 1.197 + .175 = 8.092 -----
80 6 px  -0.92
81 6 cx  1.327
84 6 cx  1.375
85 6 cx  2.30
86 6 px  1.7475

c  ********** MODES AND IMPORTANCES ***********
c changed importances to have correct number of Cells
imp:n 1 1 1 1 1 1 1 1 1 1 1 1 1 1 1 1 1 1 1 0
imp:p 1 1 1 1 1 1 1 1 1 1 1 1 1 1 1 1 1 1 1 0
mode  p
c mode n
```

```
tr1 0 0 -3.25
tr2 0 0 -13.12
tr3 0 0 4.5
tr4 0 0 -8.2
tr5 0 0 -10.74
c (prev) tr6 6.42 0 -2.7722 0 0 1 0 1 0 -1 0 0    $-3.5419
tr6 6.45 0 -2.7722 0 0 1 0 1 0 -1 0 0
tr7 -33.1 0 35.1
tr8 -30.1 0 33.1
c ----- quartz (2.32) -----
m1    14028.70c 1 &
       8016.70c 2
c ----- air  O-23.2, N-75.5,Ar-1.3 (0.00125) -----
m2    8016.70c 23  &
      7014.70c 75  &
     18036.70c 1
c ----- C2F4H2 $C3F8 (1.38) -----
m3    6000.70c  2 &
      9019.70c  4 &
      1001.70c  2
c ----- H2O (1.0) -----
m4    1001.70c  2 &
      8016.70c  1
c ----- acrylic (1.2) -----
m5    1001.70c  8 &
      6000.70c  5 &
      8016.70c  2
c ----- steel alloy 304 -----
m6   6000.70c -0.0002  &
     7014.70c -0.0005  &
    14028.70c -0.0045  &
    15031.70c -0.0003  &
    22046.70c -0.0002475 &
    22047.70c -0.0002232 &
    22048.70c -0.0022119 &
    22049.70c -0.0001623 &
    22050.70c -0.0001554 &
    24050.70c -0.0081 &
    24052.70c -0.1570 &
    24053.70c -0.0178 &
    24054.70c -0.0044 &
    25055.70c -0.013  &
    26054.70c -0.0410 &
    26056.70c -0.6434 &
    26057.70c -0.0148 &
    26058.70c -0.0020 &
    27059.70c -0.0039 &
    28058.70c -0.0553 &
    28060.70c -0.0213 &
    28061.70c -0.0009 &
    28062.70c -0.0030 &
    28064.70c -0.0008 &
    29063.70c -0.0033 &
    29065.70c -0.0015
c ----- cast epoxy (dens. = 1.18) -----
m7     6000.70c 18 &
       1001.70c 19 &
       8016.70c 3
```

```
c ----- antimony rod -----
m8    51121.70c 1
c ----- Borosilicate Glass -----
m9    5010.70c       -0.008 &
      5011.70c       -0.032 &
      8016.70c       -0.541 &
      11023.70c       -0.03 &
     14028.70c        -0.3477 &
     14029.70c        -0.0177 &
     14030.70c        -0.0116 &
     13027.70c        -0.012
c ----- BeO -----
m10   4009.70c 0.5 &
      8016.70c 0.4985 &
      16032.70c 0.0015
c - J-B-Weld Approximation -
m11  1001.70c  0.156 &
     6000.70c  0.251 &
     7014.70c  0.002 &
     8016.70c  0.271 &
     20040.70c 0.0037 &
     26054.70c 0.0117 &
     26056.70c 0.1835 &
     26057.70c 0.0042 &
     26058.70c 0.00061
c **************************************
c YBe neutron source.
c This source generates neutrons of two energies throughout the BeO (cell 20)
c The sampling follows a 1/r^2 distribution from a point defined at
c The tip of the Glass vial. If the physical source is moved in the
c geometry, then the point in sdef needs to be moved accordingly
c =================================== Source ====================================
c  Neutron source of 152 keV (99.5%) and 963 keV (0.5%)
c ==============================================================================
c sdef  pos=6.45 0.0 -2.29 cel=20 erg=d2 rad=d1 par=1
sdef  pos=6.45 0.0 -2.29 erg=d1 par=2
si1 L 0.898 1.836
sp1   0.936 0.992
c To sample a sphere of radius 4, the first argument of sp1 should be -21
c The second argument should be 2 for uniform sampling, 0 for 1/r^2 sampling
c throughout the sphere
C si1 0. 4.
C sp1 -21 0
c To call two neutron energies, is the same as two gamma energies.
C si2 L 0.152 0.963
C sp2 0.995 0.005
f18:p  3 $ E dep spectrum in cell #1 (choose your cell)
e18  0 2999i 3  $ 3000 bins between 0 and 3 MeV
c ==============================================================================
C phys:n j 20.
c phys:p j 1 1
C cut:n 200000 0.
c cut:p 200000 j 0
nps 1E8
C ipol 0 0 0 0 2j 1 3
files 21 dumn1     3j 22 dumn2
```

B.2 ^{22}Na

B.2.1 Gammas

```
c ******************** GUNTER GEOMETRY
c ----- top hemisphere of active liquid -----
1  3  -1.15  -1  3
c ----- top hemisphere of the OV -----
2  1  -2.32  -2  3 1
c ----- active liquid cylinder -----
3  3  -1.15  -5  -3 4
c ----- glass wall of OV around active volume -----
4  1  -2.32  -6  -3 4 5
c ----- hemisphere IV (epoxy) -----
5  7  -1.18  -7  9
c ----- hemisphere IV (glass) -----
6  1  -2.32  -8  9  7
c -----  IV cylinder -----
7  2  -0.00125  -11 -9 10
c ----- IV cylindrical wall -----
8  1  -2.32  -12 -9 10 #7
c ----- r134a between IV and OV -----
9  3  -1.15  -5 -4 10 #5 #6 #7 #8
c ----- glass wall -----
10 1  -2.32  -6  -4 10 #5 #6 #7 #8 #9
c ----- acrylic source button -----
11 5  -1.2  -21 22 -23
c 11 4  -1.  -21 22 -23 $ acrylic source button (NOW WATER FOR SB-124)
c ----- main volume of water -----
12 4  -1. -15 -13 14 #1 #2 #3 #4 #5 #6 #7 #8 #9 #10 #11
c ----- water in neck -----
13 4  -1.  -16 -14 10 6
c ----- acrylic -----
14 5  -1.2  -17 -18 19 #1 #2 #3 #4 #5 #6 #7 #8 #9 #10 #11 #12 #13
c ----- SS flange -----
15 6  -8.0  -20 -19 10 16
c ----- antimony rod -----
c 16 8  -6.7  -28 27 -24
c ----- source capsule (all epoxy approx.) -----
c 17 7  -1.18 -26 27 -25 #16
c ----- Air -----
18 2  -0.00125  -50 #1 #2 #3 #4 #5 #6 #7 #8 #9 #10 #11 #12 #13 #14 &
                   #15 $ #16 #17 #20 #21 #22 #23
c ----- outside world -----
19 0  50

c ******************** SURFACE CARDS
1 SO 1.2
2 SO 1.5
3 PZ 0
4 PZ -2.3
5 CZ 1.2
6 CZ 1.5
7 1 SO 0.7
8 1 SO 0.95
```

```
9 1 PZ 0
10 2 PZ 0
11 CZ 0.7
12 CZ 0.95
13 3 PZ 0
14 4 PZ 0
15 CZ 3.81
16 CZ 1.905
17 CZ 4.1275
18 3 PZ 2.54
19 5 PZ 0
20 CZ 11.43
C 21 C/X 0 -0.96 1.27
C 22 PX 1.78
C 23 PX 2.41
21 C/X 0 8.27 1.27
22 PX -9.77
23 PX -9.14
24 C/Z 4.3 0. 0.16
25 C/Z 4.79 0. 0.65
26 PZ 0.765
27 PZ -1.785
28 PZ -0.515
50 SO 25 $ World Sphere

c  ********** MODES AND IMPORTANCES ***********
C imp:n 1 1 1 1 1 1 1 1 1 1 1 1 1 1 1 0
imp:p 1 1 1 1 1 1 1 1 1 1 1 1 1 1 1 0
C mode  n p
mode p
tr1 0 0 -3.25
tr2 0 0 -13.12
tr3 0 0 4.5
tr4 0 0 -8.2
tr5 0 0 -10.74
tr6 -1.84 0 8 0 0 1 0 1 0 -1 0 0
c ----- quartz (2.32) -----
m1    14000.84p 1 &
       8000.84p 2
c ----- air  O-23.2, N-75.5,Ar-1.3 (0.00125) -----
m2    8000.84p 23  &
      7000.84p 75  &
     18000.84p 1
c ----- r134a (1.15) -----
m3    1000.84p  2 &
      6000.84p  2 &
      9000.84p  4
c ----- H2O (1.0) -----
m4    1000.84p  2 &
      8000.84p  1
c ----- acrylic (1.2) -----
m5    1000.84p  8 &
      6000.84p  5 &
      8000.84p  2
c ----- Stainless Steel (8.0) -----
m6    24000.84p 8  &
      26000.84p 74 &
```

```
      28000.84p 18
c ----- cast epoxy (dens. = 1.18) -----
m7     6000.84p 18 &
       1000.84p 19 &
       8000.84p 3
c ----- antimony rod -----
m8    51000.84p 1
c     Source Cards (Point Gamma Source)
c ************************************
sdef par=2 pos=7.8581 0 0.0200 erg=d1
si1 L 0.511 1.275
sp1   0.875 1
c si1 L 0.511 1.275
C sp1   0.64 0.36
C f8:p  3 $ Replace the "1" with whatever cell you are using
C e8  0. 1999i 2. $ This indicates 2000 bins between 0 and 2 MeV
C phys:n j 20.
C phys:p 100  0  0  0  1  0  0 $ 0 1 1
phys:p 100 0 0
c cut:n 2000
C cut:p 2j 0
nps 1E7
ipol 0 0 0 0 2j 1 3
files 21 dumn1     3j 22 dumn2
```

APPENDIX C

ANALYSIS CODE

C.1 Simulated Rates using Linear Threshold Model

C.1.1 Program

The program for simulating neutron calibrations for R-134a using ^{88}Y/Be can be found in **https://github.com/jofuentes19/PICO**. This repository includes stopping power and range tables for carbon, fluorine, and hydrogen, necessary for calculating the Seitz threshold. A Dropbox link to the MCNP-PoliMi neutron simulation output is included there as well. This file scans the simulated energies deposited by carbon, fluorine, and hydrogen recoils to determine whether bubble nucleation occured based on the linear threshold model (see Section 4.3).

C.2 Technical Note

The program was initially developed entirely in Python and later optimized with Cython [https://cython.org] C extensions for a dramatic performance tune-up. If you do not already have it, the easiest way to install Cython is with **pip**:

```
pip install Cython
```

C.2.1 setup.py

Create a copy of **program.py** with a **.pyx** extension, i.e. **program.pyx**, and then compile it using **setup.py**:

```
from distutils.core import setup
from distutils.extension import Extension
from Cython.Distutils import build_ext
import numpy

ext_modules=[ Extension("program",
```

```
              ["program.pyx"],
              libraries=["m"],
              extra_compile_args = ["-ffast-math"])]

setup(
  name = "program",
  cmdclass = {"build_ext": build_ext},
  ext_modules = ext_modules,
  include_dirs=[numpy.get_include()])
```

In the terminal or command prompt:

```
python setup.py build_ext --inplace
```

Once you have compiled a version of the program you can run it with **run.py**:

```
import program
```

In the terminal or command prompt:

```
python run.py
```

C.2.2 Best Fit and Visualization

Additional scripts are used for post-processing and visualization. It computes the weighted sum of squared deviations

$$S = \sum_{i=1}^{N} \left(\frac{y_i^{exp} - y_i^{the}}{\sigma_i} \right)^2$$

where y_i^{exp} and σ_i^2 stand for the experimental data point value and its variance or error in the ith bin and y_i^{the} is the theoretical prediction for the candidate model under analysis.

REFERENCES

Ackermann, M. et al. (2015). Searching for Dark Matter Annihilation from Milky Way Dwarf Spheroidal Galaxies with Six Years of Fermi Large Area Telescope Data. *Phys. Rev. Lett. 115*(23), 231301.

Albert, A. et al. (2017). Searching for Dark Matter Annihilation in Recently Discovered Milky Way Satellites with Fermi-LAT. *Astrophys. J. 834*(2), 110.

Amole, C. et al. (2016). Improved Dark Matter Search Results from PICO-2L Run 2. *Phys. Rev. D 93*(6), 061101.

Amole, C. et al. (2017). Dark Matter Search Results from the PICO-60 C_3F_8 Bubble Chamber. *Phys. Rev. Lett. 118*(25), 251301.

Amole, C. et al. (2019). Dark Matter Search Results from the Complete Exposure of the PICO-60 C_3F_8 Bubble Chamber. *Phys. Rev. D 100*(2), 022001.

Andernach, H. and F. Zwicky (2017). English and Spanish translation of Zwicky's (1933) The Redshift of Extragalactic nebulae.

Apfel, R. E. (1979). The Superheated Drop Detector. *Nuclear Instruments and Methods 162*(1), 603–608.

Arcadi, G. et al. (2018). The Waning of the WIMP? A Review of Models, Searches, and Constraints. *Eur. Phys. J. C 78*(3), 203.

Archambault, S. et al. (2011). New Insights into Particle Detection with Superheated Liquids. *New Journal of Physics 13*(4), 043006.

ATLAS Collaboration (2020). Probing Dark Matter with the Higgs Boson.

Aubin, F. et al. (2008). Discrimination of Nuclear Recoils from Alpha Particles with Superheated Liquids. *New J. Phys. 10*, 103017.

Ayinde, B., T. Inanc, and J. Zurada (2019). On Correlation of Features Extracted by Deep Neural Networks. pp. 1–8.

Beck, G. (2020). Hunting Dark Matter in Galaxy Clusters with Non-Thermal Electrons. *Monthly Notices of the Royal Astronomical Society 494*(1), 1128–1132.

Begeman, K. G., A. H. Broeils, and R. H. Sanders (1991). Extended Rotation Curves of Spiral Galaxies: Dark Haloes and Modified Dynamics. *Mon. Not. Roy. Astron. Soc. 249*, 523.

Behnke, E. et al. (2008). Spin-Dependent WIMP Limits from a Bubble Chamber. *Science (New York, N.Y.) 319*, 933–6.

Behnke, E. et al. (2011). Improved Limits on Spin-Dependent WIMP-Proton Interactions from a Two Liter CF_3I Bubble Chamber. *Phys. Rev. Lett. 106*, 021303.

Behnke, E. et al. (2013). Direct Measurement of the Bubble Nucleation Energy Threshold in a CF_3I Bubble Chamber. *Phys. Rev. D 88*, 021101.

Behnke, E. et al. (2017). Final Results of the PICASSO Dark Matter Search Experiment. *Astropart. Phys. 90*, 85–92.

Bell, C. R. et al. (1974). Radiation-Induced Boiling in Superheated Water and Organic Liquids. *Nucl. Sci. Eng. 53*(4), 458–465.

Bernal, J. L. et al. (2020). Robustness of Baryon Acoustic Oscillation Constraints for Early-Universe Modifications of ΛCDM Cosmology. *Physical Review D 102*(12).

Bertone, G. et al. (2007). WIMP Identification Through a Combined Measurement of Axial and Scalar Couplings. *Phys. Rev. Lett. 99*, 151301.

Blumenthal, G. R. et al. (1984). Formation of Galaxies and Large Scale Structure with Cold Dark Matter. *Nature 311*, 517–525.

Bolte, W. et al. (2006). A Bubble Chamber for Dark Matter Detection (the COUPP Project Status). *Journal of Physics: Conference Series 39*, 126.

Buchmueller, O., M. J. Dolan, and C. McCabe (2014). Beyond Effective Field Theory for Dark Matter Searches at the LHC. *JHEP 01*, 025.

Carr, B. J. et al. (2010). New Cosmological Constraints on Primordial Black Holes. *Phys. Rev. D 81*, 104019.

Chang, M. and Y. Cheng (2007). Motion Detection by Using Entropy Image and Adaptive State-Labeling Technique. *2007 IEEE International Symposium on Circuits and Systems*, 3667–3670.

Chen, G. (2009). Staged Regressions as a Remedy to the Multicollinearity Problem. *SSRN Electronic Journal*.

Collar, J. I. (2013). Applications of an ^{88}Y/Be Photo-neutron Calibration Source to Dark Matter and Neutrino Experiments. *Phys. Rev. Lett. 110*(21), 211101.

Cui, Y. (2015). A Review of WIMP Baryogenesis Mechanisms. *Mod. Phys. Lett. A 30*(37), 1530028.

Diamantaras, K. and S. Kung (1994). Cross-Correlation Neural Network Models. *IEEE Transactions on Acoustics, Speech, and Signal Processing 42*(11), 3218–3223.

Duncan, F., A. J. Noble, and D. Sinclair (2010). The Construction and Anticipated Science of SNOLAB. *Ann. Rev. Nucl. Part. Sci. 60*, 163–180.

El-Nagdy, M. M. and M. J. Harris (1971). Experimental Study of Radiation-Induced Boiling In Superheated Liquids. *J. Brit. Nucl. Energy Soc. 131*(10).

Farnes, J. S. (2018). A Unifying Theory of Dark Energy and Dark Matter: Negative Masses and Matter Creation within a Modified ΛCDM Framework. *Astronomy & Astrophysics 620*, A92.

Fitzpatrick, A. L. et al. (2013). The Effective Field Theory of Dark Matter Direct Detection. *JCAP 02*, 004.

Fu, L. and T. Chen (1993). Sensitivity Analysis for Input Vector in Multilayer Feedforward Neural Networks. In *IEEE International Conference on Neural Networks*, Volume 1, pp. 215–218.

Fustin, D. A. (2012). *First Dark Matter Limits from the COUPP 4 kg Bubble Chamber at a Deep Underground Site*. Ph. D. thesis, The University of Chicago.

Glaser, D. A. (1952). Some Effects of Ionizing Radiation on the Formation of Bubbles in Liquids. *Phys. Rev. 87*, 665–665.

Gluscevic, V. and others. (2015). Identifying the Theory of Dark Matter with Direct Detection. *JCAP 12*, 057.

Griest, K. and D. Seckel (1991). Three Exceptions in the Calculation of Relic Abundances. *Phys. Rev. D 43*, 3191–3203.

Hahn, J. and T. Edgar (2014). *Process Control*. John Wiley & Sons, Inc.

Han, X., H. Laga, and M. Bennamoun (2021). Image-Based 3D Object Reconstruction: State-of-the-Art and Trends in the Deep Learning Era. *IEEE Transactions on Pattern Analysis and Machine Intelligence 43*(5), 1578–1604.

Harper, M. J. (1991). *A Theoretical Model of a Superheated Liquid Droplet Neutron Detector*. Ph. D. thesis, University of Maryland College Park.

Harper, M. J. and J. C. Rich (1993). Radiation-Induced Nucleation in Superheated Liquid Droplet Neutron Detectors. *Nuclear Instruments and Methods in Physics Research Section A: Accelerators, Spectrometers, Detectors and Associated Equipment 336*(1), 220–225.

Hu, H. and Z. Yang (2007). 3D Reconstruction Approach Based on Neural Network. In *Proceedings of the 4th International Symposium on Neural Networks: Part II–Advances in Neural Networks*, ISNN '07, Berlin, Heidelberg, pp. 630–639. Springer-Verlag.

Huang, X., Y. S. Tsai, and Q. Yuan (2017). LikeDM: Likelihood Calculator of Dark Matter Detection. *Comput. Phys. Commun. 213*, 252–263.

Jungman, G., M. Kamionkowski, and K. Griest (1996). Supersymmetric Dark Matter. *Phys. Rept. 267*, 195–373.

Kim, T. (2010). Pattern Recognition Using Artificial Neural Network: A Review. Volume 76, pp. 138–148.

Kolb, E. W. and M. S. Turner (1990). *The Early Universe*. CRC Press.

Kolb, R. et al. (2018). Basic Research Needs for Dark-Matter Small Projects New Initiatives: Report of the Department of Energy's High Energy Physics Workshop on Dark Matter.

Lemmon, E. W. et al. (2018). NIST Standard Reference Database 23: Reference Fluid Thermodynamic and Transport Properties-REFPROP, Version 10.0, National Institute of Standards and Technology.

Levi, M. et al. (1978). Experimental Studies of the Acoustic Signature of Proton Beams Traversing Fluid Media. *IEEE Trans. Nucl. Sci. 25*, 325–332.

Lewin, J. D. and P. F. Smith (1996). Review of Mathematics, Numerical Factors, and Corrections for Dark Matter Experiments Based on Elastic Nuclear Recoil. *Astropart. Phys. 6*, 87–112.

Martynyuk, Y., N. Smirnova, and J. S. Wood (1991). Sound Generation in Superheated Liquids by Heavy Charged Particles. *Soviet physics. Acoustics 37*, 376–378.

Muñoz, C. (2017). Models of Supersymmetry for Dark Matter. *EPJ Web of Conferences 136*, 01002.

Nettleton, D. (2014). Commercial Data Mining: Chapter 6 - Selection of Variables and Factor Derivation. pp. 79–104.

Norman, A. and P. Spiegler (1963). Radiation Nucleation of Bubbles in Water. *Nuclear Science and Engineering 16*, 213–217.

Pedra, A. V. B. M. et al. (2013). Camera Calibration Using Detection and Neural Networks. *IFAC Proceedings Volumes 46*(7), 245–250. 11th IFAC Workshop on Intelligent Manufacturing Systems.

Peebles, P. J. E. (1994). *Principles of Physical Cosmology*. Princeton University Press.

Pozzi, S. A., E. Padovani, and M. Marseguerra (2003). MCNP-PoliMi: a Monte-Carlo code for correlation measurements. *Nuclear Instruments and Methods in Physics Research Section A: Accelerators, Spectrometers, Detectors and Associated Equipment 513*(3), 550–558.

Ressell, M. T. and M. S. Turner (1990). The Grand Unified Photon Spectrum: A Coherent View of the Diffuse Extragalactic Background Radiation. *Comments Astrophys. 14*, 323.

Robinson, A. E. (2015). *Dark matter limits from a 2L C3F8 filled bubble chamber*. Ph. D. thesis, The University of Chicago.

Roszkowski, L., R. Ruiz de Austri, and R. Trotta (2007). Implications for the Constrained MSSM from a New Prediction for $b \to s\gamma$. *JHEP 07*, 075.

Rubin, V. C., W. K. Ford, Jr., and N. Thonnard (1978). Extended Rotation Curves of High-Luminosity Spiral Galaxies. IV. Systematic Dynamical properties, Sa through Sc. *Astrophys. J. Lett. 225*, L107–L111.

Schober, P., C. Boer, and L. Schwarte (2018). Correlation Coefficients: Appropriate Use and Interpretation. *Anesthesia* & *Analgesia 126*, 1.

Sehairi, K., F. Chouireb, and J. Meunier (2017). Comparative Study of Motion Detection Methods for Video Surveillance Systems. *Journal of Electronic Imaging 26*(2), 023025.

Seitz, F. (1958). On the Theory of the Bubble Chamber. *Physics of Fluids 1*(1), 2–13.

Seth, S. et al. (2020). Probing Low-Mass WIMP Candidates of Dark Matter with Tetrafluoroethane Superheated Liquid Detectors. *Phys. Rev. D 101*, 103005.

Shannon, C. E. (1948). A Mathematical Theory of Communication. *Bell System Technical Journal 27*(3), 379–423.

Sherrit, S. and B. K. Mukherjee (2007). Characterization of Piezoelectric Materials for Transducers.

Steigman, G. and M. S. Turner (1985). Cosmological Constraints on the Properties of Weakly Interacting Massive Particles. *Nucl. Phys. B 253*, 375–386.

Tanabashi, M. et al. (2018). Review of Particle Physics. *Phys. Rev. D 98*, 030001.

Tenner, A. G. (1963). Nucleation in Bubble Chambers. *Nucl. Instrum. Meth. 22*, 1–42.

Tolley, E. (2016). Dark Matter Searches with Mono-X Signatures at the ATLAS Experiment. *PoS DIS2016*, 107.

Tolosi, L. and T. Lengauer (2011). Classification with Correlated Features: Unreliability of Feature Ranking and Solutions. *Bioinformatics (Oxford, England) 27*, 1986–94.

UCL Dark Matter (2021). Dark Matter.

Undagoitia, T. M. and L. Rauch (2015). Dark Matter Direct-Detection Experiments. *Journal of Physics G: Nuclear and Particle Physics 43*(1), 013001.

Wellstead, P. E. (2002). Control Systems Design. *International Journal of Adaptive Control and Signal Processing 16*(2), 173–174.

Ziegler, J., M. Ziegler, and J. Biersack (2010). The Stopping and Range of Ions in Matter. *Nuclear Instruments and Methods in Physics Research Section B: Beam Interactions with Materials and Atoms 268*, 1818–1823.